NAVAL POSTGRADUATE SCHOOL

MONTEREY, CALIFORNIA

THESIS

APPLICATION OF THE T-MATRIX METHOD TO THE NUMERICAL MODELING OF A LINEAR ACTIVE SONAR ARRAY

by

Erhan Ozer

June 2013

Thesis Co-Advisors: Steven R. Baker
Clyde L. Scandrett

Approved for public release; distribution is unlimited

THIS PAGE INTENTIONALLY LEFT BLANK

REPORT DOCUMENTATION PAGE	*Form Approved* *OMB No. 0704–0188*

1. REPORT DATE *(DD–MM–YYYY)* 18–6–2013	**2. REPORT TYPE** Master's Thesis	**3. DATES COVERED** *(From — To)* 2102-06-01—2104-10-31

4. TITLE AND SUBTITLE

APPLICATION OF THE T-MATRIX METHOD TO THE NUMERICAL MODELING OF A LINEAR ACTIVE SONAR ARRAY

5a. CONTRACT NUMBER

5b. GRANT NUMBER

5c. PROGRAM ELEMENT NUMBER

6. AUTHOR(S)

Erhan Ozer

5d. PROJECT NUMBER

5e. TASK NUMBER

5f. WORK UNIT NUMBER

7. PERFORMING ORGANIZATION NAME(S) AND ADDRESS(ES)

Naval Postgraduate School
Monterey, CA 93943

8. PERFORMING ORGANIZATION REPORT NUMBER

9. SPONSORING / MONITORING AGENCY NAME(S) AND ADDRESS(ES)

Department of the Navy

10. SPONSOR/MONITOR'S ACRONYM(S)

11. SPONSOR/MONITOR'S REPORT NUMBER(S)

12. DISTRIBUTION / AVAILABILITY STATEMENT

Approved for public release; distribution is unlimited

13. SUPPLEMENTARY NOTES

The views expressed in this thesis are those of the author and do not reflect the official policy or position of the Department of Defense or the U.S. Government. IRB Protocol number XXX.

14. ABSTRACT

Classically, the T-matrix method is a procedure to exactly compute the multiple scattering of an incident wave from a “cloud” of objects, given knowledge of the free-field scattering properties of a single object for an arbitrary incident wave. For acoustic waves, Profs. Baker and Scandrett have extended the T-matrix method to the case in which the radiation sources are also the scatterers, that is, to the case of an array of active transducers. This thesis is the first successful practical demonstration of the T-matrix method applied to an active sonar array for which a finite-element model was employed to compute the scattering properties of a single transducer. For validation, a T-matrix model of a linear array of piezoelectric spherical thin-shell transducers was modeled, for which analytical approximate values of the T-matrix element values are known. Subsequently, a T-matrix model of a linear array of piezoelectric class V flextensional “ring-shell” transducers was modeled. Beam patterns of the linear array models computed with the T-matrix method are compared with those of an array of point sources, demonstrating that the T-matrix method produces more realistic beam patterns, especially for end fire arrays.

15. SUBJECT TERMS

Active Sonar Array Modeling, T-matrix method, Array Interaction, Multi-scattering, Spherical Harmonic, Finite Element Modeling, COMSOL Multiphiyscs, Flextensional Transducer, Beampattern

16. SECURITY CLASSIFICATION OF:			**17. LIMITATION OF ABSTRACT**	**18. NUMBER OF PAGES**	**19a. NAME OF RESPONSIBLE PERSON**
a. REPORT	**b. ABSTRACT**	**c. THIS PAGE**			**19b. TELEPHONE NUMBER** *(include area code)*
Unclassified	Unclassified	Unclassified	UU	139	

THIS PAGE INTENTIONALLY LEFT BLANK

APPLICATION OF THE T-MATRIX METHOD TO THE NUMERICAL MODELING OF A LINEAR ACTIVE SONAR ARRAY

Erhan Ozer
Lieutenant Junior Grade, Turkish Navy
B.S., Turkish Naval Academy, 2007

Submitted in partial fulfillment of the
requirements for the degree of

MASTER OF SCIENCE IN ENGINEERING ACOUSTICS

from the

NAVAL POSTGRADUATE SCHOOL
June 2013

Author:	Erhan Ozer
Approved by:	Steven R. Baker Thesis Co-Advisor
	Clyde L. Scandrett Thesis Co-Advisor
	Daphne Kapolka Chair, Engineering Acoustics Academic Committee

THIS PAGE INTENTIONALLY LEFT BLANK

ABSTRACT

Classically, the T-matrix method is a procedure to exactly compute the multiple scattering of an incident wave from a “cloud” of objects, given knowledge of the free-field scattering properties of a single object for an arbitrary incident wave. For acoustic waves, Profs. Baker and Scandrett have extended the T-matrix method to the case in which the radiation sources are also the scatterers, that is, to the case of an array of active transducers. This thesis is the first successful practical demonstration of the T-matrix method applied to an active sonar array for which a finite-element model was employed to compute the scattering properties of a single transducer. For validation, a T-matrix model of a linear array of piezoelectric spherical thin-shell transducers was modeled, for which analytical approximate values of the T-matrix element values are known. Subsequently, a T-matrix model of a linear array of piezoelectric class V flextensional “ring-shell” transducers was modeled. Beam patterns of the linear array models computed with the T-matrix method are compared with those of an array of point sources, demonstrating that the T-matrix method produces more realistic beam patterns, especially for end fire arrays.

THIS PAGE INTENTIONALLY LEFT BLANK

Table of Contents

List of Figures

List of Tables

Acknowledgements

I would like to thank Prof. Steven R. Baker for his tireless effort and motivation throughout the research process. I thank you for all the advice, insight, support, and assistance. You were always available with expertise and practical experience that guided my work. I would also like to thank Prof. Clyde L. Scandrett for his guidance and assistance. I have always felt welcome in your office for questions or comments.

I gratefully acknowledge the many professors on the Acoustic Committee at the Naval Postgraduate School for their dedication and attention.

Last, but certainly not the least, I would like to thank my family. I want to dedicate this thesis to them for their endless support. In particular, I thank my wife, Tugba, for her sacrifice, understanding, and patience, as well as the enduring love she has given me every day.

THIS PAGE INTENTIONALLY LEFT BLANK

CHAPTER 1:
Introduction

1.1 Motivation

In many sonar applications, it is desirable to use a high power and directional sonar transducer. Their use reduces reverberation and can propagate further distances. Also, they provide more accurate estimate of bearing. These transducers are used in arrays in order to maximize the directionality and steer optimum acoustic beams. Figure 1.1 shows two examples of volumetric sonar array applications.

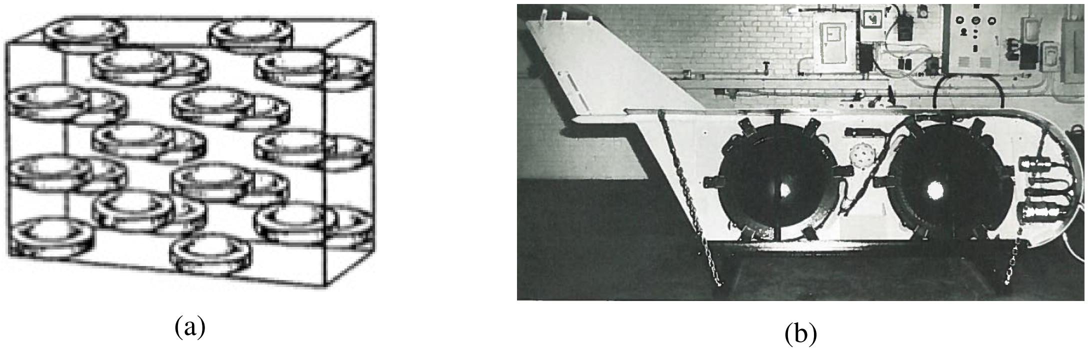
(a) (b)

Figure 1.1: (a) A bi-planar array containing of 24 Sparton of Canada 600 Hz class V flextensional transducers [1] (b) Bicycle Array composed two of the 610 Hz class V flextensional transducers [2]

The interaction between array elements can affect array performance. Especially, this effect becomes severe for high power and directional array elements because they are commonly operated at a resonance frequency and are spaced closely, typically no greater than $\lambda/2$ [8]. Accurate performance modeling of such an array requires proper accounting of the acoustic interaction between array elements.

Historically, the Pritchard's approximation [9] has been employed to evaluate inter-element array interactions. It has been employed to model a bi-planar array by the Naval Underwater Systems Center (NUSC, New London, CT; now the Naval Undersea Warfare Center, NUWC, Newport, RI) to predict the accurate beam pattern. Beam pattern predictions of computer models were then compared against results of deep water testing. Although the computer models resulted in much better beam patterns with regard to the non-interacting point sources model, it showed a significant deviation at and near end fire steering angles [8].

Another example of evaluating array interaction comes from a fundamental acoustic course at the Naval Postgraduate School (NPS). It is a three-element array with omnidirectional drivers that was investigated for several different configurations in an anechoic chamber. The investigation uncovered substantial deviation between theoretical and experimental results. In particular, near end fire, source-level amplitude data does not match theory, and the product theorem [10] cannot explain this discrepancy Figure 1.2.

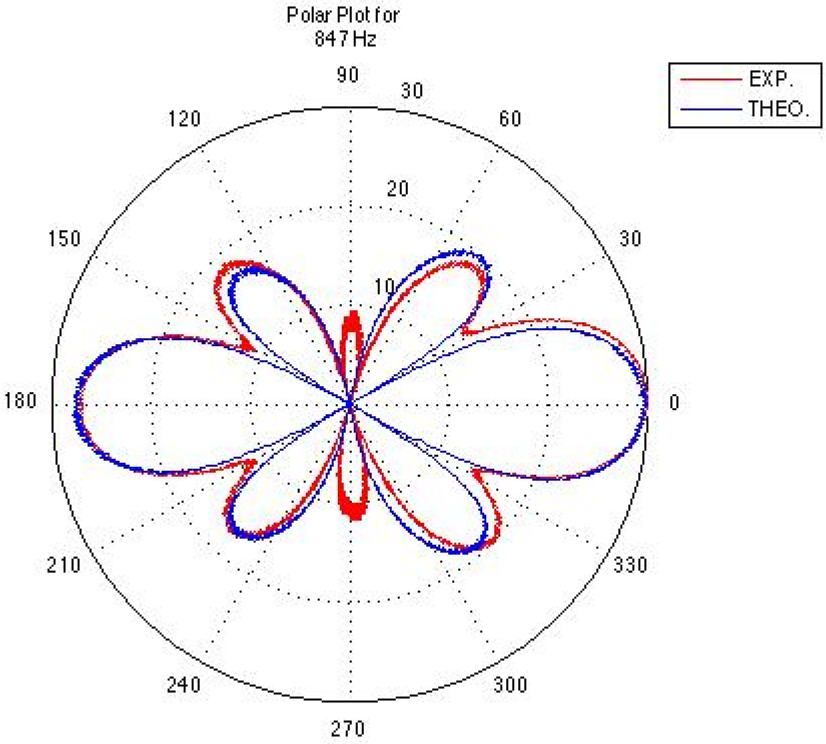

Figure 1.2: The far-field beam pattern for a three-element array with omnidirectional drivers [3]

In the early 1990s, a "T-Matrix Method" was developed by NPS researchers Prof. S. R. Baker and Prof. C. L. Scandrett [6,11] in order to properly model randomly and densely packed arrays of active sonar transducers.

To build an array model using the T-Matrix method, one must obtain the free-field radiation properties for a given electrical drive condition and the scattering properties (T-Matrix coefficients) for a single-transducer, from such as a finite-element model (FEM).

This thesis focuses on building a three-dimensional (3D) FEM of a volumetric piezoelectric transducer for T-matrix calculation in COMSOL and properly developing a model of a closely packed linear array by using the T-Matrix Method.

1.1.1 Related Works

Although the T-matrix method was first developed in the 1990s, it has not been applied to a realistic volumetric array model because, until now, the capabilities and user-friendliness of the finite-element computer codes available for performing the single-transducer radiation and scattering computations required for the T-matrix method were insufficient. Thus, the method was not of practical use to a non-specialist engineer. The attempt of prior theses to compute T-matrix elements using ATILA finite-element code resulted in excessive discrepancies in comparison to analytical results [12, 13].

Recently, that situation has changed. Using the COMSOL multiphysics finite-element computer code, finite-element model computations for the acoustic scattering T-matrix coefficients of a thin-wall elastic spherical shell now show excellent agreement with those computed using full 3D elasticity theory [14].

Therefore, the T-matrix method is applicable and can be used to build an exact model of densely and randomly-packed active sonar transducer array. Furthermore, this method can achieve a more accurate analysis of array performance that better defines the acoustic characteristics of the array.

1.2 Purpose

The purpose of the research described in this thesis is to demonstrate for the first time the practical application of the T-matrix method to the numerical performance modeling of an active sonar array, that is, to combine the results of finite-element model computations of the single-transducer free-field radiation and scattering characteristics with an analytic model for the free-field propagation between transducers. Specifically, the T-matrix method will be applied to model the source level and far-field beam pattern for several example unsteered linear active sonar arrays comprised of either 1) radially-polarized piezoelectric spherical thin-shell transducers or 2) type V flextensional "ring-shell" transducers, model 34A0610, manufactured by Sparton of Canada [7, 15]. The former was chosen as an academic example, as approximate analytic radiation and scattering properties for such transducers are known; the latter was chosen because it represents a real high-power, low-frequency sonar projector which was built and tested in a 24-element, densely-packed, bi-planar, active array, and for which single-element and array measured performance characteristics are available [7, 16]. Although only unsteered linear array configurations of 1/2-wavelength spacing and "ka"$\approx$1 were considered herein, the ultimate goal of the research program, of which the present effort is a contribution, is to compare the characteristics of the as-tested bi-planar array as computed using the T-matrix method to both its measured characteristics and its characteristics as computed using the so-called "Pritchard approximation" to model array element interaction [9].

1.3 Organization

The remainder of the thesis consists of six chapters.

Chapter 2 clarifies features of COMSOL's Acoustic Module and presents the addition theorem used in coordinate translation matrices for an array. The second part of chapter 2 describes the far-field beam pattern calculation for a linear array using the T-matrix method.

Chapter 3 describes the characteristic features of the modeled transducers which consist of a radially polarized spherical transducer and a type V Flextensional Ring-Shell Model 34A0610.

Chapter 4 is devoted to building 3D models of the radially polarized piezoelectric spherical thin-shell transducer and the type V flextensional ring-shell transducer. The second part of Chapter 4 includes an evaluation of sought-after transducer parameters from the 3D FEM model.

Chapter 5 calculates the total acoustic pressure field and produces the far-field beam pattern plots for equally spaced linear arrays using the T-matrix methodology.

Chapter 6 concludes this thesis and provides suggestions for future work.

1.4 Assumptions

Single-frequency harmonic time dependence of the form $e^{i\omega t}$ is assumed throughout this thesis. The symbol “i” is used for the imaginary unit to avoid confusion with the spherical Bessel function of the first kind, j_n.

CHAPTER 2:
Theory

2.1 COMSOL Finite Element Analysis

2.1.1 COMSOL Multiphysics

The COMSOL Multiphysics numerical package is a finite element code that includes simulation software capable of modeling many different physical phenomena employing a variety of different physics-based modules. The modules involve a solution method of Partial Differential Equations (PDE) and predefined multiphysics interfaces. Predefined multiphysics interfaces simplify the model by using a built-in coupled physics node. They undertake the analysis for different types of studies (e.g., modal, eigenfrequency, frequency response) [17].

2.1.2 The Acoustic-Piezoelectric Interaction Interface

The Acoustic-Piezoelectric Interaction Interface is one of the physical modes of COMSOL Multiphysics within the Acoustics Module. This module can solve the far-field or near-field radiation problem by incorporating acoustic-structure interactions of piezoelectric materials [18]. The boundary conditions include the pressure load from fluid to solid and a structural acceleration between the solid and fluid. The Acoustic-Piezoelectric Interaction Interface combines the piezoelectric device, pressure acoustics, frequency domain, solid mechanics, and electrostatic interfaces [18].

2.1.3 Acoustics Interface Theory in COMSOL Multiphysics

The acoustic wave equation is expressed in COMSOL by the following equation [18]:

$$\frac{1}{\underbrace{\rho c^2}_{\substack{Bulk\\Modules}}}\frac{\partial^2 p}{\partial t^2} + \nabla \cdot \left(-\frac{1}{\rho}\left(\nabla p - \mathbf{q}_d\right)\right) = Q_m \tag{2.1}$$

Variable	Description	Unit
ρ	Fluid Density	kg/m^3
c	Speed of Sound	m/s
p	Pressure	Pa
$\mathbf{q_d}$	Dipole Source	N/m^3
Q_m	Monopole Source	1/s^2

In the case of plane waves, the pressure varies with time as

$$p(x,t) = p(x)e^{i\omega t}. \tag{2.2}$$

The assumption of the frequency domain or time-harmonic dependence for the acoustic wave equation results in the inhomogeneous Helmholtz equation [18]:

$$\nabla \cdot \left(-\frac{1}{\rho} \left(\nabla p - \mathbf{q}_d \right) \right) - \frac{\omega^2 p}{\rho c^2} = Q_m \tag{2.3}$$

Boundary conditions are required to solve the inhomogeneous Helmholtz equation. COMSOL provides several different types of boundary conditions, depending upon the analysis performed. The prescribed boundaries between the fluid-solid boundary are added after nodes are selected and fixed. Three built-in boundary conditions are available [18] on the boundaries between the fluid and solid:

1. free
2. sound hard boundary(wall)
3. acoustic structure boundary

A *free boundary condition* assumes the medium reacts without any constraints acting on the boundary.

A *sound hard boundary* is added for a rigid boundary. With this boundary condition, the normal component of differential velocity is zero [18]. This boundary condition is also named the Neumann condition:

$$\mathbf{n} \cdot \left(\frac{1}{\rho_0} \left(\nabla p - \mathbf{q}_d \right) \right) = 0 \tag{2.4}$$

An *acoustic structure boundary* couples the fluid load and structural acceleration at the fluid-solid boundary. It cannot be added to other boundaries [18].

$$\begin{aligned}\mathbf{F}_p &= -\mathbf{n}p \\ a_n &= \mathbf{n}\cdot\mathbf{u}_{tt}\end{aligned} \tag{2.5}$$

Variable	Description
$\mathbf{F}$	Force
p	Pressure
n	Unit normal,outward pointing from solid domain
a_n	Normal acceleration for the acoustic fluid
$\mathbf{u_{tt}}$	Second derivative of the Structural Displacement with respect to time

2.1.4 Piezoelectric Device Theory in COMSOL Multiphysics

Piezoelectric materials are solids for which the mechanical strain and the electric field in the solid influence each other. Changes in strain or electric field cause responses of the polarization and stress within the solid. For example, an applied potential difference induces a deformation of the piezoelectric device, and/or the deformation of the piezoelectric material induces an electrical potential difference within the piezoelectric device. The piezoelectric relations for linear systems having small strains are expressed by the following equations in COMSOL [18].

Strain-Charge :

$$\mathbf{S} = s_E\mathbf{T} + d^T\mathbf{E} \tag{2.6}$$

$$\mathbf{D} = d\mathbf{T} + \varepsilon_T\mathbf{E} \tag{2.7}$$

This relation can be rewritten into stress-charge form as

Stress-Charge:

$$\mathbf{T} = c_E\mathbf{S} - e^T\mathbf{E} \tag{2.8}$$

$$\mathbf{D} = e\mathbf{S} + \varepsilon_S\mathbf{E} \tag{2.9}$$

Piezoelectric ceramics are “transverse isotropic” materials [19]. In material science, orthogonal axes, designated “1,” “2,” and “3” are defined by convention for a given material type. The polarization is conventionally designated as the “3” direction, and COMSOL uses the same convention for piezoelectric devices.

The piezoelectric material properties are expressed in stiffness, compliance, coupling, and dielectric matrices with respect to their local coordinate system. The default local coordinate system corresponds to the Cartesian coordinate system [17].

Variable	Description
T	Stress
S	Strain
D	Electrical displacement
s_E	Elastic compliance constant
c_E	Elastic stiffness constant
ε_S	Dielectric constant
e	Piezoelectric stress constant
d	Piezoelectric strain constant

2.2 Piezoelectric Spherical Thin-Shell Transducer

The spherical thin shell transducer is a particular transducer in which the spherically symmetric mode (lumped constant mode) can be developed from an equation of motion rather than a wave equation (Figure 2.1) [4, 20]. Therefore, fundamental acoustic features (e.g, mechanical Q, radiation load) of a thin shell transducer can be accurately represented by a simple closed form expression. The equivalent circuit [4] represents a model of a thin shell transducer (Figure 2.2). Hence, it is particularly convenient for illustrating equivalent circuits and design principles [20].

A radially polarized spherical thin shell transducer of mean radius "*a*", and thickness "*t*" is modeled. The radial direction coincides with the material ”3“ direction. Electrodes are located on the inner and outer surfaces of the sphere to form equipotential surfaces. Hence, transverse fields E_1 and E_2, which are perpendicular to the radial direction, are neglected. All of the tensile stresses are equal to zero except the circumferential tensile stress T_1 [4, 19]. The relationship between strain and stress forces in the "1" and "2" directions are obtained from symmetry The relationship between strain and stress forces in the 1 and 2 directions are obtained from symmetry

$$T_1 \equiv T_2 \equiv T_c$$

$$S_1 \equiv S_2 \equiv S_c.$$

Compliance coefficients are combined to form a circumferential compliance coefficient ex-

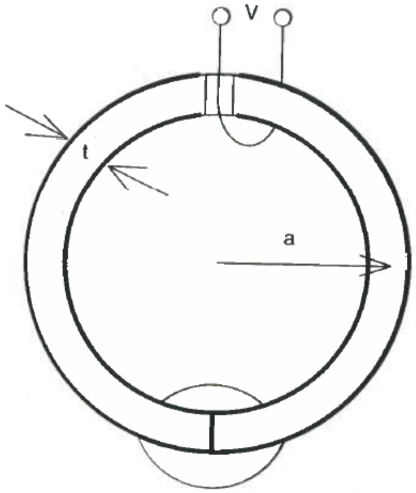

Figure 2.1: Radial cross section of a radially polarized piezoelectric spherical thin shell transducer

pressed as

$$s_c^E = \frac{1}{2}\left(s_{11} + s_{12}\right). \tag{2.10}$$

The piezoelectric equations are then

$$S_c = 2s_c^E T_c + d_{31} E_3 \tag{2.11}$$

$$D_3 = 2d_{31} T_c + \varepsilon_{33}^T E_3. \tag{2.12}$$

The electrical displacement equation can be expressed by substituting in equation (2.11)

$$D_3 = \frac{d_{31}}{s_c^E} S_c + \varepsilon_{33}^T \left(1 - {k_p}^2\right) E_3. \tag{2.13}$$

Where

$${k_p}^2 = \frac{{d_{31}}^2}{\varepsilon_{33}^T s_c^E}. \tag{2.14}$$

The circumferential strain equals the ratio of the radial displacement to mean radius of the sphere

$$S_c = \frac{\xi}{a}. \tag{2.15}$$

The radial displacement can be obtained from the equation of motion, which is derived from

Newton's Second Law

$$F_r + \rho wta\delta\theta \frac{\partial^2 \xi}{\partial t^2} = 0$$

where,

$$F_r = F\delta\theta = 2T_c wt\delta\theta.$$

The equation of motion becomes

$$\rho wta\delta\theta \frac{\partial^2 \xi}{\partial t^2} = -2T_c wt\delta\theta. \tag{2.16}$$

The equation of motion can be expressed using differentials by substituting Equations (2.11) and (2.15) into Equation (2.16)

$$\frac{\partial^2 \xi}{\partial t^2} + \frac{1}{a^2 \rho s_c^E}\xi = \frac{d_{31}}{a\rho s_c^E} E_3. \tag{2.17}$$

The free resonance frequency of the undriven sphere (E=0) can be written from 2.17

$$\omega_0^2 = \frac{1}{a^2 \rho s_c^E}. \tag{2.18}$$

The spherical shell displacement for harmonic excitation is then expressed as

$$\xi = \frac{a d_{31} \omega_0^2 E_0 e^{i\omega t}}{\omega_0^2 - \omega^2} = \frac{a d_{31} \omega_0^2 E_3}{\omega_0^2 - \omega^2}. \tag{2.19}$$

After using the relationship between symmetrical strain and spherical shell displacement, $S_c = \xi/a$, this equation can be written in a more convenient form for computing the current, $I = 4\pi a^2 \dot{D}$,

$$D_3 = E_3 \left(\frac{d_{31}}{s_c^E} \frac{S_c}{E_3} + \varepsilon_{33}^T \left(1 - {k_p}^2\right) \right) \tag{2.20}$$

so

$$I = 4\pi a^2 i\omega E_3 \left(\frac{d_{31}}{s_c^E} \frac{S_c}{E_3} + \varepsilon_{33}^T \left(1 - {k_p}^2\right) \right). \tag{2.21}$$

The electrical admittance can be obtained from equation (2.21)

$$\frac{I}{V} = \frac{1}{Z} = \frac{4\pi a^2 i\omega}{t} \left(\frac{{d_{31}}^2}{s_c^E} \frac{\omega_0^2}{\left(\omega_0^2 - \omega^2\right)} + \varepsilon_{33}^T \left(1 - {k_p}^2\right) \right). \tag{2.22}$$

The equivalent circuit for a spherical ring, Figure 2.2, can be obtained for the electrical admittance.

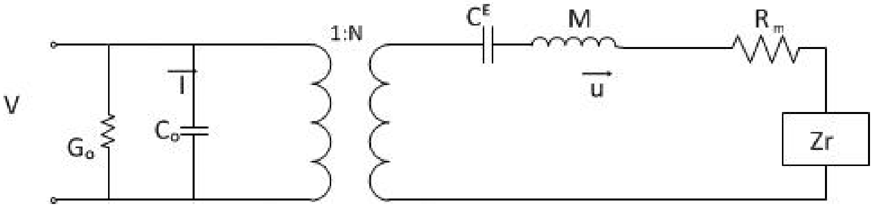

Figure 2.2: Equivalent circuit for a spherical transducer [4]

for which the electrical element values are:

$$\begin{aligned}
&N = \tfrac{4\pi a d_{31}}{s_c^E}\\
&M = 4\pi a^2 t\rho\\
&C_o = \tfrac{4\pi a^2 \varepsilon_{33}^T\left(1-k_p^2\right)}{t}\\
&C_m^E = \tfrac{s_c^E}{4\pi t}\\
&Z_r = \rho_o c S \tfrac{ika}{1+ika}\\
&S = 4\pi a^2
\end{aligned} \tag{2.23}$$

Element	Description
G_o	Electrical loss conductance
C_o	Open-circuit capacitance
N	Electromechanical turns ratio
C_m^E	Short-circuit compliance
M	Lumped mass
R_m	Mechanical Resistance
Z_r	Free-field radiation impedance

2.3 Type V Flextensional Ring-Shell Transducer

Ring-shell flextensional transducers are desirable because of their ability to operate at low frequencies while generating high acoustic power. They also have higher operating depth than uncompensated flextensionals of similar size and weight [2]. Furthermore, they provide wide bandwidth and low mechanical quality factor, Q_m, which are very important characteristics for underwater applications.

A composite piezoelectric ceramic and steel ring is used as a motor element. The ring is sandwiched between two convex thin spherical shell caps Figure 2.3. The small motion of the ring causes a relatively large volume displacement of the shell. The ring-shell transducer is depth compensated and operates at low frequencies.

The desired resonance frequency can be obtained by adjusting the piezo-ring diameter. In order to compensate for the depth pressure, a water bladder is used. The bladder is opened to the ocean and adjusts the internal pressure according to the depth pressure. [15]

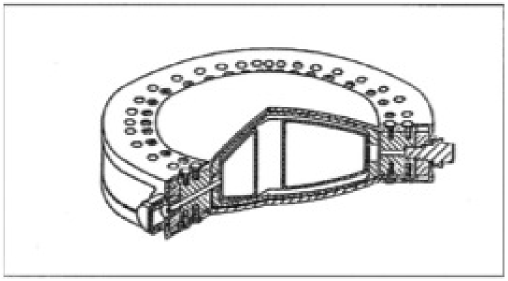

Figure 2.3: Cross Sectional View of Type V Flextensional Ring-Shell Transducer

2.4 T-Matrix Method

2.4.1 Introduction

Application of the T-Matrix method requires computation of the single-transducer scattering properties for an arbitrary incident wave. Since the incident pressure distribution is not known a priori, it, along with the single-transducer free-field radiation, is parametrized as a series expansion with to-be-determined coefficients using the free-field eigenfunctions of the linear wave equation in spherical coordinates. Outgoing waves (free-field radiated and scattered) are represented using outgoing traveling wave solutions (spherical Hankel functions), while incident waves are represented using standing wave solutions (spherical Bessel functions). Unnormalized spherical harmonic functions are used in all cases as an angular basis set, as shown in equations (2.24) and (2.25)

$$p^{i}(r,\theta,\phi)=\sum_{n}^{\infty}\sum_{m=-n}^{n}P_{nm}^{i}j_{n}(kr)\,\Omega_{n}^{m}(\theta,\phi) \tag{2.24}$$

$$p^s(r,\theta,\phi) = \sum_n^\infty \sum_{m=-n}^n P_{nm}^s h_n^{(2)}(kr)\,\Omega_n^m(\theta,\phi), \tag{2.25}$$

where

$\Omega_n^m(\theta,\phi) = P_n^m(\cos\theta)\,e^{im\phi}$.

Variable	**Description**
(r,θ,ϕ)	The spherical coordinates
P_{nm}^i	Incident pressure coefficient
P_{nm}^s	Scattered coefficient from the obstacle
$j_n(kr)$	n^{th} order spherical Bessel function
$h_n^{(2)}(kr)$	n^{th} order spherical Hankel function of the second kind
$\Omega_n^m(\theta,\phi)$	Unnormalized spherical harmonic function
$P_n^m(\cos\theta)$	Associated Legendre function of the first kind

To simplify further development, the following matrix notation will be employed. The spherical harmonic component coefficients for any quantity belonging to a single radiator are arranged in a column matrix, denoted using bold capital letter, e.g., by "flattening out" the double sequence over *n* and *m*, as follows

$$\mathbf{P^s} = \begin{pmatrix} P_{00}^s \\ P_{1-1}^s \\ P_{10}^s \\ P_{11}^s \\ \vdots \end{pmatrix} = \begin{pmatrix} P_1^s \\ P_2^s \\ P_3^s \\ P_4^s \\ \vdots \end{pmatrix}.$$

The one dimensional running index "*i*" of the column matrix equals

$$1 + n^2 + n + m$$

.

In principle, the length of such matrices may be infinite; however, in a practical computation, the number of spherical harmonics kept is truncated to a maximum value up to a certain degree, typically the second degree (quadrupolar, n=2) [6]. If the maximum spherical harmonic degree kept is n_{max}, the total number of spherical harmonic components kept is $N = (n_{\max}+1)^2$, e.g., 9 for $n_{max} = 2$.

2.4.2 Unnormalized Versus Normalized Spherical Harmonics

The unnormalized spherical harmonic function $\Omega_p^m(\theta,\phi)$ is related to the normalized spherical harmonic function $Y_n^m(\theta,\phi)$ [21];

$$Y_n^m(\theta,\phi) = C_{nm}\Omega_n^m(\theta,\phi) = C_{nm}P_n^m(\cos\theta)\exp(im\phi) \tag{2.26}$$

where

$$C_{nm} = (-1)^m \left[\frac{2n+1}{4\pi}\frac{(n-m)!}{(n+m)!}\right]^{1/2}. \tag{2.27}$$

Any function can be decomposed into a superposition of either normalized or unnormalized spherical harmonic functions [21]

$$f(\theta,\phi) = \sum_{n=0}^{\infty}\sum_{m=-n}^{n} a_{nm}Y_n^m(\theta,\phi) \tag{2.28}$$

where the constant a_{nm} is given by

$$a_{nm} = \int_0^{\pi}\int_0^{2\pi} [Y_n^m(\theta,\phi)]^* f(\theta,\phi)\, d\Omega \equiv C_{nm}I_{nm} \tag{2.29}$$

so

$$f(\theta,\phi) = \sum_{n=0}^{\infty}\sum_{m=-n}^{n} C_{nm}^2 I_{nm}\Omega_n^m(\theta,\phi)\ . \tag{2.30}$$

The orthonormality property of the associated Legendre equation is used for the limit 0 to π θ-dependent and 0 to 2π ϕ-dependent.

The I_{nm} is given by [14]

$$I_{nm} = \int_0^{\pi}\int_0^{2\pi} [\Omega_n^m(\theta,\phi)]^* f(\theta,\phi) d\Omega\ . \tag{2.31}$$

2.4.3 T-Matrix Calculation

The multiple scattering of acoustic waves by transducers in an array, to all orders, is rigorously and self-consistently accounted for by enforcing that the scattered component amplitudes at each transducer are related to the free-field incident component amplitudes from all other transducers by a transition, or T-, matrix

$$\mathbf{P^s} = [\mathbf{T}]\mathbf{P^i} \, . \tag{2.32}$$

Employing the matrix representation introduced in Section 2.4.1, this relationship can be expressed as

$$\begin{bmatrix} P_1^s \\ \vdots \\ \vdots \\ P_N^s \end{bmatrix} = \begin{bmatrix} T_{11} & \cdots & \cdots & \cdot \\ \vdots & \ddots & & \vdots \\ \vdots & & \ddots & \vdots \\ \cdot & \dots & \dots & T_{NN} \end{bmatrix} \begin{bmatrix} P_1^i \\ \vdots \\ \vdots \\ P_N^i \end{bmatrix} \tag{2.33}$$

where $N = (n_{\max} + 1)^2$.

The T-matrix elements are computed through a succession of scattering computations, as follows. An incident wave is imposed with unit amplitude in exactly one member (component) of the incident eigenfunction expansion, and the amplitudes of all members (components) of the scattered eigenfunction expansion found. This determines the member of exactly one column of the T-matrix. The T-matrix elements of that column equal the component pressure amplitudes. For example, to determine the first column of the T-matrix, elements denoted R_{nm} below, an incident wave with $P_{00}^i = 1$ and all other $P_{nm}^i = 0$ is imposed, and the resulting left hand side column matrix of scattered wave component coefficients P_{nm}^S determined by applying orthogonality of the unnormalized spherical harmonic functions (see Section 2.4.2 for details). If $p^s(a, \theta, \phi)$ is the scattered pressure amplitude at radius a in the fluid, then

$$P_{nm}^s = \frac{C_{nm}^2 I_{nm}}{h_n^{(2)}(ka)} \tag{2.34}$$

where

$$I_{nm} = \int_0^{\pi} \int_0^{2\pi} [\Omega_n^m(\theta, \phi)]^* p^s(a, \theta, \phi) \, d\Omega \, . \tag{2.35}$$

$$\begin{bmatrix} P^s_{00} \\ \vdots \\ \vdots \\ P^s_{nm} \end{bmatrix} = \begin{bmatrix} R_{00} & \cdots & \cdots & \cdot \\ \vdots & \ddots & & \vdots \\ \vdots & & \ddots & \vdots \\ R_{nm} & \cdots & \cdots & \cdot \end{bmatrix} \begin{bmatrix} 1 \\ \vdots \\ \vdots \\ 0 \end{bmatrix}, \tag{2.36}$$

where

$$R_{nm} = P^s_{nm} = \frac{C^2_{nm} I_{nm}}{h^{(2)}_n (ka)} \ . \tag{2.37}$$

This follows from setting

$$\sum_{n}^{\infty} \sum_{m=-n}^{n} P^s_{nm} h^{(2)}_n (ka) \, \Omega^m_n (\theta, \phi) = \sum_{n=0}^{\infty} \sum_{m=-n}^{n} C^2_{nm} I_{nm} \Omega^m_n (\theta, \phi) \ . \tag{2.38}$$

It should be noted that by its spherical symmetry property, the T-matrix for the spherical thin-shell transducer must be diagonal. Hence, the scattering cannot mix components. This is not exactly the case for the ring-shell transducer. By its axial symmetry property, scattering by the ring-shell transducer can mix "*n*" values, but not "*m*" values.

2.4.4 The Radiation Pressure Coefficient Calculation

In the absence of scattering, the free-field radiated pressure is expressed with the spherical Hankel function and unnormalized spherical harmonic function

$$P^R (r, \theta, \phi) = \sum_{n=0}^{\infty} \sum_{m=-n}^{n} P^R_{nm} h^{(2)}_n (kr) \, \Omega^m_n (\theta, \phi) \ . \tag{2.39}$$

The radiated pressure coefficients can be computed using the FEM. After comparing the spherical harmonic function expansion (2.28), the radiation pressure amplitude can be expressed in terms of I_{nm} as

$$P^R_{nm} = \frac{C^2_{nm} I_{nm}}{h^{(2)}_n (ka)} \ . \tag{2.40}$$

The right-hand side variable seems the same as the scattered pressure amplitude, but the surface integral (I_{nm}) in this case will be different as scattering has been neglected.

2.4.5 The Addition Theorem

In the case of an array, a single common coordinate system is inconvenient in applying boundary conditions. The spherical addition theorem must be used in this situation. It provides for a representation of a pressure field relative to one coordinate system in terms of another.

Consider two active spherical sources of radius "*a*" and separated by distance "*d*", as shown in Figure 2.4. The outgoing pressure of sphere two in mode (*n, m*) can be determined as a superposition of free-field incident pressures on sphere one in modes (*s, u*):

$$P^{out}_{n,m} h^{(2)}_n(kr_2)\, P^m_n(\theta_2,\phi_2) = \sum_s \sum_u P^i_{s,u}\, j^{(1)}_s(ka)\, P^u_s(\theta_1,\phi_1)\ , \tag{2.41}$$

where

$$\left(P^i_{s,u}\right) = [G_{12}]\left(P^{out}_{n,m}\right) \tag{2.42}$$

and G_{12} can be written from [5]

$$G^{2\rightarrow 1}_{(n,m)\rightarrow(s,u)} = \sum_{\substack{t=|n-s| \\ t\geq |m-u|}}^{n+s} a(s,t,n,u,m)\, h^{(2)}_t(kr_{12})\, \Omega^{m-u}_t(\theta_{12},\phi_{12})\ , \tag{2.43}$$

where

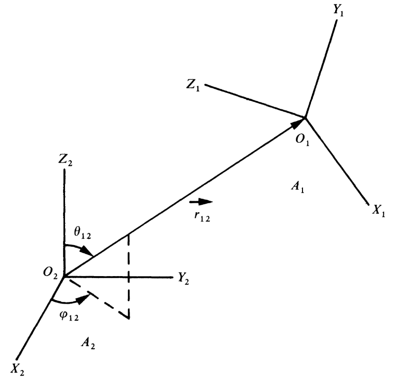

Figure 2.4: Two coordinate frames with arbitrary relative positions and orientations from [5]

$$
\begin{aligned}
a\left(s,t,n,u,m\right) = i^{s+t-n} & \left\{ \frac{\left(2s+1\right)\left(2t+1\right)\left(s-u\right)!\left(t-m+u\right)!\left(n+m\right)!\left[\left(s+t+n\right)/2\right]!}{\left[\left(n+t-s\right)/2\right]!\left[\left(n+s-t\right)/2\right]!\left[\left(s+t-n\right)/2\right]!\left(s+t+n+1\right)!} \right\} \\
& \cdot \sum_{w=w\min}^{w\max} \left(-1\right)^{w} \begin{pmatrix} s+t-n \\ \left(s+t-n\right)/2+w \end{pmatrix} \begin{pmatrix} t+n+-s \\ \left(t+n-s\right)/2+m-u+w \end{pmatrix} \\
& \cdot \begin{pmatrix} s+n-t \\ \left(s+n-t\right)/2-u+w \end{pmatrix}
\end{aligned}
$$

with

$$
\begin{pmatrix} a \\ b \end{pmatrix} = \frac{a!}{b!\left(a-b\right)!}
$$

$$
2w_{\min} = \max\left(n-s-t, s-n-t-2m+2u, t-s-n+2u\right)
$$

$$
2w_{\max} = \min\left(s+s-n, n+t-s-2m+2u, n+s-t+2u\right) \ .
$$

Variable	Description
r_{12}	the inter-element spacing distance,“*d*.”
θ_{12}	the polar angle of origin “1” with respect to origin “2”
ϕ_{12}	the azimuthal angle of origin “1” with respect to origin “2”

For a line array along the polar axis, which is all that will be considered herein, θ_{12} equals either 0 or π, and ϕ_{12} is “0”.

2.4.6 Total Acoustic Pressure Calculation

The multi-scattering of acoustic waves must be considered in the acoustic field calculation. The acoustic field is regarded as a superposition of outgoing waves from each transducer in the sonar array using the eigenfunctions of the wave equation in spherical coordinates as a basis set (e.g., spherical Hankel functions and spherical harmonics) centered at each array element. Outgoing wave components account for both the free field radiation, when a transducer is electrically energized, and the scattered field.

$$P^{out} = P^R + P^S \tag{2.44}$$

"Self consistency" is imposed, i.e., the incident pressure on one transducer is due to the outgoing pressure from all other transducers. This leads to a coupled set of linear equations in terms of the radiated and scattered pressure coefficients. For example, for two elements

$$\left(\mathbf{P_1^S}\right) = [\mathbf{T_1 G_{12}}] \left(\mathbf{P_2^R} + \mathbf{P_2^S}\right) \tag{2.45}$$

and

$$\left(\mathbf{P_2^S}\right) = [\mathbf{T_2 G_{21}}] \left(\mathbf{P_1^R} + \mathbf{P_1^S}\right) . \tag{2.46}$$

Variable	Description
$\mathbf{P}_l^{\mathbf{S}}$	Scattering pressure amplitude for l^{th} transducer
$\mathbf{G}_{lq}$	Translation formula from system q to system l
$\mathbf{T}_l$	Scattering pressure amplitude for l^{th} transducer
$\mathbf{P}_l^{\mathbf{R}}$	Free-field radiation pressure amplitude for l^{th} transducer

In the matrix form (2.45) and (2.46) can be expressed as

$$\begin{bmatrix} \mathbf{I} & -\mathbf{T_1 G_{12}} \\ -\mathbf{T_2 G_{21}} & \mathbf{I} \end{bmatrix} \begin{pmatrix} \mathbf{P_1^S} \\ \mathbf{P_2^S} \end{pmatrix} = \begin{pmatrix} \mathbf{T_1 G_{12} P_2^R} \\ \mathbf{T_2 G_{21} P_1^R} \end{pmatrix} . \tag{2.47}$$

The "α" matrix is defined as

$$\alpha = \begin{bmatrix} 0 & \mathbf{T_1 G_{12}} \\ \mathbf{T_2 G_{21}} & 0 \end{bmatrix} . \tag{2.48}$$

After substitution into (2.47) we get the simpler matrix form:

$$[\mathbf{I} - \alpha] \begin{pmatrix} \mathbf{P_1^S} \\ \mathbf{P_2^S} \end{pmatrix} = \alpha \begin{pmatrix} \mathbf{P_1^R} \\ \mathbf{P_2^R} \end{pmatrix} \tag{2.49}$$

or equivalently

$$\begin{pmatrix} \mathbf{P_1^S} \\ \mathbf{P_2^S} \end{pmatrix} = [\mathbf{I} - \alpha]^{-1} \alpha \begin{pmatrix} \mathbf{P_1^R} \\ \mathbf{P_2^R} \end{pmatrix} . \tag{2.50}$$

This result is easily generalized to the case of "N" transducers. The result is

$$\begin{pmatrix} \mathbf{P_1}^{\mathbf{S}} \\ \vdots \\ \mathbf{P_N^S} \end{pmatrix} = (\mathbf{I}-\alpha)^{-1}\alpha \begin{pmatrix} \mathbf{P_1^R} \\ \vdots \\ \mathbf{P_N^R} \end{pmatrix}$$

.

From this equation the scattering pressure amplitudes can be found.

The summation of the scattered and radiated pressure for each individual coordinate system of the transducer provides the total pressure at any field point with respect to a global origin in spherical coordinates.

$$p\left(r,\theta,\phi\right) = \sum_{l=1}^{N_{\mathbf{X}}} \sum_{n=0}^{n_{\max}} \sum_{m=-n}^{n} [P_{lmn}^{S} + P_{lmn}^{R}] h_n^{(2)}\left(kr_l\right) \Omega_n^m\left(\theta_l,\phi_l\right) , \tag{2.51}$$

where r_l, θ_l, and ϕ_l are the range, polar angle, and azimuth angle, respectively, of the field point with respect to the local coordinate axes of transducer "l." In all of the arrays considered herein, the local coordinate axes of all the transducers are assumed the same; only the origins differ in location. Hence, $\theta_l = \theta$ and $\phi_l = \phi$ for all "l."

2.4.7 Far Field Beam Pattern

A sonar array can be represented as a collection of arbitrarily-randomly and densely-packed acoustic transducers. An example for a sonar array is shown in Figure 2.5, a bi-linear array spherical thin shell transducer elements. The horizontal far-field beam pattern of this sonar array is represented in Figure 2.6 [6]. The amplitude of pressure is given in terms of a directional factor, $H(\phi)$, and the pressure amplitude along the acoustic axis of source, P_{ax},

$$P\left(r,\theta,\phi\right) = P_{ax}\left(r\right) H\left(\theta,\phi\right) . \tag{2.52}$$

The pressure amplitude change is proportional to $1/r$ in the far field, so equation (2.52) becomes

$$\lim_{r\to\infty} p\left(r,\theta,\phi\right) = \frac{P_{ax}\left(1\right) H\left(\theta,\phi\right)}{r} , \tag{2.53}$$

where

$$P_{ax}\left(1\right) = \lim_{r\to\infty} p\left(r,0,0\right) r$$

is the far-field, on-axis pressure amplitude, "referred" to a range of 1 m .

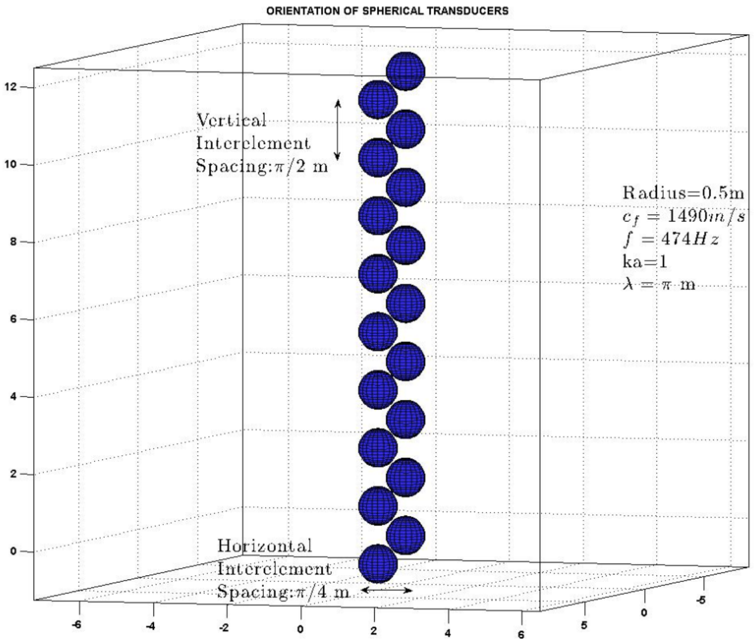

Figure 2.5: Orientation of the spherical transducers in the 16 element array

Equation (2.51) can be simplified using the asymptotic form of the spherical Hankel function, which can be derived from the standard Hankel function [22]

$$h_n^{(2)}(kr) = \sqrt{\frac{\pi}{2kr}} H_{n+\frac{1}{2}}^{(2)}(kr) \ . \tag{2.54}$$

In the far field, the asymptotic form of the Hankel function is inversely proportional to the square root of the distance

$$\lim_{r\to\infty} H_{n+\frac{1}{2}}^{(2)}(kr) = \sqrt{\frac{2}{\pi kr}} e^{-ikr} e^{-i\left(-\frac{\pi}{2}\left(n+\frac{1}{2}\right)-\frac{\pi}{4}\right)} \ . \tag{2.55}$$

So, the asymptotic spherical Hankel function can be written as

$$\lim_{r\to\infty} h_n^{(2)}(kr) = \sqrt{\frac{\pi}{2kr}} \sqrt{\frac{2}{\pi kr}} e^{-i\left(kr - n\frac{\pi}{2} - \frac{\pi}{2}\right)} \ .$$

After simplification it becomes

$$\lim_{r\to\infty} h_n^{(2)}(kr) = i^{(n+1)} \frac{e^{-ikr}}{kr} \ . \tag{2.56}$$

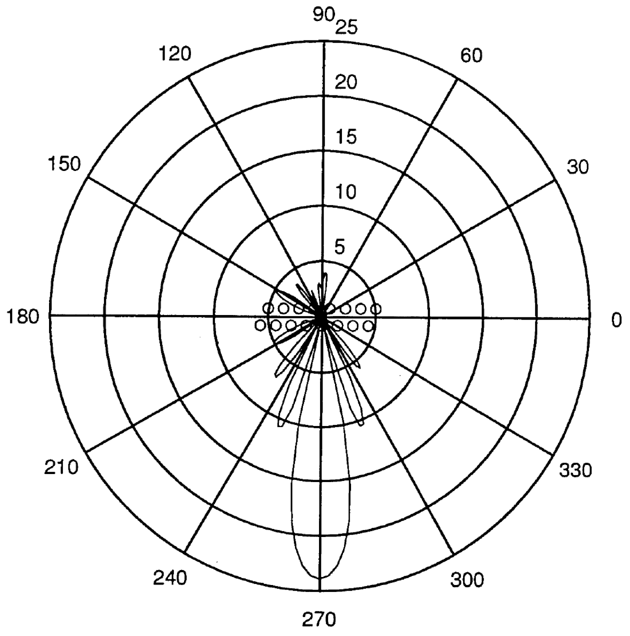

Figure 2.6: Source level of array, ka=1, analytically scaled by far-field of a single spherical transducer [6]

Applying this form to equation (2.51), and noting that "kr" above represents $\vec{k}\cdot\vec{r}$, the total acoustic pressure for the far-field limit can be obtained

$$p_{ff}(r,\theta,\phi) = \lim_{r\to\infty} p(r,\theta,\phi) = \sum_{l=1}^{N_{\mathbf{X}}} \frac{e^{-i\vec{k}\cdot(\vec{r}-\vec{r}_{Ol})}}{\vec{k}\cdot(\vec{r}-\vec{r}_{Ol})} \sum_{n=0}^{n_{\max}} i^{(n+1)} \sum_{m=-n}^{n} \left[P^S_{lmn}+P^R_{lmn}\right]\Omega^m_n(\theta_l,\phi_l)\,, \tag{2.57}$$

where the direction of $\vec{k}$ equals the direction of $\vec{r}$ and $\vec{r}_{Ol}$ is the vector position of the local origin of axes for transducer "l" with respect to the global origin.

In the far field, all radial vectors $(\vec{r}-\vec{r}_{Ol})$ are approximately parallel. The distance to the far field does not vary much for each element, so the factor r_{Ol} can be neglected compared to r in the amplitude factors (denominators). Although the path length difference can be ignored for amplitude, it has to be taken into account for phase. Factoring out the common phase $-kr$, the factor $\vec{k}\cdot\vec{r}_{Ol}$ is the phase difference between the global origin and the acoustic origin of transducer l. If the acoustic center of transducer l is located at (x_{Ol}, y_{Ol}, z_{Ol}),

$$\vec{k}\cdot\vec{r}_{Ol} = k_x x_{Ol} + k_y y_{Ol} + k_z z_{Ol}$$

which can be written as

$$\vec{k}\cdot\vec{r}_{Ol} = k\left(x_{Ol}\sin\theta\cos\phi + y_{Ol}\sin\theta\sin\phi + z_{Ol}\cos\theta\right) \ . \tag{2.58}$$

After the substitution of this equation into equation (2.57), the far-field total acoustic pressure equation is obtained

$$p_{ff}\left(r,\theta,\phi\right) = \frac{e^{-ikr}}{kr}\sum_{l=1}^{N_{\mathbf{X}}} e^{i\vec{k}\cdot\vec{r}_{Ol}} \sum_{n=0}^{n_{\max}} i^{(n+1)} \sum_{m=-n}^{n} \left[P^{S}_{lmn} + P^{R}_{lmn}\right] \Omega^{m}_{n}\left(\theta,\phi\right) \tag{2.59}$$

with $\vec{k}\cdot\vec{r}_{Ol}$ given by (2.58) .

THIS PAGE INTENTIONALLY LEFT BLANK

CHAPTER 3:

Spherical and Ring-Shell Transducer Descriptions

The radially polarized spherical thin-shell transducer and the class V flextensional ring-shell transducer are picked as example applications for the T-matrix calculation of a volumetric array transducer.

3.1 Piezoelectric Spherical Thin-Shell Transducer

The piezoelectric ceramic thin shell is polarized in thickness (radial) direction, and electrodes are installed on the inner and outer surface of the thin shell to provide radial polarization. The shell is made of lead zirconate titanate (PZT-8). This material is treated as a member of the Navy Type III. The Navy Type III is defined as "hard," which delineates a relative difficulty of depolarization of the ceramic [19]. PZT-8 is preferred for high powered transducers. The properties of PZT-8 are obtained from the COMSOL material library.

The thin shell is surrounded by a water. The inner domain of the thin shell is defined as air. The frequency of the transducer is defined with respect to "*ka*=1," which is the typical "*ka*" value of low frequency transducers [23]. Main operational and dimensional parameters are the following:

Parameter	**Value**	**Notation**
Frequency	474 Hz	f
Applied Electric Potential	1 V	V
Shell outer Radius	0.5 m	a
Shell thickness	0.01 m	t
Radiation boundary dimension	2.5 m	R

Table 3.1: The spherical thin-shell transducer dimensional and operational parameters

The thin-shell transducer can be properly represented by an equivalent circuit and the radiation load can be calculated by again using an equivalent circuit (See for details Chapter 2.2).

3.2 The Class V Flextensional Ring-Shell Transducer

The class V flextensional ring-shell transducer (Sparton Model 34A0610), is shown in Figure 3.1, and has been selected as a realistic model of a volumetric transducer. The ring-shell transducer is versatile in the case of low-frequency and high-power applications [2]. It is comprised of a composite piezoelectric ceramic and steel ring sandwiched between two thin convex-shaped steel shell segments. The radial motion of the piezoelectric ring causes large volume displacement over the shell and provides high acoustic output [15].

Figure 3.1: The depth-compensated ring shell projector [2]

3.2.1 Characteristics of the Transducer

The outer piezo-ring diameter is 81 cm. The ring is made of piezoelectric material (PZT-4), which is a motor element of the transducer. PZT-4 is classified as a "hard" ceramic type (Navy Type I) and is used primarily for high-powered transducers [19]. The piezo-ring consists of 144 plates of thickness-poled lead zirconate titanate, ceramic staves connected electrically in parallel. Rectangular-shaped ceramic staves are separated by 72 steel wedges to create an annular shape form [7]. Each steel wedge separates two bonded ceramic plates. Steel wedges are axially longer than ceramic staves in order to protect a ceramic surface from the stress that is caused by the shell edge [2]. A tension applied (25-40 MPa) fiber wrapping encloses the piezo-ring. The fiberglass wrapping is bonded with an epoxy resin. The fundamental operational characteristics of transducer are given by [1, 15, 24]

The piezoelectric elements are polarized tangentially and are connected in parallel. The polarization direction is shown in Figure 3.2.

In common with the flextensional transducer, the operating depth of the ring-shell projector is limited to a few meters without a depth compensating system. Different systems (e.g., liquid, compliant tubes, self-supporting, etc.) may be used to overcome the depth limited operation. The class V flextensional ring-shell projector is depth compensated by an internal water bladder that is opened to the sea through the water inlet [15]. The water bladder is installed into the

Parameter	**Value**
Frequency	610 Hz
Maximum Source Pressure Level	213 dB re 1 μPa at 1 m (driven by 3000 Vrms)
Efficiency	%90 at resonance, %65 at -6 dB
Operational Depth	Exceeds 400 m
Bandwidth at Resonance(-3 dB points)	>140 Hz (470 Hz to 750 Hz)

Table 3.2: Ring-Shell Transducer Operation Characteristic

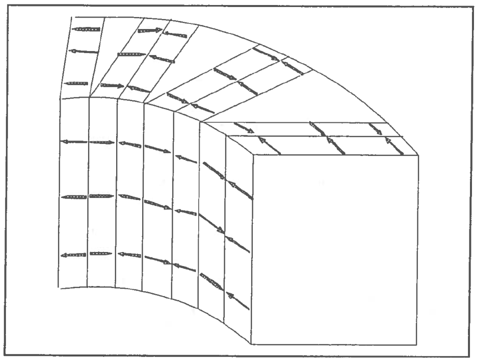

Figure 3.2: Original piezo-ring polarization [7]

interior cavity of the shell segments (Figure 3.3). The air domain between the shell segments is compressed by the water bladder with respect to the depth pressure. The water bladder depth compensation system decreases the damping and supports shells against the depth pressure without constraining motion of the shell.

The in-air weight without a foundation is 245 kg, while the in-water weight is 272 kg.

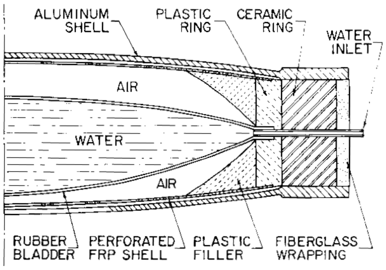

Figure 3.3: Cross sectional view of ring shell projector [2]

THIS PAGE INTENTIONALLY LEFT BLANK

CHAPTER 4:
The 3D Models

The numerical finite-element models of a radially polarized thin-shell spherical transducer and a class V flextensional ring-shell transducer were developed using the COMSOL Multiphysics version 4.3a finite-element code [25]. The acoustic-piezoelectric interaction , frequency domain interface of the acoustic module was selected using multi-physics because the fluid-structure coupling properties are enhanced at boundaries (See Chapter 2.1.3 for details).

The development of models is comprised of the following steps:

1. Selection of the COMSOL module and physics interface
2. Adding the required type of analysis (i.e,frequency domain, eigenfrequency, frequency-domain modal)
3. Creating a geometry in the selected space dimension (i.e, 3D, 2D, 2D axisymmetric)
4. Setting material properties
5. Assigning material geometrically
6. Applying the physics interaction to the model
7. Meshing
8. Computation
9. Post processing

4.1 General Model Settings

Development settings are the same for both models.

1. The built-in acoustic-piezoelectric interaction,frequency domain interface (ACPZ) was used. This interface couples the field boundary conditions between fluid and the piezoelectric material. The normal component of acceleration over the piezoelectric material's surface generates sound within the fluid. Inversely, the piezoelectric material undergoes a mechanical distortion due to applied fluid acoustic pressure over its surface [18].

2. The free-field incident waves are referred to as "*the background pressure field*" in COMSOL [18]. The background pressure field is defined for each spherical harmonic component (n, m). In each computational run, exactly one incident component is applied within the fluid domain. The incident pressure amplitude was set to "1" so the incident standing wave equation (2.24) becomes

$$P^i(r,\theta,\phi) = \sum_n^{\infty} \sum_{m=-n}^{n} j_n(kr)\,\Omega_p^m(\theta,\phi) \ .$$

3. The spherical wave radiation condition is applied on the outer boundary of the fluid domain at radius 2.5 m to reduce the reflection on the boundary and to truncate the numerical domain. It models acoustic propagation without reflection from the boundary.

4. The reference pressure for sound pressure level (SL) was selected as water (1μ Pa) from the SL settings window in COMSOL.

5. The maximum size of mesh elements was limited with respect to the wavelength of sound in water. To achieve a reliable solution, the wavelength has to be resolved by a 10-12 degrees of freedom (DOFs) corresponding to six elements in a wavelength. In other words, the mesh element size should be no larger than $\lambda/5$ [18]. This criteria was applied strictly to each mesh sequence.

6. The T-matrix elements were calculated for monopole, dipole, and quadrupole spherical harmonic components.

7. Two studies have been examined in each model, i.e, study 1 for calculation of the single-element free-field radiated pressure while study 2 corresponds to determination of the T-matrix elements, each using the post processing feature.

System Requirements

The Apple iMac MC813LL/A employed for COMSOL has the following technical specifications:

a. 2.7 Ghz Intel Core i5 processor

b. 32 GB 1333 MHz DDR3 memory

4.2 The Spherical Thin-Shell Transducer

The main purpose for building a model of the radially polarized piezoelectric spherical thin-shell transducer is to calculate the elements of its T-matrix and the coefficients of its free-field radiated pressure. The validation of the COMSOL Multiphysics ACPZ interface was evaluated by comparing the obtained values of the free-field radiated pressure field at the surface of the spherical thin-shell transducer with an equivalent circuit model of a spherical transducer.

4.2.1 Geometry

The thickness of the model shell is 0.01 m and has a radius of 0.5 m. The piezoelectric ceramic is surrounded by water (Figure 4.1). The cavity of the thin-shell is air filled.

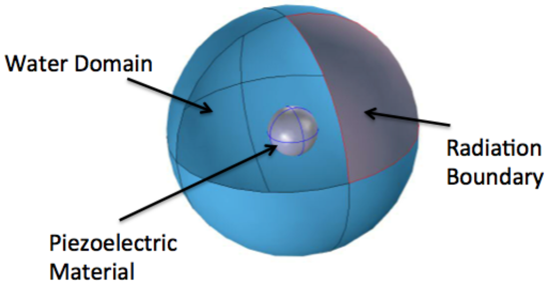

Figure 4.1: Pictorial representation of the 3D spherical thin-shell transducer and fluid domain.

The non-dimensional parameter *ka*=1 was selected to simulate the typical transducer operating condition and the frequency was adjusted to enforce *ka*=1. The model parameters can be seen in Table 3.1.

The surfaces of the spherical thin-shell were covered with electrodes. The inner surface of thin-shell was grounded while the outer surface was driven by a 1 V peak amplitude potential (Figure 4.2).

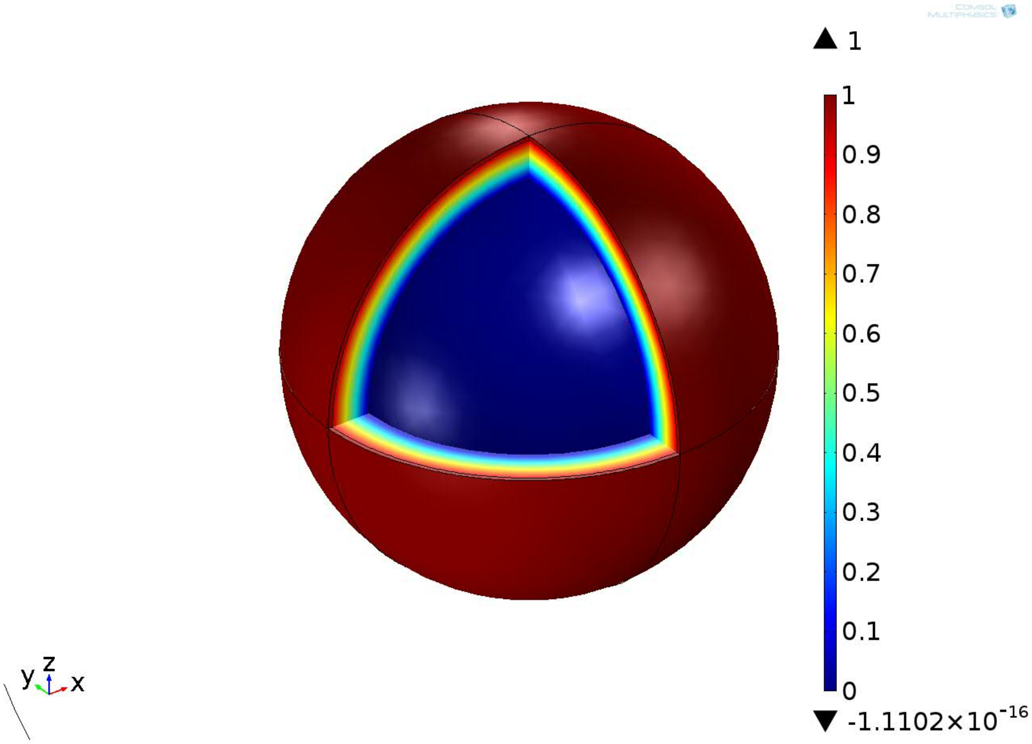

Figure 4.2: Electric potential of the thin-shell

4.2.2 Material

Three different material types were assigned to the geometry.

Lead Zirconate Titanate(PZT-8)

Properties of PZT-8 were assigned to the spherical shell. It is a very common piezoelectric material also known as a Navy Type III that is often used for power transducers. This material provides a maximum strength against high tensile forces. Material properties are already built into the COMSOL Material Library, and are shown in Table 4.1.

The default polarization direction is defined along the “*z*” axis in COMSOL [18], but in the present case, the polarization direction is radial. In order to obtain this polarization a user-defined base vector system was added to the “definition” branch .

Parameter	**Value**	**Unit**	**Notation**
Density	7600	kg/m^3	ρ
Compliance Matrix			
s^E_{11}	11.5	10^{-12}m^2/N	
s^E_{12}	-3.7	10^{-12}m^2/N	
s^E_{13}	-4.8	10^{-12}m^2/N	
s^E_{33}	13.5	10^{-12}m^2/N	
s^E_{44}	31.9	10^{-12}m^2/N	
s^E_{66}	30.4	10^{-12}m^2/N	
Coupling Matrix			
d_{31}	-97	10^{-12}C/N	
d_{33}	225	10^{-12}C/N	
d_{15}	330	10^{-12}C/N	
d_{15}	330	10^{-12}C/N	
Relative Permittivity			
$\varepsilon^T_{11}/\varepsilon_0$	1290		
$\varepsilon^T_{33}/\varepsilon_0$	1000		
ε_0	8.85	10^{-12}F/M	

Table 4.1: PZT-8 material properties (From the COMSOL material library)

The spherical coordinate system was defined using the unit basis vector (**i, j, k**) [21]

$$\begin{aligned}
\mathbf{x_1} &= \hat{\mathbf{e}}_\theta = \cos\theta\cos\phi\,\mathbf{i} + \cos\theta\sin\phi\,\mathbf{j} - \sin\theta\,\mathbf{k} \\
\mathbf{x_2} &= \hat{\mathbf{e}}_\phi = -\sin\phi\,\mathbf{i} + \cos\phi\,\mathbf{j} \\
\mathbf{x_3} &= \hat{\mathbf{e}}_r = \sin\theta\cos\phi\,\mathbf{i} + \sin\theta\sin\phi\,\mathbf{j} + \cos\theta\,\mathbf{k}\ .
\end{aligned} \tag{4.1}$$

After the spherical coordinate system was added in the definition branch, it was selected as a coordinate system from the selection menu in the material properties window.

The $\mathbf{x_3}$ unit vector of the spherical coordinate system shows the polarization direction, and in this model it is referred to as the radial direction.

Water

Water was used to define the fluid domain which surrounds the transducer. The material properties were assigned as shown in Table 4.2.

Parameter	**Value**	**Notation**
Density	1000 kg/m^3	ρ
Speed of Sound	1490 m/s	c

Table 4.2: Water material properties

Air

Air was added to define the interior cavity of the thin-shell. The material properties are built into COMSOL.

4.2.3 Meshing

User-controlled meshing was used for the sequence type to control and optimize the numerical mesh. The "free mesh" algorithm is preferred over the geometry. The spherical transducer domain and fluid domain used a finer mesh size employing tetrahedral elements. The entire model consists of 421,598 elements (Figure 4.3). The average mesh quality is 0.73 where the quality measure is a number between 0 and 1 (Figure 4.4). An acceptable mesh quality is typically larger than 0.1 according to the COMSOL user's manual [17].

According to the COMSOL user's manual, the maximum element size of mesh should be smaller than $\lambda/5$ (0.628 m in water at 474 Hz) in an acoustical model [18]. We have chosen the maximum element size of the mesh to be $\lambda/11.5$ or 0.273 m which ensures accuracy. The statistical mesh quality for boundaries is represented in Table 4.3

Boundaries	Element Type	Amount	Avg. Element Quality
Radiation	Triangular	2,852	0.98
Piezo material outer	Triangular	19,416	0.99
Piezo material inner	Triangular	18,504	0.99

Table 4.3: The meshing properties of the 3D spherical transducer model with a "finer mesh" size for all domains.

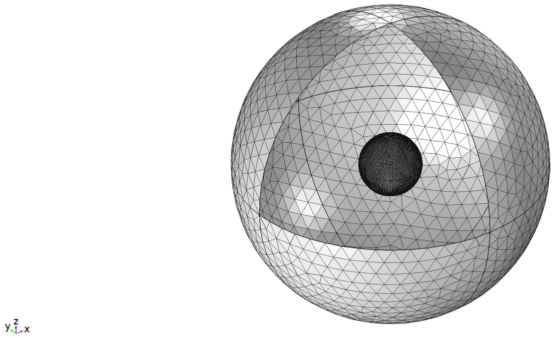

Figure 4.3: 3D spherical transducer model meshing

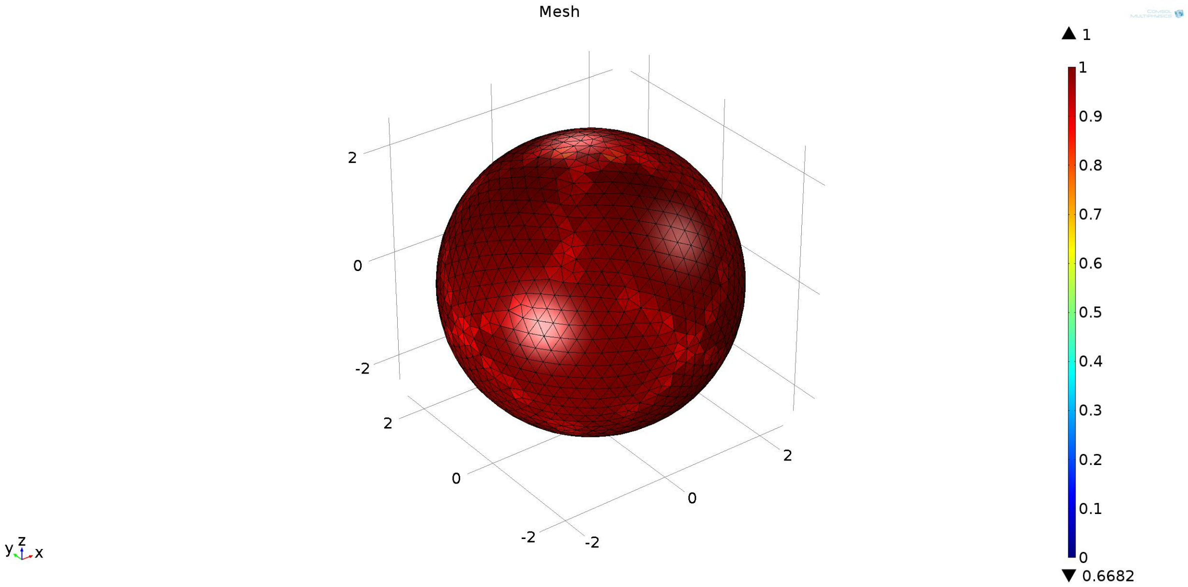

Figure 4.4: Mesh quality of the model

4.2.4 The Free-Field Radiated Acoustic Pressure Field

The free-field radiated acoustic pressure field is plotted versus the on-axis distance from the thin-shell transducer surface. Figures 4.5 and 4.6 show the spatial free-field radiated acoustic field. Pressure magnitude, refer to one meter was found as

$$P(1) \equiv r\,p = 9.76\ Pa.m\ .$$

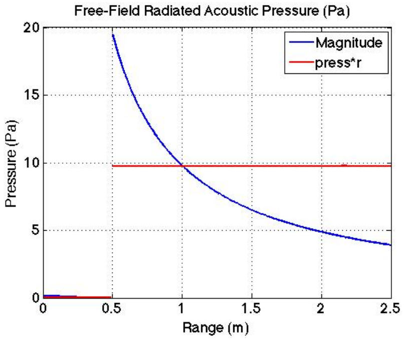

Figure 4.5: The free-field radiated acoustic pressure field (magnitude) vs distance from the center of the spherical thin-shell transducer

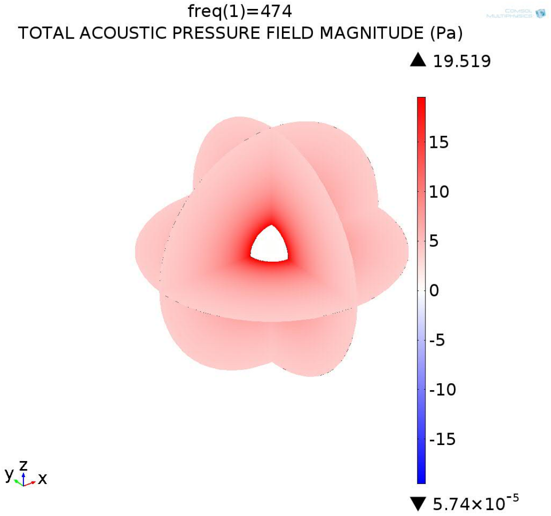

Figure 4.6: The multi-slice plot of the free-field acoustic radiated field (magnitude) in "Pa" for a modeled spherical thin-shell transducer

4.2.5 Approximate Analytical Radiation Pressure Calculation for a Thin-Shell Transducer

The free-field radiated acoustic pressure can be expressed by the product of the mechanical radiation impedance, Z_r, and the surface velocity, u, integrated over the surface of the transducer

$$p = \frac{Z_r u}{4\pi a^2} \,. \tag{4.2}$$

The radiation impedance for the monopole sphere which has a uniform, radial velocity distribution and uniform pressure on the surface is given as [4]

$$Z_r = 4\pi a^2 \rho c \tfrac{(ka)^2 + ika}{1 + (ka)^2} \tag{4.3}$$

and the velocity over the spherical transducer surface can be calculated by using an electrical equivalent circuit for the spherical transducer (Figure 2.2). In this figure of the equivalent circuit, the right side of the transformer contain the components of the mechanical impedance. R_m is negligible compared to the stiffness and the compliance, so the mechanical impedance becomes approximately

$$Z_m = i\left(\omega M - \frac{1}{\omega C_m^E}\right) \tag{4.4}$$

with velocity

$$u = \frac{NV}{(Z_r + Z_m)}\ , \tag{4.5}$$

where NV is the piezoelectric driving force.

The lumped mass, M, the mechanical compliance, C_m^E, and the electromechanical turns ratio, N, can be obtained from equation (2.23).

The total surface acoustic radiated pressure is calculated by substitution of equation (4.3) and (4.5) into equation (4.2). Comparison of the results for an analytical calculation and the COMSOL computation are shown in Table 4.4.

Method	Real	Imag	Amp
approximate analytical solution	-9.6	17.88	20.29
COMSOL Result	-9.4	17.11	19.52

Table 4.4: Comparison of the free-field radiated pressure at the surface of the spherical transducer computed in COMSOL against those calculated from an equivalent circuit.

The results in Table 4.4 show that the COMSOL result and the approximate analytical solution are in agreement. The magnitude value of the COMSOL result differs by 3.7 percent from the approximate analytical solution. This is an acceptable difference, since the approximate analytical solution is derived from the equivalent circuit model of a spherical transducer, based on the assumption that its small cross-sectional dimensions are negligible when compared with its radius and with no internal losses [20], whereas the COMSOL model is fully three-dimensional. The approximate solution does provide insight as to the physical behavior of the transducer.

4.2.6 T-Matrix Calculation

Nine different spherical harmonic components (n=0,1,2 m=-n..n) of an incident wave pressure were used in defining the background pressure field. The amplitude of a given incident wave pressure mode was set to "1" with the remaining mode amplitudes set to zero and scattered component amplitudes computed (see Section 2.4.3 for details). For example, to determine the first column of the T-matrix, an incident wave with $P^i_{00} = 1$ and all other $P^i_{nm} = 0$ is imposed. Then resulting column matrix of scattered wave component calculated using (4.6)

$$R_{nm} = \frac{C^2_{nm} I_{nm}}{h^{(2)}_n (ka)} \tag{4.6}$$

and

$$\begin{bmatrix} P^s_{00} \\ \vdots \\ \vdots \\ P^s_{nm} \end{bmatrix} = \begin{bmatrix} R_{00} & \cdots & \cdots & \cdot \\ \vdots & \ddots & & \vdots \\ \vdots & & \ddots & \vdots \\ R_{nm} & \dots & \dots & \cdot \end{bmatrix} \begin{bmatrix} 1 \\ \vdots \\ \vdots \\ 0 \end{bmatrix} . \tag{4.7}$$

Evaluation of the surface integrals were performed at the surface of the spherical thin-shell transducer using the solution data set. One column of the T-matrix was derived from each computation, so nine computations were undertaken in order to complete the T-matrix. The T-matrix of a spherical thin-shell shell transducer is given in Table 4.5. The accuracy of the T-matrix can be determined by examining the non-diagonal elements because the applied single-component of incident wave should theoretically result in only the same harmonic component

T-matrix Elements

	P^i_{00}	P^i_{1-1}	P^i_{10}	P^i_{11}	P^i_{2-2}	P^i_{2-1}	P^i_{20}	P^i_{21}	P^i_{22}
P^s_{00}	**6.91E-02**	2.60E-08	1.18E-08	7.36E-08	7.51E-08	4.51E-07	1.94E-06	6.99E-06	2.81E-06
P^s_{1-1}	3.23E-08	**7.43E-02**	3.32E-08	5.22E-08	8.74E-08	3.99E-08	8.45E-07	2.41E-06	3.98E-06
P^s_{10}	4.33E-09	1.37E-08	**7.43E-02**	3.31E-08	1.13E-07	8.15E-08	3.44E-07	5.07E-07	2.47E-06
P^s_{11}	9.92E-09	2.10E-09	1.37E-08	**7.43E-02**	1.03E-07	1.84E-07	3.66E-07	9.32E-08	1.40E-06
P^s_{2-2}	7.00E-07	1.19E-06	2.18E-06	3.50E-06	**9.21E-01**	1.01E-04	1.07E-04	5.55E-05	9.18E-04
P^s_{2-1}	2.61E-06	9.96E-08	3.85E-07	2.15E-06	2.58E-05	**9.21E-01**	5.22E-05	1.14E-04	5.55E-05
P^s_{20}	8.93E-07	3.21E-07	3.05E-07	7.39E-07	4.20E-06	8.07E-06	**9.21E-01**	5.22E-05	1.07E-04
P^s_{21}	1.63E-07	1.64E-07	6.13E-08	4.53E-08	5.20E-07	2.14E-06	8.07E-06	**9.21E-01**	1.01E-04
P^s_{22}	3.73E-08	9.21E-08	9.97E-08	7.33E-08	1.80E-06	5.20E-07	4.20E-06	2.58E-05	**9.21E-01**

Table 4.5: The magnitude of T-matrix elements of a spherical thin-shell transducer computed in COMSOL

of the scattered wave. Therefore, the diagonal values of T-matrix should be non-zero for a spherical thin-shell transducer, while the off-diagonal values should vanish [12, 14].

To investigate the off-diagonal elements accurately, the magnitude of the off-diagonal elements in the T-matrix were normalized by the magnitude of diagonal elements in the same column and the result is shown in Table 4.6. The magnitude of the diagonal elements are significantly greater than non-diagonal elements as expected. The largest “leakage” is 1.10E-04 and occurs with quadrupole-quadrupole spherical harmonic component interactions. It is remarkable that the leakages are so small and demonstrate the quality of the T-matrix calculations.

Normalized T-matrix

	P^i_{00}	P^i_{1-1}	P^i_{10}	P^i_{11}	P^i_{2-2}	P^i_{2-1}	P^i_{20}	P^i_{21}	P^i_{22}
P^s_{00}	1	3.50E-07	1.58E-07	9.92E-07	8.15E-08	4.90E-07	2.10E-06	7.59E-06	3.05E-06
P^s_{1-1}	4.67E-07	1	4.47E-07	7.03E-07	9.48E-08	4.34E-08	9.18E-07	2.62E-06	4.32E-06
P^s_{10}	6.26E-08	1.85E-07	1	4.46E-07	1.23E-07	8.85E-08	3.74E-07	5.51E-07	2.68E-06
P^s_{11}	1.43E-07	2.82E-08	1.84E-07	1	1.12E-07	2.00E-07	3.97E-07	1.01E-07	1.52E-06
P^s_{2-2}	1.01E-05	1.60E-05	2.93E-05	4.72E-05	1	1.10E-04	1.17E-04	6.02E-05	9.96E-04
P^s_{2-1}	3.78E-05	1.34E-06	5.18E-06	2.90E-05	2.80E-05	1	5.66E-05	1.24E-04	6.02E-05
P^s_{20}	1.29E-05	4.33E-06	4.11E-06	9.95E-06	4.56E-06	8.76E-06	1	5.66E-05	1.17E-04
P^s_{21}	2.36E-06	2.21E-06	8.25E-07	6.10E-07	5.64E-07	2.33E-06	8.76E-06	1	1.10E-04
P^s_{22}	5.40E-07	1.24E-06	1.34E-06	9.87E-07	1.96E-06	5.64E-07	4.56E-06	2.80E-05	1

Table 4.6: The magnitude of the non-diagonal elements in the T-matrix were normalized to the magnitude of diagonal elements in the same column

The diagonal elements of the T-matrix are shown in Table 4.7. For the spherical thin-shells, the off-diagonal elements of the T-matrix computed with COMSOL were fairly close to zero.

ELEMENT	**REAL PART**	**IMAG PART**	**MAGNITUDE**	**PHASE(DEG)**
T_{11}	-4.778E-03	-6.895E-02	6.911E-02	-9.40E+01
T_{22}	-5.514E-03	7.405E-02	7.426E-02	9.43E+01
T_{33}	-5.514E-03	7.405E-02	7.426E-02	9.43E+01
T_{44}	-5.514E-03	7.405E-02	7.426E-02	9.43E+01
T_{55}	-8.462E-01	-3.642E-01	9.212E-01	-1.57E+02
T_{66}	-8.462E-01	-3.641E-01	9.212E-01	-1.57E+02
T_{77}	-8.462E-01	-3.641E-01	9.212E-01	-1.57E+02
T_{88}	-8.462E-01	-3.641E-01	9.212E-01	-1.57E+02
T_{99}	-8.462E-01	-3.642E-01	9.212E-01	-1.57E+02

Table 4.7: Diagonal T-matrix elements for a spherical thin-shell transducer

Therefore, the off-diagonal elements were neglected in array calculations and the T-matrix for the spherical thin-shell transducer is expressed as

$$\mathbf{T}_{\mathbf{Sphere}} = \begin{bmatrix} -0.005-0.069\mathrm{i} & 0 & 0 & 0 & 0 & 0 & 0 & 0 & 0 \\ 0 & -0.006+0.074\mathrm{i} & 0 & 0 & 0 & 0 & 0 & 0 & 0 \\ 0 & 0 & -0.006+0.074\mathrm{i} & 0 & 0 & 0 & 0 & 0 & 0 \\ 0 & 0 & 0 & -0.006+0.074\mathrm{i} & 0 & 0 & 0 & 0 & 0 \\ 0 & 0 & 0 & 0 & -0.846-0.364\mathrm{i} & 0 & 0 & 0 & 0 \\ 0 & 0 & 0 & 0 & 0 & -0.846-0.364\mathrm{i} & 0 & 0 & 0 \\ 0 & 0 & 0 & 0 & 0 & 0 & -0.846-0.364\mathrm{i} & 0 & 0 \\ 0 & 0 & 0 & 0 & 0 & 0 & 0 & -0.846-0.364\mathrm{i} & 0 \\ 0 & 0 & 0 & 0 & 0 & 0 & 0 & 0 & -0.846-0.364\mathrm{i} \end{bmatrix}.$$

4.3 The Flextensional Ring-Shell Transducer

The second major objective of this thesis is to model the performance of a linear array of flextensional ring-shell transducer elements. As no analytical solution is available, an accurate 3D model must be constructed to calculate the T-matrix elements of the class V flextensional ring-shell transducer in COMSOL. The excellent result obtained for the thin shell FEM calculations lent confidence that high accuracy results could be obtained for the ring shell transducer as well. Results obtained with COMSOL were compared to prior work as well as to the manufacturer's data in order to investigate the accuracy of the model [7, 15].

Previous research is provided in the thesis work of Rogerio Pinto [7]. It should be noticed that an ultimate goal of this research is to model the performance of the "double-billboard" array of flextensional transducers that was built and tested circa 1990 [1].

4.3.1 Geometry

The dimensional information of the flextensional ring-shell transducer differs slightly from that of prior research. The dimensional nodes from the previous attempt to model the 3D flextensional ring-shell in ATILA FEM were used as a reference for the present geometry. The coordinate values of the nodes were imported to Microsoft Excel and the required dimensions of the geometry were then computed.

The elements were built using 3D geometric primitives in COMSOL (e.g., sphere, circle, etc.) in order to simplify the geometry. The ring-shell transducer was located inside of a fluid spherical domain with radiating boundaries at a total radius of 2.5 m.

The dimensions of the geometry are shown in Table 4.8.

Parameter	Value [cm]
Shell outer radius	67.32
Shell height from symmetry center	14.3
Shell thickness	1.04
Piezoelectric ring edge	8.0
Inner radius of piezoelectric ring	31.9
Outter radius of piezoelectric ring	39.9
Fiber wrap height	8.0
Fiber wrap width	0.5
Radius of water domain	250

Table 4.8: The ring-shell transducer dimensional parameters

4.3.2 Material

Piezoelectric ceramic ring

The piezoelectric ceramic ring has 144 tangentially-poled lead zirconate titanate ceramic plates, separated by 72 steel wedges. The modeling for each tangentially-poled ceramic plate requires coordinate system orientation (Figure 3.2) and this process increases the computation time. Therefore, "smeared" material properties were used for the composite piezoelectric ceramic ring and steel wedges in simplifying the model. Also, the polarization direction altered from the tangential direction into the axial direction.

The properties of the smeared piezo-ring, shown in Figure 4.7 were obtained by McMahon and Armstrong through in-air measurements of the segmented ring during various stages of assembly [7]. The effect of compression due to fiberglass wrapping and material losses were included in the piezoelectric material properties.

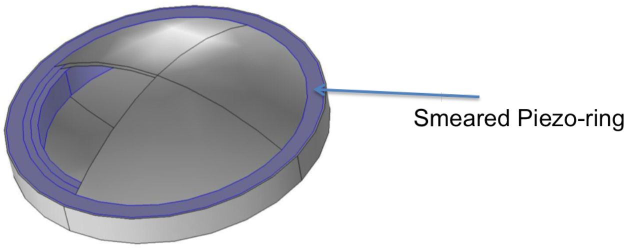

Figure 4.7: Smeared piezo-ring

A further transformation is required of the elasto-piezoelectric material property matrix in order to model a circumferentially-polarized ring as an axially-polarized ring. The required steps are explained in Appendix A. After transformation, the elasto-piezoelectric matrix becomes

$$\begin{bmatrix} S_1 \\ S_2 \\ S_3 \\ S_4 \\ S_5 \\ S_6 \\ D_1 \\ D_2 \\ D_3 \end{bmatrix} = \begin{bmatrix} s_{11}^E & s_{13}^E & s_{12}^E & 0 & 0 & 0 & 0 & 0 & d_{31} \\ s_{13}^E & s_{33}^E & s_{13}^E & 0 & 0 & 0 & 0 & 0 & d_{33} \\ s_{12}^E & s_{13}^E & s_{11}^E & 0 & 0 & 0 & 0 & 0 & d_{31} \\ 0 & 0 & 0 & s_{44}^E & 0 & 0 & d_{15} & 0 & 0 \\ 0 & 0 & 0 & 0 & s_{66}^E & 0 & 0 & 0 & 0 \\ 0 & 0 & 0 & 0 & 0 & s_{44}^E & 0 & d_{15} & 0 \\ 0 & 0 & 0 & d_{15} & 0 & 0 & \varepsilon_{11}^T & 0 & 0 \\ 0 & 0 & 0 & 0 & 0 & d_{15} & 0 & \varepsilon_{11}^T & 0 \\ d_{31} & d_{33} & d_{31} & 0 & 0 & 0 & 0 & 0 & \varepsilon_{33}^T \end{bmatrix} \begin{bmatrix} T_1 \\ T_2 \\ T_3 \\ T_4 \\ T_5 \\ T_6 \\ E_1 \\ E_2 \\ E_3 \end{bmatrix} \tag{4.8}$$

for which the smeared material properties are:

Parameter	**Value**	**Unit**	**Notation**
Density	7550	kg/m^3	ρ
Compliance Matrix			
s_{11}^E	8.202-0.32808i	10^{-12}m^2/N	
s_{12}^E	-2.703+0.10812i	10^{-12}m^2/N	
s_{13}^E	-3.538+0.14152i	10^{-12}m^2/N	
s_{33}^E	11.99-0.4796i	10^{-12}m^2/N	
s_{44}^E	26-1.04i	10^{-12}m^2/N	
s_{66}^E	21.8-8.72i	10^{-12}m^2/N	
Coupling Matrix			
d_{31}	-1	10^{-10}C/N	
d_{33}	2.139	10^{-10}C/N	
d_{15}	-2.811	10^{-10}C/N	
Relative Permittivity			
$\varepsilon_{11}^T/\varepsilon_0$	1297-5.186i		
$\varepsilon_{33}^T/\varepsilon_0$	1297-5.186i		
ε_0	8.85	10^{-12}F/M	

Table 4.9: The flextensional transducer smeared piezoelectric material properties

To select an axial polarization direction the user-defined base vector system was added in the definition branch of the model and the cylindrical coordinate system was defined using the unit basis vectors (**i, j, k**) [21]

$$\begin{aligned}
\mathbf{x_1} &= \hat{\mathbf{e}}_r = \cos\phi\,\mathbf{i} + \sin\phi\,\mathbf{j} \\
\mathbf{x_2} &= \hat{\mathbf{e}}_\phi = -\sin\phi\,\mathbf{i} + \cos\phi\,\mathbf{j} \\
\mathbf{x_3} &= \hat{\mathbf{e}}_z = \mathbf{k}\ .
\end{aligned} \tag{4.9}$$

It should be noted that this modification of polarization requires adjustment of the computed pressure values. The required correction was described in the masters thesis of Rogerio Pinto as the following step [7]

“divide the displacement and pressure fields by the ratio of the circumferential length of a ‘smeared’ piezoelectric element (which is equal to 1/144 of the the ring circumferential length) to its height. In the present case this ratio is 0.1958.”

The correction factor calculated using this ratio as -14.16 dB, i.e. a value of 14.6 dB was added to the computed pressures, for a given voltage drive. Note this correction is only required for computing the radiated pressure field; it does not apply for the short-circuit scattering calculations required to compute the T-matrix values.

Shell

The shell, shown in Figure 4.8 was made of a special alloy steel (ST4340) and modeled by the user defined material properties given in Table 4.10, and taken from an input data file of ATILA FEM [7].

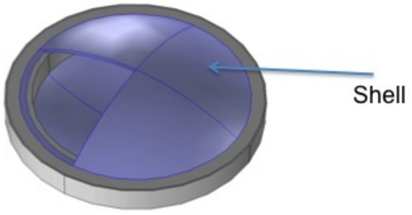

Figure 4.8: ST4340 shell

Fiberglass

The fiberglass sheath, shown in Figure 4.9, provides compression to the ring, having been applied under tension and bonded with epoxy resin, and the smeared piezoelectric ceramic proper-

Parameter	**Value**	**Notation**
Density	7700 kg/m^3	ρ
Young's Modulus	195 GPa	Y
Poisson's ratio	0.28	ν

Table 4.10: Shell material properties

ties include the effect of the fiberglass wrapping compression. For that reason, fiberglass wrapping is added without any specified compression to the model; Only its linear elasto-dynamic properties are specified, as shown in Table 4.11.

Parameter	**Value**	**Notation**
Density	2000 kg/m^3	ρ
Young's Modulus	10 GPa	Y
Poisson's ratio	0.28	ν

Table 4.11: Fiberglass material properties

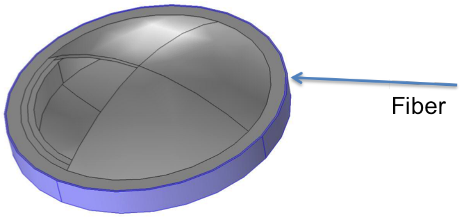

Figure 4.9: Fiberglass wrapping

Fluid Domain

The fluid domain has the same material properties as given in Table 4.2. The fluid media include exterior water and interior air.

4.3.3 Meshing

The maximum element size is defined with respect to the Nyquist criteria which states that the maximum element size must be smaller than $\lambda/5$ (This criteria was applied with respect to the speed of sound in water). The frequency used is 605 Hz which is close to the operating frequency and also provides "*ka*=1".

The upper surface of the piezo-ring was meshed with free triangular mesh elements using the size adjustment of "extra fine." The meshed surface was swept by a built-in feature of COMSOL through the axial direction to the bottom surface of the piezo-ring.

(a) (b)

Figure 4.10: (a) Converted faces with quadrilateral mesh (b) Swept mesh with free triangular elements

The number of the elements swept in were adjusted to be 10 equal hexahedron elements using the "distribution" node feature of COMSOL (Figure 4.10b). The surface boundary between ring faces and the surrounding fluid was converted to a quadrilateral mesh to generate an adjacent-free tetrahedral mesh for the surrounding domain (Figure 4.10a).

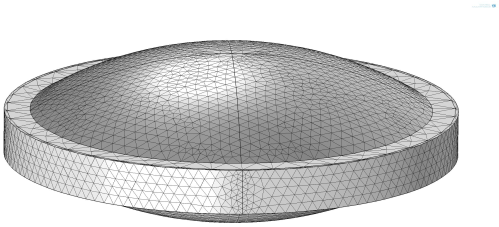

Figure 4.11: Complete mesh of the ring-shell transducer

The remaining geometry was meshed using free triangular mesh elements with a size adjustment of “finer” (Figure 4.11). The complete mesh, shown in Figure 4.12 consists of 207,003 elements and the average element quality of the entire geometry is 0.66.

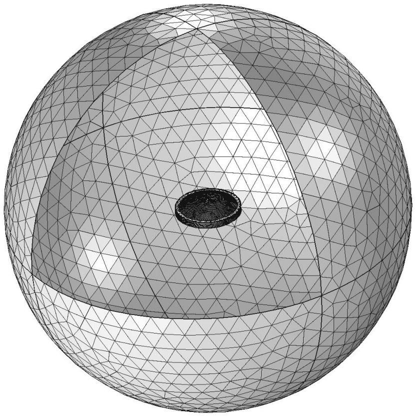

Figure 4.12: Complete mesh of entire geometry

Geometry Entity Level	Element Type	Amount	Avg. Element Quality
All Domain	Tetrahedral	200,483	0.67
	Pyramid	2,680	0.20
	Prism	3,840	0.48
Boundaries			
Radiation	Triangular	5,056	0.99
Piezo ceramic ring	Triangular	3,496	0.54
Wet surface of transducer	Triangular	7,588	0.91
Entire Geometry		**207,003**	**0.66**

Table 4.12: Meshing properties of the 3D spherical transducer model with extra fine mesh for the piezo-ring and with a size adjustment of finer for the remaining geometry

4.3.4 Validation of Model

To quantify validation of the model, the source level (SL) at 3000 Vrms at 1 m was computed in COMSOL, and the correction factor, -14.16 dB, was added to the computed SL (See Chapter 4.3.2 for details).

Figure 4.13 shows the SL as a function of the frequency computed by COMSOL using the baseline properties at 10 Hz intervals, from 200 Hz to 2000 Hz and Figure 4.14 shows a comparison of the SL computed in ATILA FEM [7] against the manufacturer's data of the SL as a function of frequency. The number of DOFs solved was 495,594 and the solution time for each frequency was 255 s.

The first peak value of 211.6 dB re 1 μPa/V at 1 m occurred at 605 Hz with 3000 Vrms driven voltage. While this value differs by 1.4 dB in SL from the manufacturer's data (213 dB), it is much better than ATILA FEM results which differed by 4 dB from the measured value at the resonance frequency.

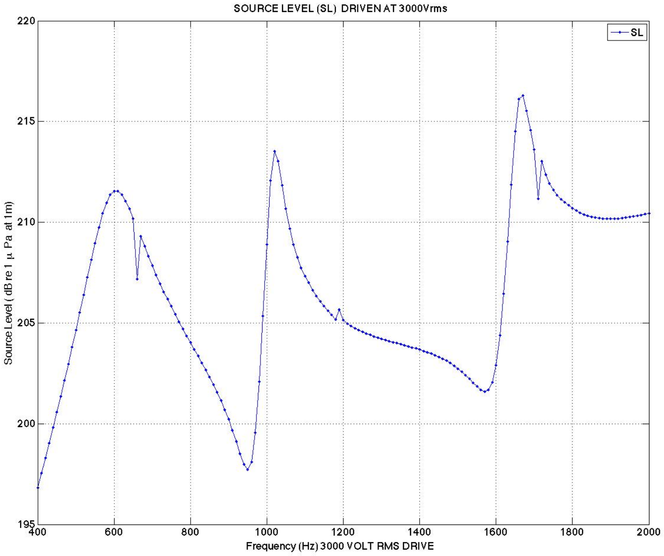

Figure 4.13: SL at 1m on acoustic axis driven 3000 Vrms, obtained with COMSOL ACPZ interface (main model).

The very narrowband irregularities observed in Figure 4.13 (660 Hz, ∼1200 Hz, ∼ 1700 Hz) were found to be uncontrolled shell modes. They are not seen in experimental measurements.

Figure 4.15 depicts the bandwidth at resonance frequency, and it shows the interpolated value of $\pm 3dB$ with respect to computed values. The spurious value at 660 Hz was omitted as being misleading. The mechanical quality factor, Q_m, was calculated 4.35 and a bandwidth of 139 Hz. The Q_m differ 0.4 and the bandwidth 16 Hz from the manufacturer's measured value.

The model shows (Figure 4.13) the second resonance of the developed model occurring at 950

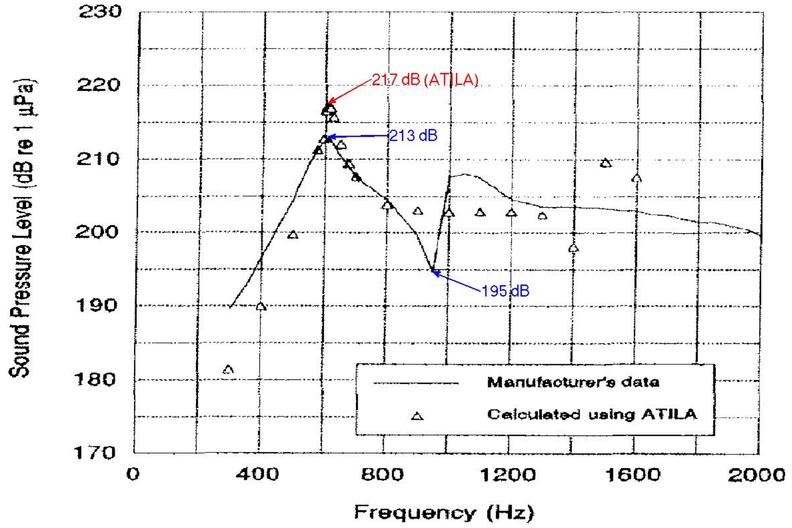

Figure 4.14: SL on acoustic axis driven 3000 Vrms, obtained from the master thesis of Pinto,1993 [7]

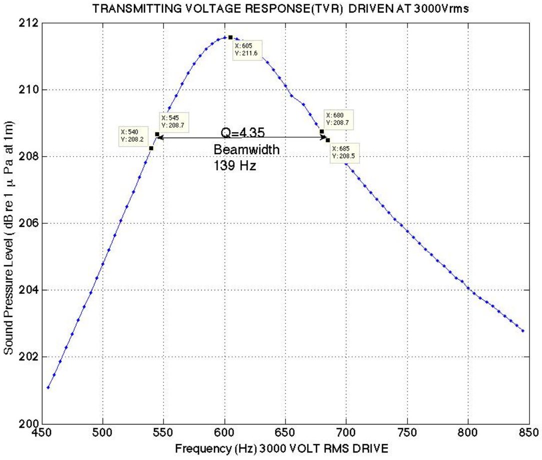

Figure 4.15: The bandwidth at primary resonance frequency(main model)

Hz which is in excellent agreement with manufacturer's data, but the model displays an approximately 6 dB higher peak after the secondary resonance frequency. As the frequency increases to 1000 Hz, the model shows some discrepancies. After 1600 Hz the model shows a lack of convergence to manufacturer's data.

At first glance, the expected reason for this deviation may be due to internal material losses. The internal material losses were not included in the model and could vary the computed SL values. Secondly, the mesh quality (Figure 4.16) may affect the results at higher frequencies since meshing quality is related to operating wavelength. The proper meshing size at low frequency becomes too coarse at high frequency. Therefore, increasing the frequency, reduces the mesh quality of the model. It should be noted, that the mesh size of the developed model was adjusted according to "*f*=474 Hz" and the selected mesh size was not refined enough for high frequency.

Further investigation of meshing quality indicated another issue: the meshing of thin structures deteriorated. Coupling of a thin structure with a larger object obstructs the growth rate of the mesh size. A sample of this situation occurs with the coupling between fiberglass wrapping and the piezo-ring domain. The quality distribution of the mesh is shown in Figure 4.16.

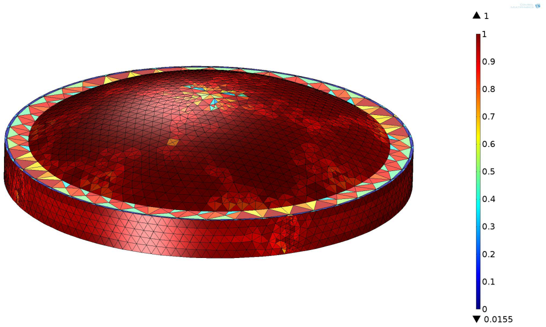

Figure 4.16: Mesh quality plot of the main model for the ring-shell transducer.

Although, the model shows some deviation above the secondary resonance frequency, the model still demonstrates quite good agreement with the manufacturer's data between 400-1000 Hz ("*ka*=1") and better agreement than the previous model (Pinto,1993).

The developed model is sufficient for the purpose of a T-matrix calculation because the performance of the class V flextensional transducer will reside in vicinity of "*ka*=1", and so was used as the base model for the T-matrix calculation.

4.3.5 T-Matrix Calculation

The spherical harmonic components of an incident standing wave were applied at the fluid/solid surface of the transducer, and the spherical harmonic scattered amplitudes were determined from the resultant scattered pressure field in the fluid.

Post processing properties were used to create a spherical parametrized surface within the water domain at radii of 0.5 m. Figure 4.17 shows the defined spherical parametrized surface in water domain.

The magnitude of the T-matrix elements are provided in Table 4.13.

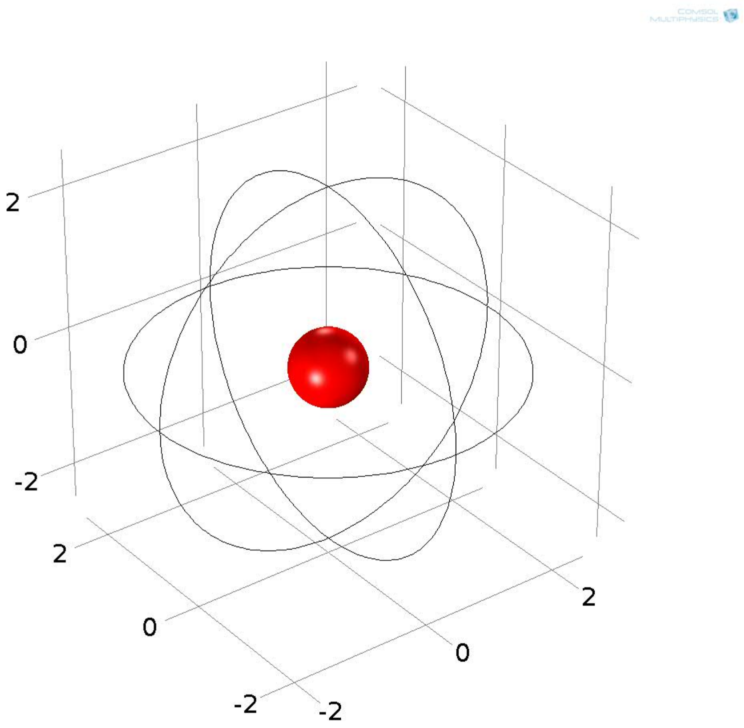

Figure 4.17: A parametrized spherical surface was created at radii of 0.5 m (shown in red; The great circles are on the radiation boundary at 2.5 m).

T-matrix Elements

	P^i_{00}	P^i_{1-1}	P^i_{10}	P^i_{11}	P^i_{2-2}	P^i_{2-1}	P^i_{20}	P^i_{21}	P^i_{22}
P^s_{00}	9.30E-01	2.76E-05	1.64E-04	7.68E-05	4.93E-08	2.63E-06	1.93E-02	1.64E-05	2.25E-05
P^s_{1-1}	7.54E-05	5.06E-02	1.63E-05	6.84E-05	4.62E-07	3.03E-06	1.17E-06	3.73E-06	3.93E-06
P^s_{10}	5.07E-04	1.74E-05	5.68E-02	6.19E-05	2.79E-07	1.38E-06	1.23E-05	1.24E-05	7.02E-06
P^s_{11}	8.49E-05	1.34E-06	1.71E-05	7.55E-02	9.25E-08	1.87E-07	2.16E-06	6.73E-06	1.86E-06
P^s_{2-2}	1.33E-04	2.67E-06	1.11E-05	5.63E-05	4.90E-03	1.75E-07	3.37E-06	5.95E-06	6.81E-05
P^s_{2-1}	1.58E-05	1.22E-05	2.21E-05	7.87E-06	2.21E-07	4.45E-03	1.77E-06	1.56E-06	6.53E-06
P^s_{20}	9.57E-02	3.36E-06	2.03E-05	9.41E-06	7.42E-09	3.12E-07	4.23E-03	1.74E-06	2.70E-06
P^s_{21}	6.35E-06	3.42E-07	2.29E-06	8.47E-06	3.68E-08	8.86E-08	1.21E-07	4.45E-03	8.64E-08
P^s_{22}	2.00E-06	1.32E-07	3.86E-07	1.46E-06	5.84E-08	3.78E-08	4.40E-08	2.00E-07	4.90E-03

Table 4.13: The magnitude of T-matrix elements of a class V flextensional ring-shell transducer computed in COMSOL

For convenience of analysis, the magnitude of the non-diagonal elements in the T-matrix were normalized to the magnitude of diagonal elements in the same column and the results are shown in Table 4.14.

Normalized T-matrix

	P^i_{00}	P^i_{1-1}	P^i_{10}	P^i_{11}	P^i_{2-2}	P^i_{2-1}	P^i_{20}	P^i_{21}	P^i_{22}
P^s_{00}	1	5.46E-04	2.88E-03	1.02E-03	1.01E-05	5.91E-04	1	3.68E-03	4.59E-03
P^s_{1-1}	8.11E-05	1	2.87E-04	9.06E-04	9.42E-05	6.81E-04	6.06E-05	8.39E-04	8.01E-04
P^s_{10}	5.45E-04	3.44E-04	1	8.20E-04	5.68E-05	3.09E-04	6.38E-04	2.78E-03	1.43E-03
P^s_{11}	9.13E-05	2.65E-05	3.02E-04	1	1.89E-05	4.20E-05	1.12E-04	1.51E-03	3.80E-04
P^s_{2-2}	1.43E-04	5.28E-05	1.96E-04	7.46E-04	1	3.93E-05	1.74E-04	1.34E-03	1.39E-02
P^s_{2-1}	1.70E-05	2.42E-04	3.89E-04	1.04E-04	4.51E-05	1	9.17E-05	3.50E-04	1.33E-03
P^s_{20}	1.03E-01	6.64E-05	3.58E-04	1.25E-04	1.51E-06	7.02E-05	2.19E-01	3.91E-04	5.50E-04
P^s_{21}	6.83E-06	6.76E-06	4.03E-05	1.12E-04	7.50E-06	1.99E-05	6.29E-06	1	1.76E-05
P^s_{22}	2.16E-06	2.60E-06	6.79E-06	1.94E-05	1.19E-05	8.50E-06	2.28E-06	4.48E-05	1

Table 4.14: The magnitude of non-diagonal elements in the T-matrix normalized to the magnitude of diagonal element in the same column

In the vicinity of the primary resonance frequency, 605 Hz, the flextensional transducer radiates both quadrupole and monopole pressure fields. It is found that the linear quadrupole radiated pressure coefficient is about 1/10 of the monopole coefficient (see section 5.2 for details) When a monopole field is incident, the ring-shell generates a quadrupole field and vice versa, characteristic of the resonant vibration. This general dynamic response of the transducer can be seen from the T-matrix table. It is remarkable that the magnitude of T_{77} (quadrupole-quadrupole) is smaller than the magnitude of T_{17} (quadrupole-monopole) which are highlighted in Table 4.14. Thus, the calculated T-matrix captures the interaction between monopole and quadrupole excitation.

The T-matrix for the ring-shell transducer is not diagonal while the T-matrix of the spherical thin-shell transducer essentially is. This is expected behavior as the geometry of the flextensional transducer is not spherical. It should be noted, that the T-matrix is a kind of transfer function. The diagonal elements are represented in Table 4.15.

Similar to the spherical thin-shell transducer, the T-matrix of the flextensional ring-shell transducer is nearly a diagonal matrix except for elements of monopole-linear quadrupole interactions (T_{17},T_{71}). Unlike the spherical thin-shell transducers, the monopole-linear quadrupole term must be included in the T-matrix. Neglecting small values in the matrix, the T-matrix of the flextensional ring-shell becomes,

ELEMENT	REAL PART	IMAG PART	MAGNITUDE	PHASE(DEG)
T_{11}	-9.237E-01	-1.088E-01	9.301E-01	-1.73E+02
T_{22}	-1.538E-02	-4.820E-02	5.060E-02	-1.08E+02
T_{33}	-1.652E-02	-5.435E-02	5.680E-02	-1.07E+02
T_{44}	-2.467E-02	-7.134E-02	7.548E-02	-1.09E+02
T_{55}	-1.674E-03	-4.607E-03	4.902E-03	-1.10E+02
T_{66}	-1.660E-03	-4.129E-03	4.450E-03	-1.12E+02
T_{77}	-3.586E-03	-2.242E-03	4.229E-03	-1.48E+02
T_{88}	-1.660E-03	-4.129E-03	4.450E-03	-1.12E+02
T_{99}	-1.674E-03	-4.607E-03	4.902E-03	-1.10E+02

Table 4.15: Diagonal T-matrix elements for a class V flextensional ring-shell transducer

$$\mathbf{T}_{\mathbf{Ring-shell}} = \begin{bmatrix} -0.924-0.109\mathrm{i} & 0 & 0 & 0 & 0 & 0 & -0.019-0.002\mathrm{i} & 0 & 0 \\ 0 & -0.015-0.048\mathrm{i} & 0 & 0 & 0 & 0 & 0 & 0 & 0 \\ 0 & 0 & -0.017-0.054\mathrm{i} & 0 & 0 & 0 & 0 & 0 & 0 \\ 0 & 0 & 0 & -0.025-0.071\mathrm{i} & 0 & 0 & 0 & 0 & 0 \\ 0 & 0 & 0 & 0 & -0.002-0.005\mathrm{i} & 0 & 0 & 0 & 0 \\ 0 & 0 & 0 & 0 & 0 & -0.002-0.004\mathrm{i} & 0 & 0 & 0 \\ -0.095-0.009\mathrm{i} & 0 & 0 & 0 & 0 & 0 & -0.004-0.002\mathrm{i} & 0 & 0 \\ 0 & 0 & 0 & 0 & 0 & 0 & 0 & -0.002-0.004\mathrm{i} & 0 \\ 0 & 0 & 0 & 0 & 0 & 0 & 0 & 0 & -0.002-0.005\mathrm{i} \end{bmatrix}.$$

4.4 Improvement on the Ring-Shell Transducer Model at Higher Operating Frequencies

Although the accuracy of the developed model was verified up to 1000 Hz, corresponding to the frequency of interest in this thesis to calculate the T-matrix elements, the SL of the developed model demonstrated some deviation from experimental values at higher frequencies (Figure 4.13). To achieve more accurate results at higher frequencies, improvements were made to the first developed model. The first model developed is referred to as the “main model” throughout this section.

4.4.1 Refined Mesh Model

For frequencies up to 2 kHz, the wavelength of sound in water is 0.745 m (c=1490 m/s). The maximum meshing element size should be specified with respect to $\lambda/5$ at this frequency. In this limit, the maximum element size of meshed geometry equals 0.149 m which is much smaller than the maximum mesh element size of the main model (0.275 m). To obtain an accurate result at higher frequency, the mesh of the geometry was refined and adjusted satisfy the

$\lambda/5$ criteria at 2000 Hz. The refined mesh consist of 413,778 elements and 733,161 DOFs.

The SL of the refined mesh model is shown in Figure 4.18 and the SL was calculated at 10 Hz intervals, from 200 Hz to 2000 Hz. Primary and secondary resonances were captured at the same frequency as those in the main model, as are the amplitudes. Mesh refinement did not produce any significant improvement. Thus, the general behavior of SL stayed the same and the refined mesh could not remove discrepancies between the graph of computed SL values and the graph of measured SL values (Figure 4.14). It should also be noted that the computation time increased due to the increased number of DOFs of the refined mesh.

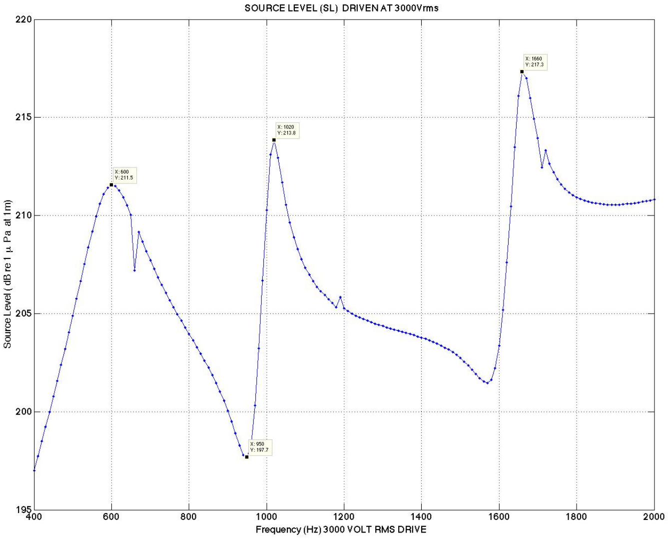

Figure 4.18: SL at 1 m on acoustic axis is driven at 3000 Vrms of the refined mesh model, the mesh size is adjusted with respect to 2000 Hz.

4.4.2 Improved Model

Upon further investigation, it was revealed that the mesh quality was reduced in the neighborhood of the fiberglass wrapping and the surface of the shell. The fiberglass wrapping was re-meshed with triangular elements and swept through the axially direction from top to bottom with a limited maximum mesh element size to $\lambda/30$ or 0.025 m at 2500 Hz.

In addition to mesh improvement, the spherical wave radiation boundary condition was replaced with a spherical perfectly matched layer (PML) to absorb the incident waves without reflection as they strike the radiation boundary. The PML surrounded the fluid domain and had a 0.5 m thickness, reducing the radius of fluid domain to 2 m. The updated geometry is represented in

Figure 4.19. The PML mesh was swept radially with a distribution of ten hexahedron elements through its thickness, and the water domain between PML and ring-shell was meshed with a boundary layer mesh. The boundary layer mesh is recommended by COMSOL in order to enhance the precision of the far field calculation near the PML [17]. The complete mesh consist of 238,503 elements and 792,888 DOFs.

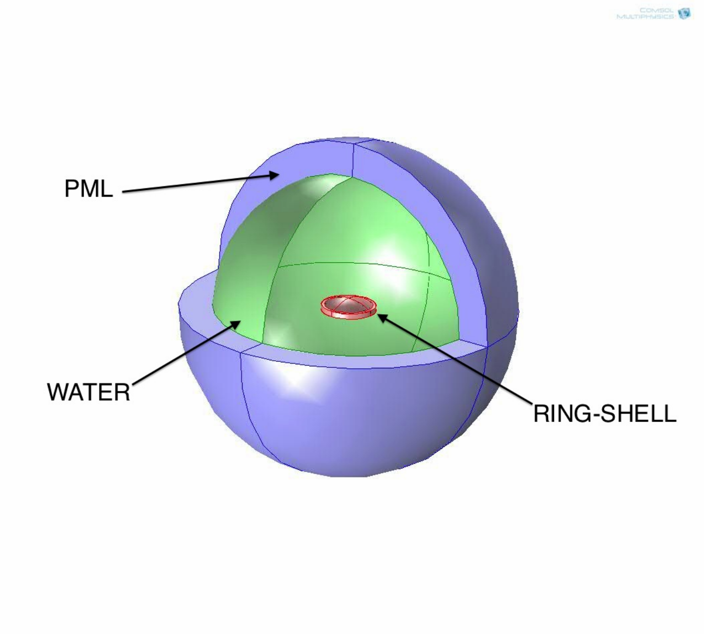

Figure 4.19: The geometry of the improved model, PML surrounded the fluid domain.

Figure 4.20 shows the SL of the improved model where again the SL was calculated at 10 Hz intervals, from 200 Hz to 2000 Hz. The behavior of the model changed. The secondary resonance frequency shifted left by 35 Hz from the manufacturer's data to 985 Hz, and the SL became higher than the manufacturer's data by 6 dB.

The effects of the improvements were seen at frequencies higher than the secondary resonance. Beyond that frequency, the SL agrees with the manufacturer's data (Figure 4.14) and the difference was reduced to 2 dB, showing fairly good agreement with the manufacturer's data up to 1600 Hz. For frequencies higher than 1600 Hz, the SL again deviates slightly from the manufacturer's data.

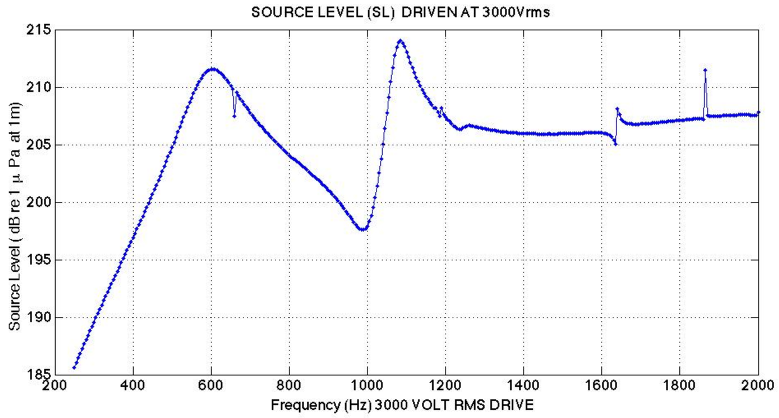

Figure 4.20: SL on acoustic axis driven at 3000 Vrms of the improved model, PML and boundary layer mesh added.

4.4.3 Result

In addition to the main model, two different models were examined for the purpose of improving accuracy at higher frequencies. Figure 4.21 depicts the comparison of SL of the main model, the refined mesh model and the improved model.

The main model and refined mesh models performed identically from 400 Hz to 800 Hz. The improved model produced a lower SL than the other models at higher frequencies, and it converged with the manufacturer's data. Thus, the improved model performed better when compared to the other model, although it captured the secondary resonance with a 35 Hz difference from experiment.

Reasons for the improvement in the SL value are due in part to the changes in the mesh structure and applied PML as boundary condition.

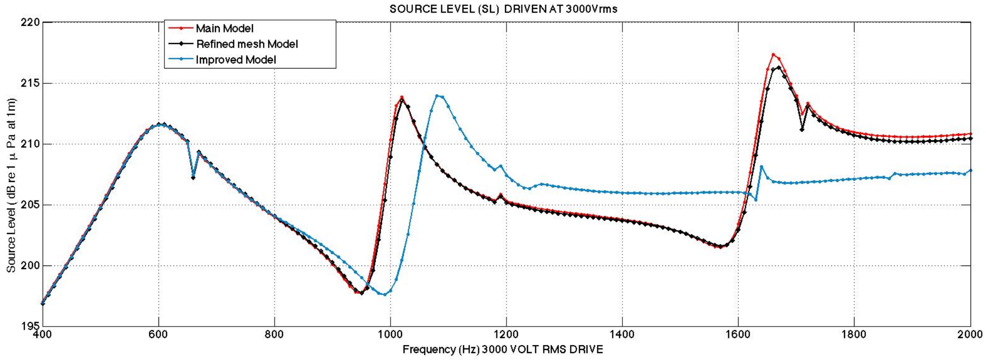

Figure 4.21: The SL comparison of three developed model

The detailed SL of frequency interest in the neighborhood of the first resonance is illustrated in Figures 4.23 through 4.24. The comparison of the bandwidth and the Q values are shown in Table 4.16. The three models performed nearly the same and show fairly good agreement with the manufacturer's data between 250-1000 Hz.

Model	BW (Hz)	BW Error(Hz)	BW(%)	Q	Q Error	Q Error(%)
Main	138.5	16.5	10.64	4.33	0.43	11
Refined	139.5	15.5	10.00	4.30	0.4	10.26
Improved	139	16	10.03	4.35	0.45	10.35

Table 4.16: comparison of bandwidth and mechanical Q value from three model against manufacturer's data

All the models reproduced equally well the SL up to 1000 Hz. For this reason, the main model was preferred for the T-matrix element calculation because of reduced computation time for equivalent accuracy.

Model	number of element	average	worst	DOFs	Computation Time
main	207,003	0.66	2.29E-05	495594	258 s.
refined	413,778	0.73	4.23E-05	733161	353 s.
improved	238,503	0.56	2.23E-06	792888	550 s.

Table 4.17: The computation time values and the general mesh information of the three model

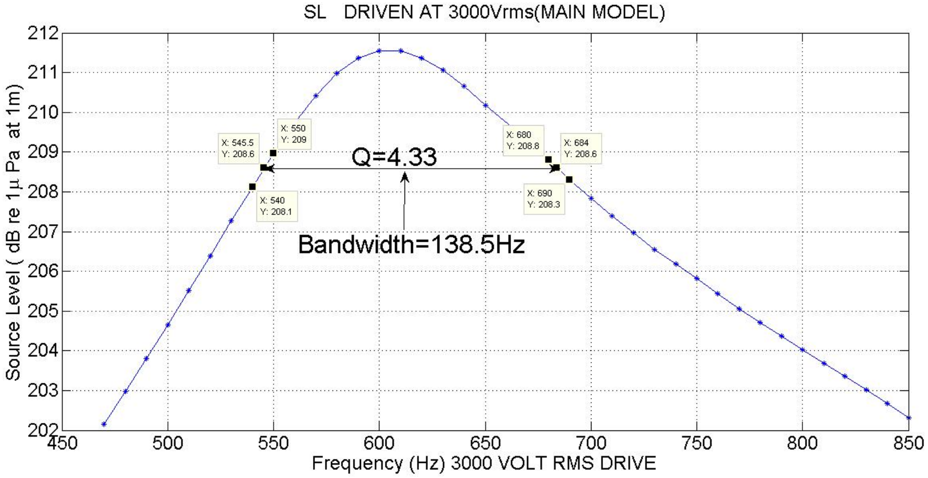

Figure 4.22: The bandwidth at primary resonance frequency (main model)

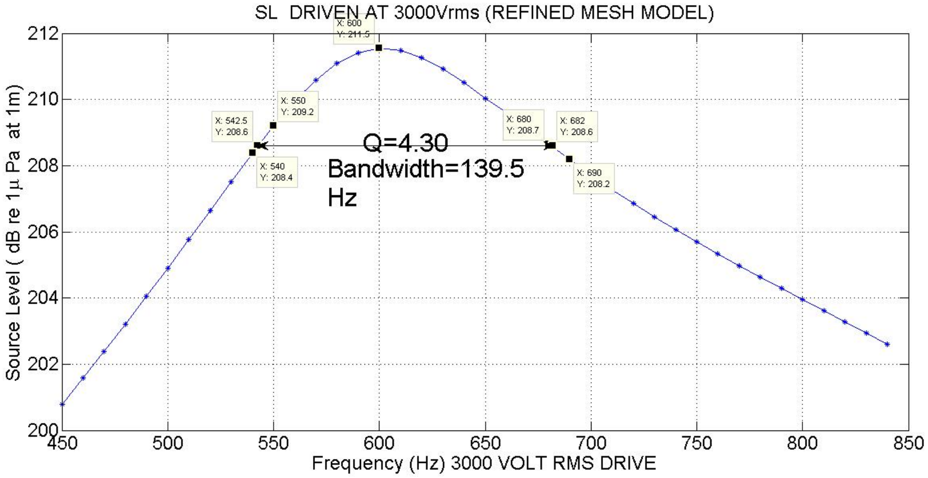

Figure 4.23: The bandwidth at primary resonance frequency (refined model)

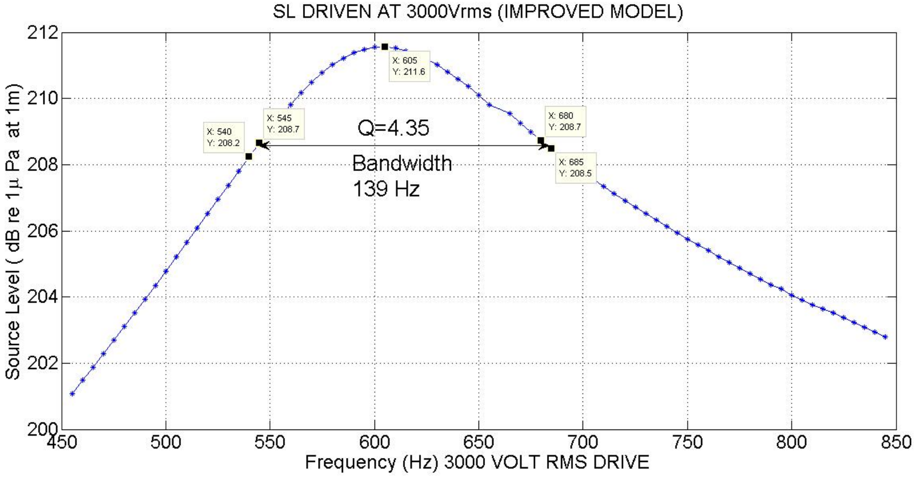

Figure 4.24: The bandwidth at primary resonance frequency (improved model)

THIS PAGE INTENTIONALLY LEFT BLANK

CHAPTER 5:
Linear Array Performance Modeling by Using T-Matrix Method

The vertical linear array with the spherical thin-shell transducer elements and the vertical linear array with the ring-shell transducer elements were programmed in MATLAB, using the T-matrix method. The required T-matrix elements for both types of the transducers were reported in Chapter 4.

5.1 The Development Sequence of an Array Model

1. Computation of the free-field radiated pressure coefficients

2. Calculation of the translation matrix using the addition theorem

3. Implementation of the T-matrix to calculate the scattered pressure coefficients

4. Computation of the total acoustic pressure field and generation of the far-field beam pattern

5.2 Computation of the Free-Field Radiated Pressure Coefficients

The free-field radiated pressure coefficients of both transducer types were calculated at a 1 V peak driven potential. That a driving peak was used versus 1 Vrms is of no consequence as only normalized beam patterns are presented in this chapter. The free-field radiated pressure amplitudes were computed by solving equation (2.40) using COMSOL. The number of spherical harmonic components kept was truncated at the the quadrupolar degree, n=2, so the total number of spherical harmonic components kept was 9 (n=0,1,2 and m=-n..n).

Results for the spherical thin-shell transducer are listed in Table 5.1, and the results for the ring-shell transducer are given in Table 5.2.

operation freq	*474Hz (ka=1)*				
Mode	**Real**	**Imaginary**	**Amplitude**	$\frac{\textbf{Amplitude}}{\mathbf{|P^r_{00}|}}$	**Angle(rad)**
P^r_{00}	1.349E+00	1.946E+01	1.951E+01	1.000E+00	1.502E+00
P^r_{1-1}	6.323E-06	6.863E-06	9.331E-06	4.784E-07	8.263E-01
P^r_{10}	3.608E-07	1.330E-06	1.378E-06	7.067E-08	1.306E+00
P^r_{11}	2.909E-06	-9.429E-07	3.058E-06	1.568E-07	-3.135E-01
P^r_{2-2}	2.633E-04	1.202E-04	2.894E-04	1.484E-05	4.285E-01
P^r_{2-1}	-6.943E-04	3.410E-04	7.735E-04	3.966E-05	2.685E+00
P^r_{20}	2.027E-04	9.465E-05	2.237E-04	1.147E-05	4.369E-01
P^r_{21}	3.074E-05	3.885E-05	4.954E-05	2.540E-06	9.015E-01
P^r_{22}	-1.306E-06	-8.569E-06	8.668E-06	4.444E-07	-1.722E+00

Table 5.1: The radiated pressure coefficients of the spherical thin-shell transducer for monopole, dipole, and quadrupole (*n*=0, 1, 2 and *m*=-*n*..*n*), for 1 V peak drive.

operation freq	*605Hz (ka=1)*				
Mode	**Real**	**Imaginary**	**Amplitude**	$\frac{\textbf{Amplitude}}{\mathbf{|P^r_{00}|}}$	**Angle (rad)**
P^r_{00}	6.431E+00	9.823E-01	6.506E+00	1.000E+00	1.516E-01
P^r_{1-1}	1.026E-04	-6.191E-04	6.275E-04	9.645E-05	-1.407E+00
P^r_{10}	1.109E-03	3.419E-03	3.594E-03	5.524E-04	1.257E+00
P^r_{11}	4.475E-04	-4.552E-04	6.384E-04	9.812E-05	-7.939E-01
P^r_{2-2}	-4.804E-06	1.083E-03	1.083E-03	1.665E-04	1.575E+00
P^r_{2-1}	1.188E-04	1.791E-04	2.149E-04	3.303E-05	9.853E-01
P^r_{20}	6.738E-01	3.858E-02	6.749E-01	1.037E-01	5.719E-02
P^r_{21}	-2.213E-05	2.659E-05	3.459E-05	5.317E-06	2.265E+00
P^r_{22}	8.583E-06	-6.395E-06	1.070E-05	1.645E-06	-6.403E-01

Table 5.2: The radiated pressure coefficients of the ring-shell transducer for monopole, dipole, and quadrupole (*n*=0, 1, 2 and *m*=-*n*..*n*), for 1 V peak drive.

Table 5.1 indicates that the free-field radiated pressure amplitudes of the spherical thin-shell transducer are negligible except for the monopole (P^r_{00}), as expected. Because of symmetry, coefficients other than P^r_{00} are close to zero, indicating the accuracy of the finite element model.

Similarly, Table 5.2 shows that the free-field radiated pressure amplitudes of the ring-shell transducer are negligible except for the monopole (P^r_{00}) and linear quadrupole (P^r_{20}), the monopole coefficient being about “10” times the linear quadrupole coefficient. This is expected due to the nature of the flexural motion of the ring-shell transducer.

Negligible values of the free-field radiation are ignored in far-field calculation. The free-field radiated pressure vectors then become for a 1 V peak drive,

$$P^{R}_{Sphere} = \begin{bmatrix} 1.345 + 19.459\mathrm{i} \\ 0 \\ 0 \\ 0 \\ 0 \\ 0 \\ 0 \\ 0 \\ 0 \end{bmatrix} \tag{5.1}$$

$$P^{R}_{Ring-shell} = \begin{bmatrix} 6.431 + 0.982i \\ 0 \\ 0 \\ 0 \\ 0 \\ 0 \\ 0.674 + 0.039i \\ 0 \\ 0 \end{bmatrix}, \tag{5.2}$$

and they were imported to MATLAB for further calculation.

5.3 Calculation of the Translation Matrix

The translation matrix,"$\mathbf{G_{lq}}$", is needed to relate the "s, u^{th}" outgoing wave component from transducer "q" to the "n, m^{th}" free-field incident component on transducer "l". The translation matrix is obtained from a spherical addition theorem (See Chapter 2.4.5 for details). Bold capital "G" denotes a translation matrix from one transducer to another in the array

$$\mathbf{G_{lq}} = \begin{pmatrix} P^{inc}_{q\to l\neq q,00} \\ P^{inc}_{q\to l\neq q,1-1} \\ P^{inc}_{q\to l\neq q,10} \\ P^{inc}_{q\to l\neq q,11} \\ P^{inc}_{q\to l\neq q,2-2} \\ P^{inc}_{q\to l\neq q,2-1} \\ P^{inc}_{q\to l\neq q,20} \\ P^{inc}_{q\to l\neq q,21} \\ P^{inc}_{q\to l\neq q,22} \end{pmatrix} = \begin{bmatrix}
G_{\substack{l,00\\q,00}} & G_{\substack{l,00\\q,1-1}} & G_{\substack{l,00\\q,10}} & G_{\substack{l,00\\q,11}} & G_{\substack{l,00\\q,2-2}} & G_{\substack{l,00\\q,2-1}} & G_{\substack{l,00\\q,20}} & G_{\substack{l,00\\q,21}} & G_{\substack{l,00\\q,22}} \\
G_{\substack{l,1-1\\q,00}} & G_{\substack{l,1-1\\q,1-1}} & G_{\substack{l,1-1\\q,10}} & G_{\substack{l,1-1\\q,11}} & G_{\substack{l,1-1\\q,2-2}} & G_{\substack{l,1-1\\q,2-1}} & G_{\substack{l,1-1\\q,20}} & G_{\substack{l,1-1\\q,21}} & G_{\substack{l,1-1\\q,22}} \\
G_{\substack{l,10\\q,00}} & G_{\substack{l,10\\q,1-1}} & G_{\substack{l,10\\q,10}} & G_{\substack{l,10\\q,11}} & G_{\substack{l,10\\q,2-2}} & G_{\substack{l,10\\q,2-1}} & G_{\substack{l,10\\q,20}} & G_{\substack{l,10\\q,21}} & G_{\substack{l,10\\q,22}} \\
G_{\substack{l,11\\q,00}} & G_{\substack{l,11\\q,1-1}} & G_{\substack{l,11\\q,10}} & G_{\substack{l,11\\q,11}} & G_{\substack{l,11\\q,2-2}} & G_{\substack{l,11\\q,2-1}} & G_{\substack{l,11\\q,20}} & G_{\substack{l,11\\q,21}} & G_{\substack{l,11\\q,22}} \\
G_{\substack{l,2-2\\q,00}} & G_{\substack{l,2-2\\q,1-1}} & G_{\substack{l,2-2\\q,10}} & G_{\substack{l,2-2\\q,11}} & G_{\substack{l,2-2\\q,2-2}} & G_{\substack{l,2-2\\q,2-1}} & G_{\substack{l,2-2\\q,20}} & G_{\substack{l,2-2\\q,21}} & G_{\substack{l,2-2\\q,22}} \\
G_{\substack{l,2-1\\q,00}} & G_{\substack{l,2-1\\q,1-1}} & G_{\substack{l,2-1\\q,10}} & G_{\substack{l,2-1\\q,11}} & G_{\substack{l,2-1\\q,2-2}} & G_{\substack{l,2-1\\q,2-1}} & G_{\substack{l,2-1\\q,20}} & G_{\substack{l,2-1\\q,21}} & G_{\substack{l,2-1\\q,22}} \\
G_{\substack{l,20\\q,00}} & G_{\substack{l,20\\q,1-1}} & G_{\substack{l,20\\q,10}} & G_{\substack{l,20\\q,11}} & G_{\substack{l,20\\q,2-2}} & G_{\substack{l,20\\q,2-1}} & G_{\substack{l,20\\q,20}} & G_{\substack{l,20\\q,21}} & G_{\substack{l,20\\q,22}} \\
G_{\substack{l,21\\q,00}} & G_{\substack{l,21\\q,1-1}} & G_{\substack{l,21\\q,10}} & G_{\substack{l,21\\q,11}} & G_{\substack{l,21\\q,2-2}} & G_{\substack{l,21\\q,2-1}} & G_{\substack{l,21\\q,20}} & G_{\substack{l,21\\q,21}} & G_{\substack{l,21\\q,22}} \\
G_{\substack{l,22\\q,00}} & G_{\substack{l,22\\q,1-1}} & G_{\substack{l,22\\q,10}} & G_{\substack{l,22\\q,11}} & G_{\substack{l,22\\q,2-2}} & G_{\substack{l,22\\q,2-1}} & G_{\substack{l,22\\q,20}} & G_{\substack{l,22\\q,21}} & G_{\substack{l,22\\q,22}}
\end{bmatrix} \begin{pmatrix} P^{out}_{q,00} \\ P^{out}_{q,1-1} \\ P^{out}_{q,10} \\ P^{out}_{q,11} \\ P^{out}_{q,2-2} \\ P^{out}_{q,2-1} \\ P^{out}_{q,20} \\ P^{out}_{q,21} \\ P^{out}_{q,22} \end{pmatrix} .$$

Equation (2.43) was employed in MATLAB to construct the translation matrix, $\mathbf{G_{lq}}$, $l \neq q$.

The l^{th} row refers to the interaction of the "l^{th}" transducer with the other transducers in the array. Computation time for producing the translation matrix depends on the number of elements within an array

$$\begin{pmatrix} \mathbf{P_1^{inc}} \\ \mathbf{P_2^{inc}} \\ \vdots \\ \mathbf{P_N^{inc}} \end{pmatrix} = \begin{bmatrix} 0 & \mathbf{G_{12}} & \cdots & \mathbf{G_{1N}} \\ \mathbf{G_{21}} & 0 & \cdots & \mathbf{G_{2N}} \\ \vdots & \vdots & \ddots & \vdots \\ \mathbf{G_{N1}} & \mathbf{G_{N2}} & \cdots & 0 \end{bmatrix} \begin{pmatrix} \mathbf{P_1^{out}} \\ \mathbf{P_2^{out}} \\ \vdots \\ \mathbf{P_N^{out}} \end{pmatrix} , \tag{5.3}$$

where

$\mathbf{P}_l^{\mathbf{out}} = \mathbf{P}_l^{\mathbf{R}} + \mathbf{P}_l^{\mathbf{S}}$.

5.4 Implementation of the T-matrix

The scattered pressure amplitudes can be obtained solving (2.49). The product of both sides with the inverse matrix of $(\mathbf{I}-\alpha)$ gives the scattered pressure vectors.

$$\begin{pmatrix} \mathbf{P_1}^{\mathbf{S}} \\ \vdots \\ \mathbf{P_N^S} \end{pmatrix} = (\mathbf{I}-\alpha)^{-1}\alpha \begin{pmatrix} \mathbf{P_1^R} \\ \vdots \\ \mathbf{P_N^R} \end{pmatrix} , \tag{5.4}$$

where α is defined for an array which is composed of the identical elements,

$$\alpha = \begin{pmatrix} 0 & \mathbf{TG_{12}} & \cdots & \mathbf{TG_{1N}} \\ \mathbf{TG_{21}} & 0 & \cdots & \mathbf{TG_{2N}} \\ \vdots & \vdots & \ddots & \vdots \\ \mathbf{TG_{N1}} & \mathbf{TG_{N2}} & \cdots & 0 \end{pmatrix} .$$

Considering a three-element transducer array configuration, for example, the free-field scattered pressure amplitudes become

$$\begin{pmatrix} \mathbf{P_1^S} \\ \mathbf{P_2^S} \\ \mathbf{P_3^S} \end{pmatrix} = \begin{bmatrix} \mathrm{I} & -\mathbf{TG_{12}} & -\mathbf{TG_{13}} \\ -\mathbf{TG_{21}} & \mathrm{I} & -\mathbf{TG_{23}} \\ -\mathbf{TG_{31}} & -\mathbf{TG_{32}} & \mathrm{I} \end{bmatrix}^{-1} \begin{bmatrix} 0 & \mathbf{TG_{12}} & \mathbf{TG_{13}} \\ \mathbf{TG_{21}} & 0 & \mathbf{TG_{23}} \\ \mathbf{TG_{31}} & \mathbf{TG_{32}} & 0 \end{bmatrix} \begin{pmatrix} \mathbf{P_1^R} \\ \mathbf{P_2^R} \\ \mathbf{P_3^R} \end{pmatrix} .$$

In Chapter 4.2.6 the complex coefficients of the T-matrix for the spherical thin-shell transducer were calculated as

$$\mathbf{T_{Sphere}} = \begin{bmatrix} -0.005-0.069\mathrm{i} & 0 & 0 & 0 & 0 & 0 & 0 & 0 & 0 \\ 0 & -0.006+0.074\mathrm{i} & 0 & 0 & 0 & 0 & 0 & 0 & 0 \\ 0 & 0 & -0.006+0.074\mathrm{i} & 0 & 0 & 0 & 0 & 0 & 0 \\ 0 & 0 & 0 & -0.006+0.074\mathrm{i} & 0 & 0 & 0 & 0 & 0 \\ 0 & 0 & 0 & 0 & -0.846-0.364\mathrm{i} & 0 & 0 & 0 & 0 \\ 0 & 0 & 0 & 0 & 0 & -0.846-0.364\mathrm{i} & 0 & 0 & 0 \\ 0 & 0 & 0 & 0 & 0 & 0 & -0.846-0.364\mathrm{i} & 0 & 0 \\ 0 & 0 & 0 & 0 & 0 & 0 & 0 & -0.846-0.364\mathrm{i} & 0 \\ 0 & 0 & 0 & 0 & 0 & 0 & 0 & 0 & -0.846-0.364\mathrm{i} \end{bmatrix} .$$

In Chapter 4.3.5 the complex coefficients of T-matrix for the ring-shell transducer were calculated as

$$\mathbf{T_{Ring-shell}} = \begin{bmatrix} -0.924-0.109\mathrm{i} & 0 & 0 & 0 & 0 & 0 & -0.019-0.002\mathrm{i} & 0 & 0 \\ 0 & -0.015-0.048\mathrm{i} & 0 & 0 & 0 & 0 & 0 & 0 & 0 \\ 0 & 0 & -0.017-0.054\mathrm{i} & 0 & 0 & 0 & 0 & 0 & 0 \\ 0 & 0 & 0 & -0.025-0.071\mathrm{i} & 0 & 0 & 0 & 0 & 0 \\ 0 & 0 & 0 & 0 & -0.002-0.005\mathrm{i} & 0 & 0 & 0 & 0 \\ 0 & 0 & 0 & 0 & 0 & -0.002-0.004\mathrm{i} & 0 & 0 & 0 \\ -0.095-0.009\mathrm{i} & 0 & 0 & 0 & 0 & 0 & -0.004-0.002\mathrm{i} & 0 & 0 \\ 0 & 0 & 0 & 0 & 0 & 0 & 0 & -0.002-0.004\mathrm{i} & 0 \\ 0 & 0 & 0 & 0 & 0 & 0 & 0 & 0 & -0.002-0.005\mathrm{i} \end{bmatrix} .$$

5.5 Computation of the Total Acoustic Pressure Field and Far-Field Beam Pattern

In the array models, a line of $N_{\mathbf{X}}$ transducer sources with the adjacent elements equally spaced were analyzed and are as shown in Figure 5.1. The transducers are aligned with the polar axis (z axis). The beam patterns of the developed models, therefore, have rotational symmetry with respect to the array (polar) axis. Beam patterns are represented by polar coordinates (θ,ϕ), and the far-field approximation was used with phase difference between elements, due to their position. This was taken into account for the calculations of far-field acoustic field and beam pattern.

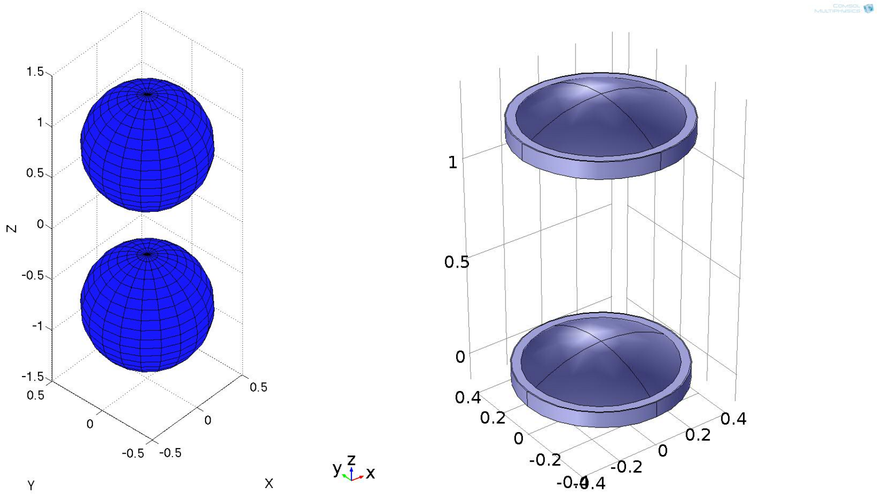

(a) (b)

Figure 5.1: Orientation of the transducers; spacing $\lambda/2$ and "$ka = 1$" (a) Spherical thin-shell transducer (b) Class V ring-shell transducer

The total acoustic pressure in the far-field was obtained from superposition of the radiated and the scattered complex acoustic pressure amplitudes originating from the transducers in the array (See Chapter 2.4.7 for details) . Equations (5.5) and (5.7) were employed in MATLAB to obtain far-field pressure amplitudes.The radiated pressure amplitudes are reported in Section 5.2, and the scattered pressure amplitudes can be obtained from equation (5.4). All equations were combined in MATLAB, and the code used is presented in Appendix B.

The far-field pressure is

$$p_{ff}(r,\theta,\phi) = \frac{e^{-ikr}}{kr} \sum_{l=1}^{N_{\mathbf{X}}} e^{i\vec{k}\cdot\vec{r}_{Ol}} \sum_{n=0}^{n_{\max}} i^{(n+1)} \sum_{m=-n}^{n} \left[P_{lmn}^{S} + P_{lmn}^{R}\right] \Omega_{n}^{m}(\theta,\phi) \; , \tag{5.5}$$

where

$$\vec{k}\cdot\vec{r}_{Ol} = k\left(x_{Ol}\sin\theta\cos\phi + y_{Ol}\sin\theta\sin\phi + z_{Ol}\cos\theta\right) \; . \tag{5.6}$$

and x_{Ol}, y_{Ol}, z_{Ol} are the rectangular coordinates of the origin of transducer "l."

The normalized far-field beam pattern is

$$b = 20\log_{10}\left(\frac{\left|p_{ff}(r,\theta,\phi)\right|}{\left|p_{ff}(r,\theta,\phi)\right|_{\max}}\right) \; . \tag{5.7}$$

To understand the array interaction effect on the far-field beam pattern different linear array configurations were examined. For all configurations, 3D normalized far-field beam patterns were plotted using the T-matrix method. As the horizontal (i.e., perpendicular array axis) beam patterns of all configurations were omni-directional, the detailed investigation of the effect of the T-matrix method on beam pattern was focused on the vertical beam (plane including array axis direction) patterns. The resultant normalized vertical beam patterns were compared against those computed for non-interacting simple sources.

5.6 Figures of the Far Field Beam Patterns

The 2D normalized vertical far-field beam patterns were plotted in dB as a function of the angle (in degrees). The beam patterns obtained with the T-matrix method are compared to point sources on the same plot. For the polar plot, magnitudes lower than "-30 dB" were omitted since values lower than -30 dB are negligible compared to the maximum intensity. The "0 dB" reference value was shifted to 30 dB to improve visualization. Similarly, for improving the visualization of cartesian plots of the beam patterns, magnitudes which were lower than "-50 dB" were omitted and the "0 dB" reference shifted to 50 dB. The angles "90" and "270" correspond to the broadside direction while "0" and "180" correspond to the "array axis (end fire)" direction.

Several configurations were examined, to investigate the performance of the array and to determine array interaction.

5.6.1 The Model of the Linear Array With Spherical Thin-Shell Elements

Three-Element Array Configuration

Figure 5.2 depicts the 3D normalized far-field beam pattern of a linear array with three evenly-spaced, identical, spherical thin-shell transducer elements at "*ka*=1" (f=474 Hz). The inter-element spacing is equal to $\lambda/2$ where λ is the acoustic wavelength. In terms of amplitudes, the broadside is the major lobe, and a nodal surface does not exist. Instead of the expected conical nodal surface, some degradation is observed between broadside and end fire.

Figure 5.3 is the normalized vertical beam pattern of the three evenly-spaced, identical, spherical thin-shell transducers. The inter-element spacing is equal to $\lambda/2$. Figure 5.3b and Figure 5.3c compares the patterns obtained from the T-matrix method versus the point sources. The T-matrix beam pattern shows the severe interaction at end fire. The end fire lobe has 3 dB greater amplitude than the broadside lobe (main lobe). The degradation of amplitudes was observed at -132^o, -47^o, 47^o, and 132^o, but the point sources beam pattern goes to adjacent nulls at the same angles (Figure 5.3c).

It was suspected that a linear quadrupolar resonance was responsible that we had not previously identified. Examination of the total scattering amplitude revealed very strong linear quadrupolar scattering, about forty times as great as monopolar scattering. An eigenfrequency analysis in the vicinity of the operating frequency (474 Hz) was conducted using the COMSOL Multiphysics finite-element code. A group of five and only five eigenfrequencies were found very close to 474 Hz, at about 477 Hz. These could represent modes for which $n = 2$, $m = –2$ to 2. Mode shapes for these solutions were examined, and all appeared to represent quadrupole modes, with four of the five appearing to display predominantly motion in a plane, with quadrupolar symmetry, and with exactly one appearing to display linear quadrupolar motion. Confirmation that these most likely were indeed quadrupolar resonances was obtained by a second, approximate computation of the resonance frequencies of the axially-symmetric eigenfrequencies of a thin elastic shell in water [26, pp. 281-284], substituting for the Young's modulus and Poisson's ratio the piezoelectric elastic compliance modulus values s_{11}^E and s_{12}^E/s_{11}^E. A linear quadrupole eigenfrequency value of 473 Hz was found.

Seven-Element Array Configuration

Figure 5.4 depicts the 3D normalized far-field beam pattern of the linear array with seven evenly-spaced, identical, spherical thin-shell transducer elements at "*ka*=1" (f=474 Hz). The inter-element spacing is equal to $\lambda/2$. The width of the main lobe is reduced, and the directivity is enhanced in this configuration compared to the three element array. Two conical nodal surfaces are seen between broad side and end fire.

Figure 5.5 is the normalized vertical beam pattern of the seven evenly-spaced, identical, spherical thin-shell transducers. The inter-element spacing is equal to $\lambda/2$. Figure 5.5b and Figure 5.5c compare the patterns obtained from the T-matrix method versus the point sources. Near the broadside, the behavior of beam patterns is almost the same as that of the point sources. The difference is increased near and at the end fire direction. Separation between lobes cannot be detected easily. Three minor lobes were smeared by one wide lobe. While six adjacent nulls appear in the beam pattern of the point sources, only one adjacent null occurs in the T-matrix method.

Eight-Element Array Configuration

Figure 5.6 depicts the 3D normalized far-field beam pattern of the linear array with eight evenly-spaced, identical, spherical thin-shell transducer elements at "*ka*=1" (f=474 Hz). The inter-element spacing is equal to $\lambda/2$. Three conical nodal surfaces were observed.

Figure 5.7 shows explicitly the difference between the two methods for angles near end fire. The T-matrix method does not produce a null to the end fire direction, while the point sources do. The Figures 5.7b and 5.7c show that the amplitude values of the T-matrix method away from broadside are slightly higher than the point sources in the neighborhood of end fire.

Three-Element Array Configuration With Different Inter-Element Spacing Distance

Figure 5.3 shows the severe interaction effect at the end fire where the side lobe has a larger amplitude than the main lobe. To investigate further the array interaction of the three-element configuration, different inter-element spacing distances for the three-element array were examined. Figure 5.8 illustrates the effect of an inter-element spacing on the three-element array when "*ka*=1." The inter-element spacing distances are selected arbitrarily between $\lambda/2$-$\lambda/4$. Figures 5.8a and 5.8b show that the $\lambda/2$ and $\lambda/2.2$ inter-element spacing distances produce larger side lobe than main lobe. Figures 5.8c through 5.8i illustrate the shading of the end fire is reduced with respect to the decreasing inter-element spacing distance, and it reaches a minima when spacing distance equals $\lambda/3$. Although the two methods show some difference in amplitude, they have the same beam pattern behavior.

Array Configuration With Different Numbers of Elements

To determine the effect of the number of elements in an array, several different configurations were examined. Figures 5.9 and 5.10 represent the far-field beam patterns for differing *N* (numbers of elements in the vertical array). The elements are spaced equally and the inter-element spacing is fixed at $\lambda/2$. For convenience, the configurations with an even number of elements and those with an odd number are analyzed in separate figures.

Figure 5.9 shows the end fire shading is reduced respectively for an increasing number of elements in an array. When the number of elements in an array is more than three, the nulls which are predicted near the end fire in the point sources are shadowed. An analogous shadowing effect occurs near the broadside when the number of the elements in an array is equal to 11 (Figure 5.9e).

Figure 5.10 shows the configurations for even-numbered array elements. The adjacent null is produced at end fire for all even number configuration in point sources due to the axis of symmetry while the T-matrix method beam patterns display the array interaction effect, and the beam pattern does not terminate at the adjacent nulls at the end fire.

Figures 5.11 and 5.12 demonstrate the 3D normalized far-field beam pattern for the different number configurations corresponding to Figures 5.9 and 5.10. The directionality of the array increases with respect to *N*. The worst directionality appears in Figure 5.11a where the major lobe seems to be at the end fire. As shown in Figure 5.11c, Figure 5.11f, and the Figure 5.12b some of the estimated conical nodal surfaces disappear.

Summary of Results for Linear Arrays of Spherical Thin-Shell Transducers

1. The observation of the three-element array configuration shows that for the T-matrix result, the end-fire lobe is 3 dB greater than the broadside lobe (5.3). The strong array interaction was found to be due to strong linear quadrupole scattering. This was traced to an uncontrolled (not able to be driven) linear quadrupole resonance of the transducer, at 477 Hz. The array interaction cause a “shading” in this case and reduce the amplitude of the major lobe.
2. For the T-matrix results, the consistent “shadowing” effect is manifested by a reduction in destructive interference, and so true nulls do not occur.
3. The “shadowing” effect disappears when the inter-element spacing distance is $\lambda/3$ for the three element array (Figure 5.8f).
4. The configurations of the linear arrays with different *N* number of the elements, are shown

in Figures 5.9 and 5.10, which indicate that the “shading” effect is reduced with respect to the increasing number of elements while the “shadowing” effect is increased. It can be concluded that the "shading" effect due to scattering is reduced by increasing the number of elements in an array.

5. It should be noted that the beam pattern of both methods is the same at broadside when the number of elements in an array is more than three (Figures 5.9 and 5.10).
6. The least desirable array configuration of the spherical thin-shells was observed for a three-element array with $\lambda/2$ inter element spacing, because the side lobe dominated the broadside major lobe (Figure 5.8a).

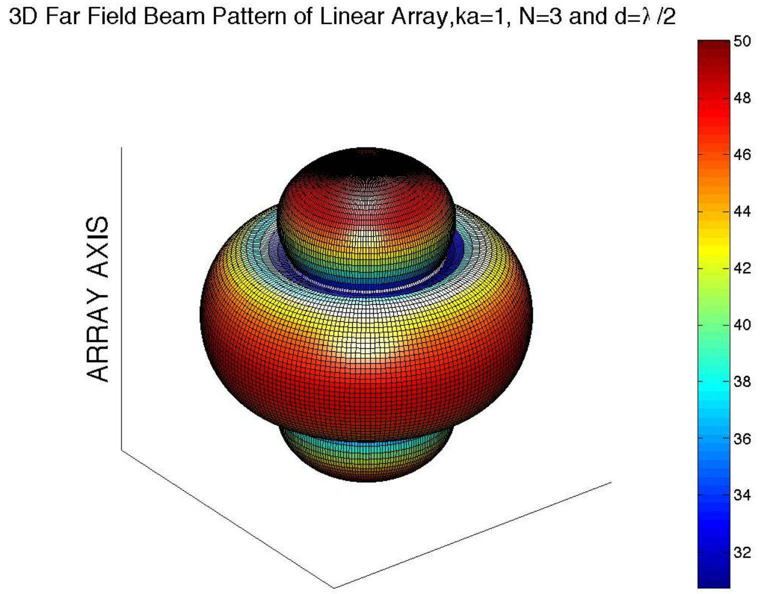

Figure 5.2: 3D front-left view of normalized far-field beam pattern of vertical linear array with three identical spherical thin-shell transducer elements obtained with the T-matrix method,inter-element spacing d=$\lambda/2$, f=474 Hz and ka=1.

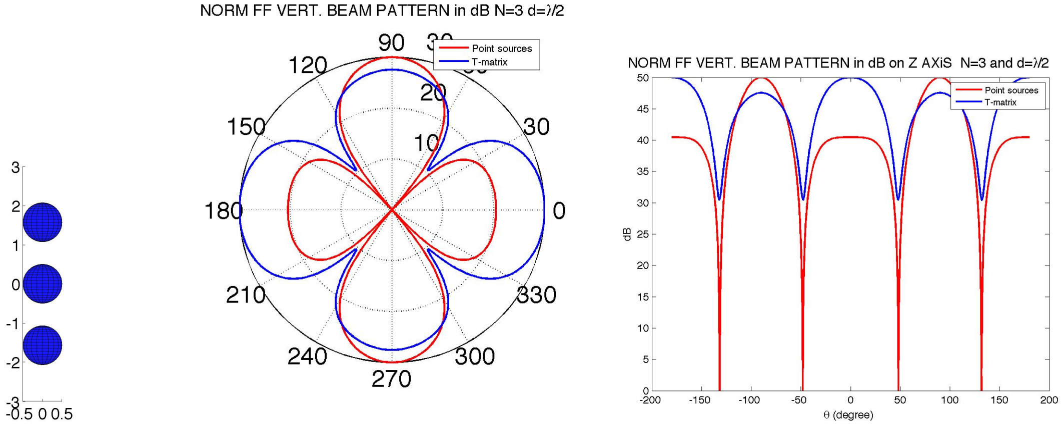

(a) (b) (c)

Figure 5.3: Normalized far-field vertical beam pattern for the modeled linear array with three identical spherical thin-shell transducer elements lying along polar axis ($\theta = 0$), inter-element spacing d=$\lambda/2$, f=474 Hz and ka=1. (a) Orientation of the spherical thin-shell transducers (b) A polar plot of the normalized magnitudes of the vertical far-field beam pattern (c) A plot of the normalized magnitudes of the vertical far-field beam pattern

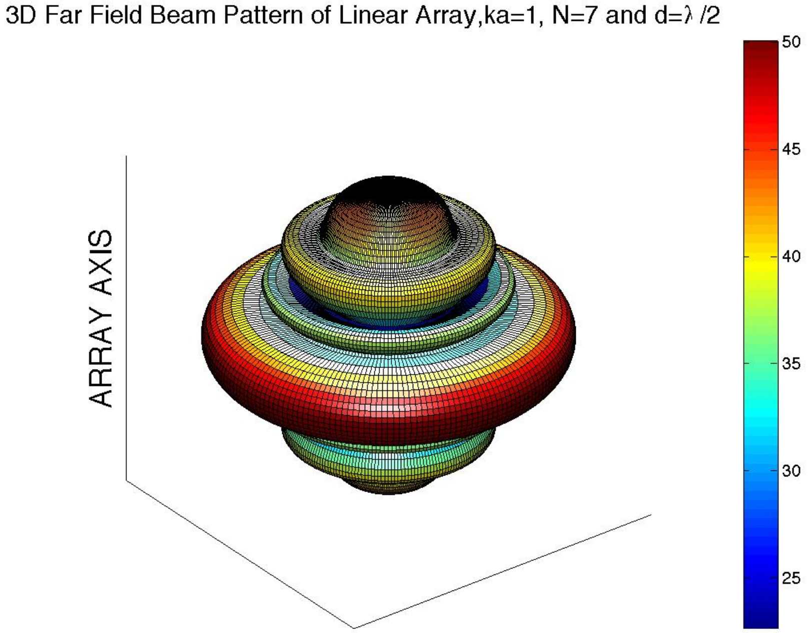

Figure 5.4: 3D front-left view of normalized far-field beam pattern of vertical linear array with seven identical spherical thin-shell transducer elements obtained with the T-matrix method, inter-element spacing d=$\lambda/2$, f=474 Hz and ka=1

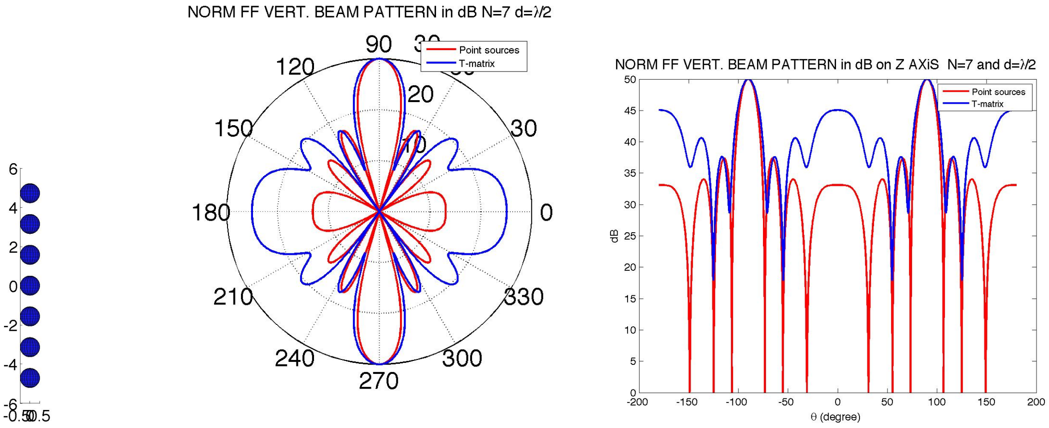

(a) (b) (c)

Figure 5.5: Normalized far-field vertical beam pattern for the modeled linear array with seven identical spherical thin-shell transducer elements lying along polar axis ($\theta = 0$), inter-element spacing d=$\lambda/2$, f=474 Hz and ka=1. (a) Orientation of the spherical thin-shell transducers (b) A polar plot of the normalized magnitudes of the vertical far-field beam pattern (c) A plot of the normalized magnitudes of the vertical far-field beam pattern

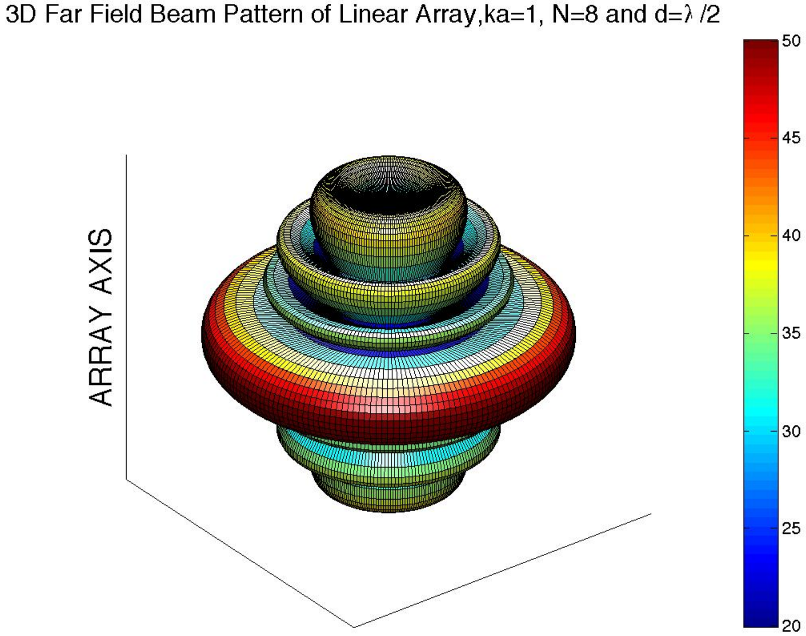

Figure 5.6: 3D front-left view of normalized far-field beam pattern of vertical linear array with eight identical spherical thin-shell transducer elements obtained with the T-matrix method, inter-element spacing d=$\lambda/2$, f=474 Hz and ka=1

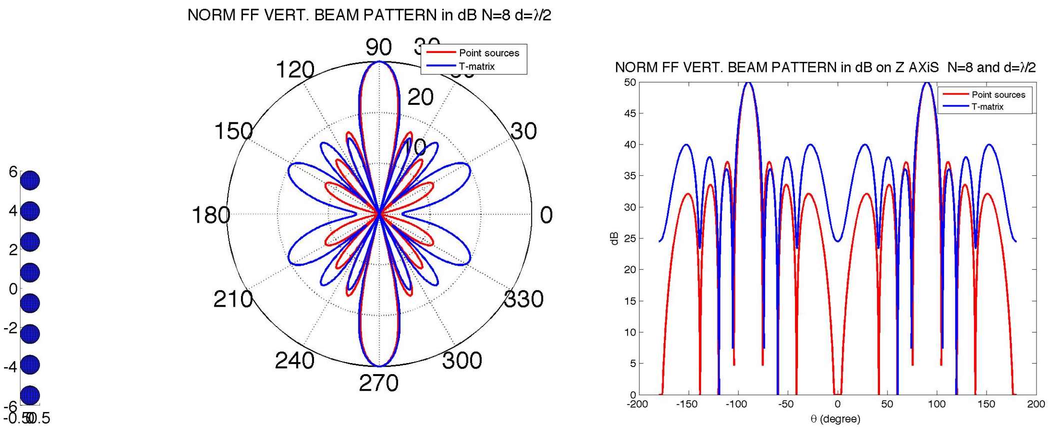

(a) (b) (c)

Figure 5.7: Normalized far-field vertical beam pattern for the modeled linear array with three identical spherical thin-shell transducer elements lying along polar axis ($\theta = 0$), inter-element spacing d=$\lambda/2$, f=474 Hz and ka=1. (a) Orientation of the spherical thin-shell transducers (b) A polar plot of the normalized magnitudes of the vertical far-field beam pattern (c) A plot of the normalized magnitudes of the vertical far-field beam pattern

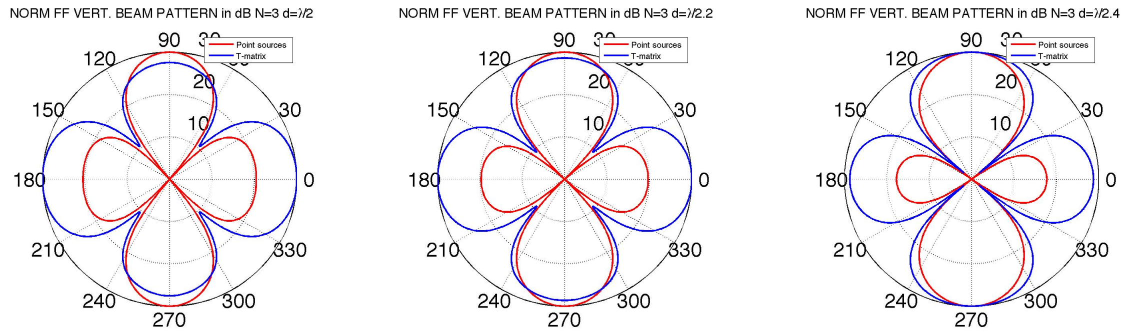

(a) $d = \lambda/2$ (b) $d = \lambda/2.2$ (c) $d = \lambda/2.4$

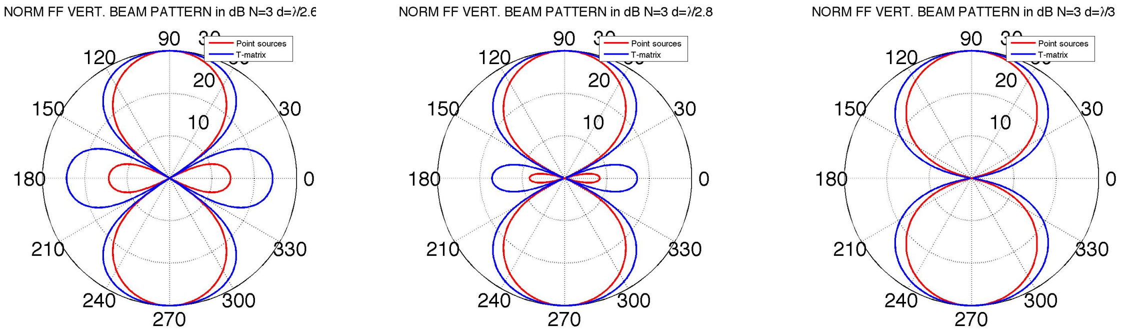

(d) $d = \lambda/2.6$ (e) $d = \lambda/2.8$ (f) $d = \lambda/3$

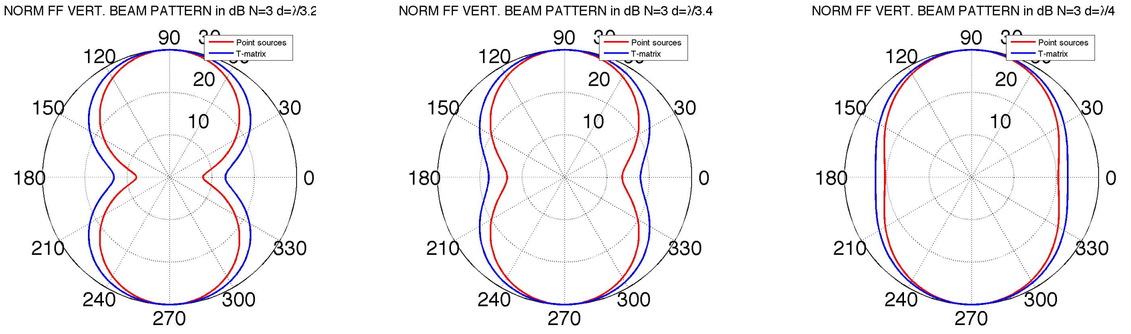

(g) $d = \lambda/3.2$ (h) $d = \lambda/3.4$ (i) $d = \lambda/4$

Figure 5.8: The comparison of the normalized far-field vertical beam patterns of a modeled evenly spaced three-element linear array of spherical thin-shell transducer at f=474 Hz and ka=1 with different inter-element spacing distance (a-i) Comparison of polar plot of the normalized vertical far-field beam pattern of T-matrix method against polar plot of the normalized vertical far-field beam pattern of the point sources.

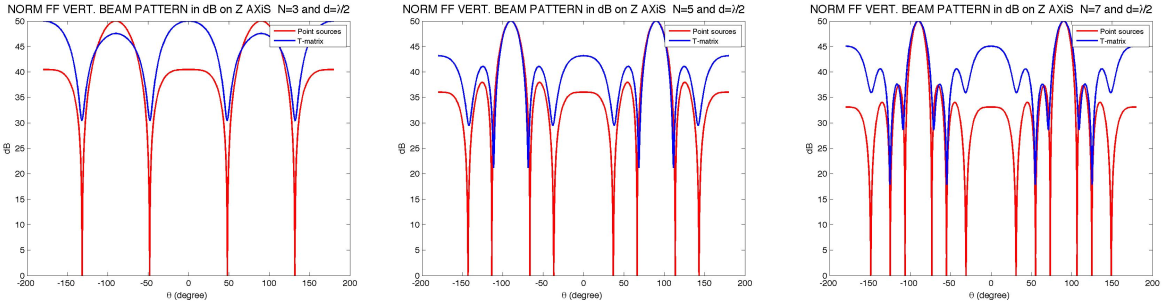

(a) N=3 (b) N=5 (c) N=7

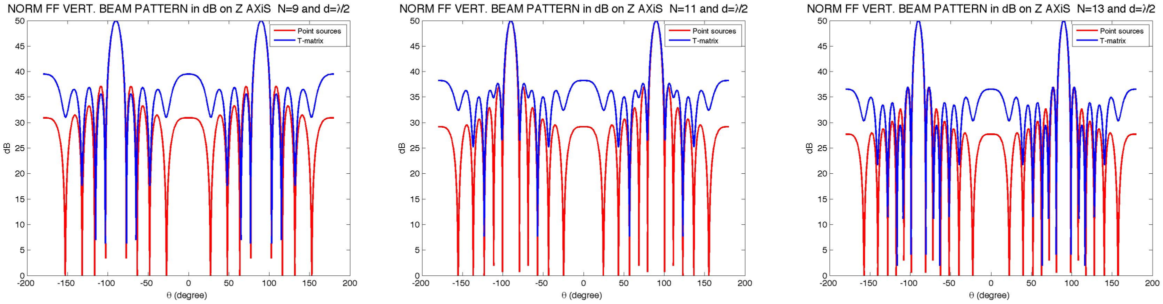

(d) N=9 (e) N=11 (f) N=13

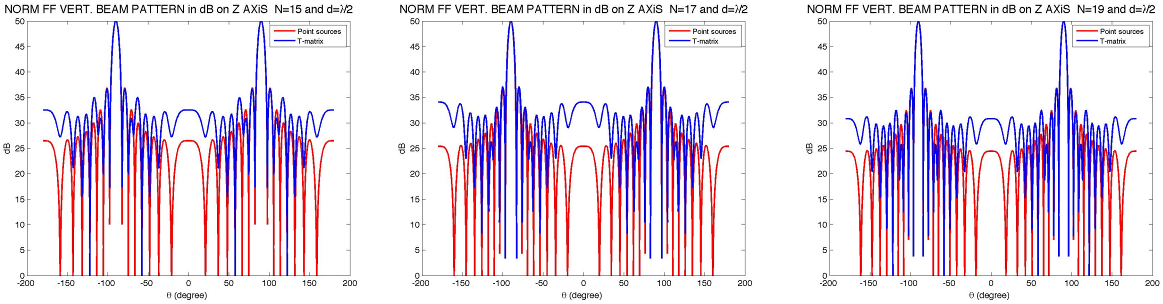

(g) N=15 (h) N=17 (i) N=19

Figure 5.9: The vertical far-field beam patterns for a modeled vertical linear array composed of an odd number N of evenly spaced spherical thin-shell transducer elements lying along the polar axis ($\theta = 0$) at $\lambda/2$, f=474 Hz and ka=1 (a-i) Comparison of cartesian plot of the normalized vertical far-field beam pattern of T-matrix method against cartesian plot of the normalized vertical far-field beam pattern of the point sources.

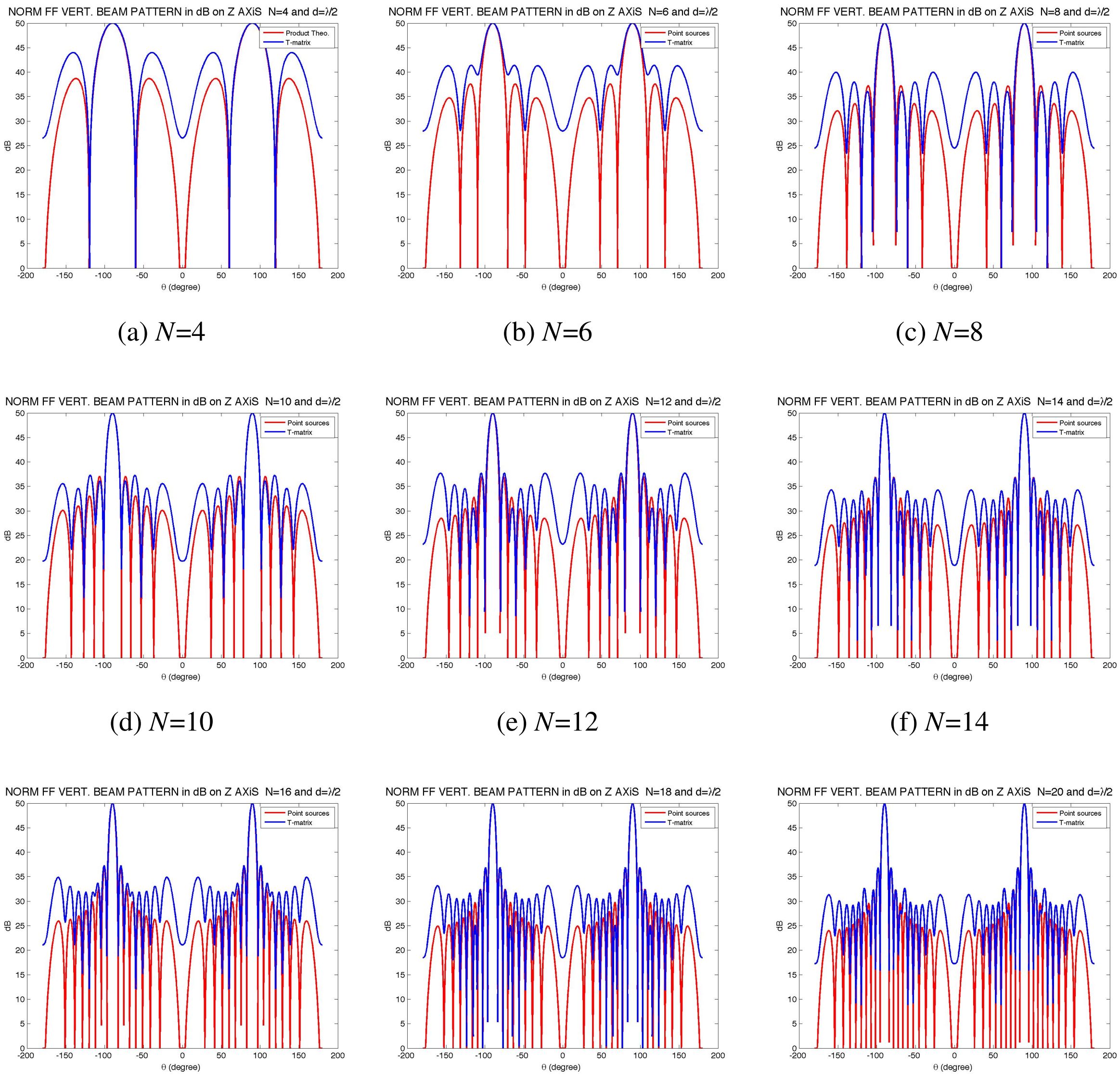

(a) *N*=4 (b) *N*=6 (c) *N*=8

(d) *N*=10 (e) *N*=12 (f) *N*=14

(g) *N*=16 (h) *N*=18 (i) *N*=20

Figure 5.10: The vertical far-field beam patterns for a modeled vertical linear array composed of an even number *N* of evenly spaced spherical thin-shell transducer elements lying along the polar axis ($\theta = 0$) at $\lambda/2$, *f*=474 Hz and *ka*=1 (a-i) Comparison of cartesian plot of the normalized vertical far-field beam pattern of T-matrix method against cartesian plot of the normalized vertical far-field beam pattern of the point sources.

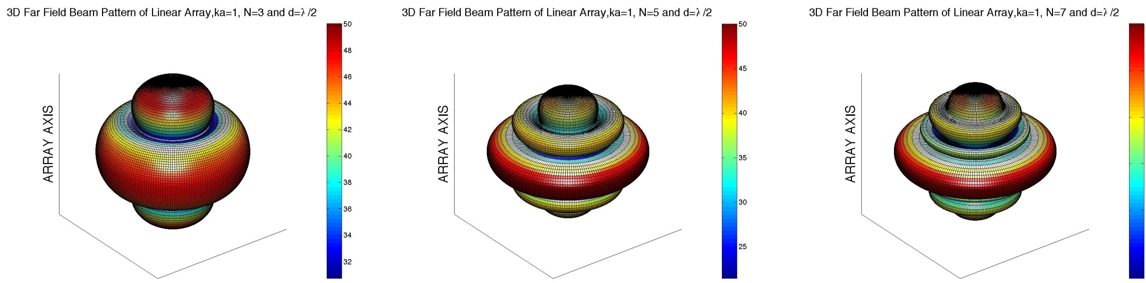

(a) N=3 (b) N=5 (c) N=7

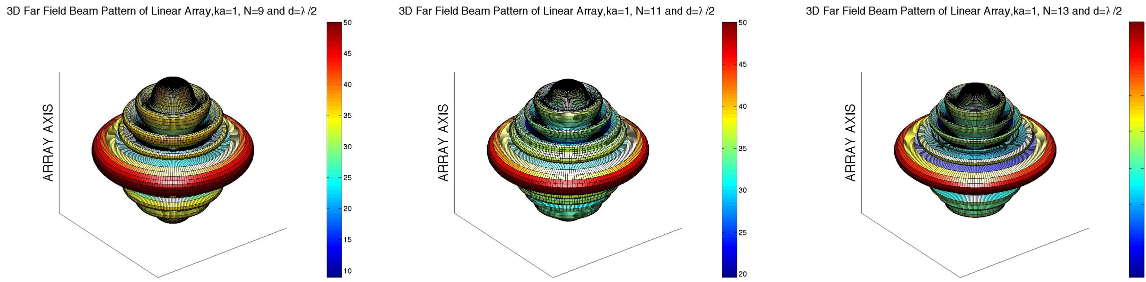

(d) N=9 (e) N=11 (f) N=13

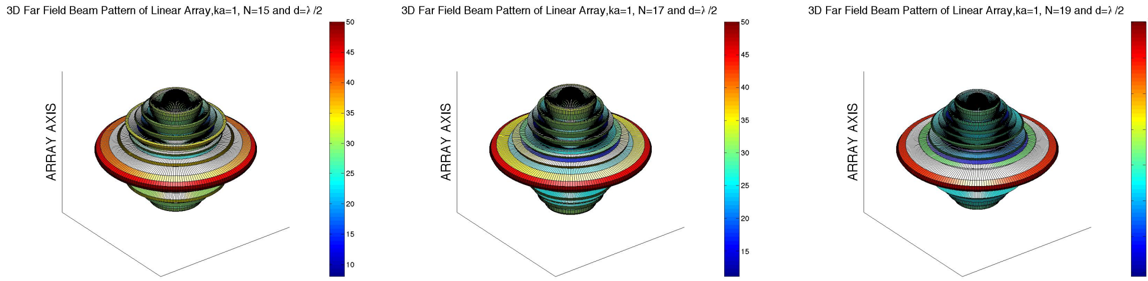

(g) N=15 (h) N=17 (i) N=19

Figure 5.11: The 3D normalized far-field beam patterns for a modeled vertical linear array composed of an odd number N of evenly spaced spherical thin-shell transducer elements lying along the polar axis ($\theta = 0$) at $\lambda/2$, f=474 Hz and ka=1 (a-i) 3D front-left view of far-field beam pattern of vertical linear array

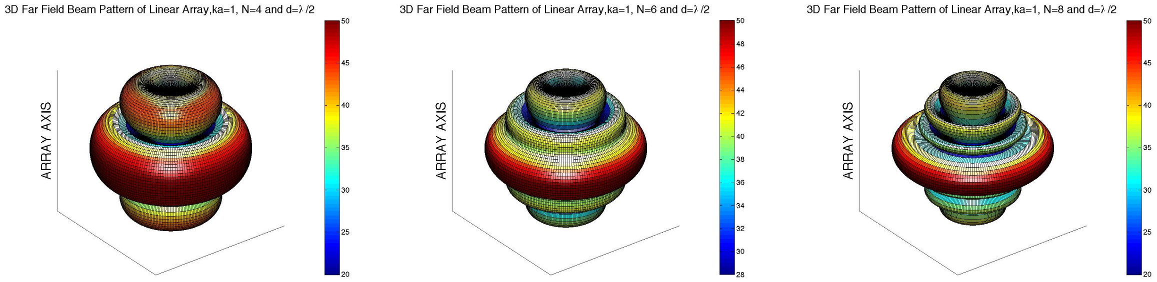

(a) N=4 (b) N=6 (c) N=8

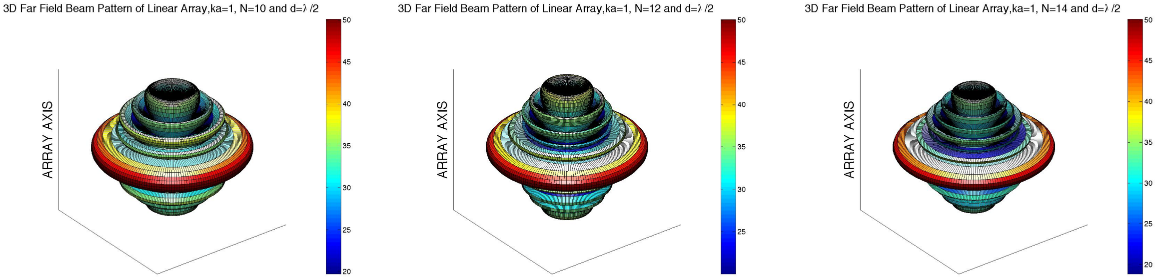

(d) N=10 (e) N=12 (f) N=14

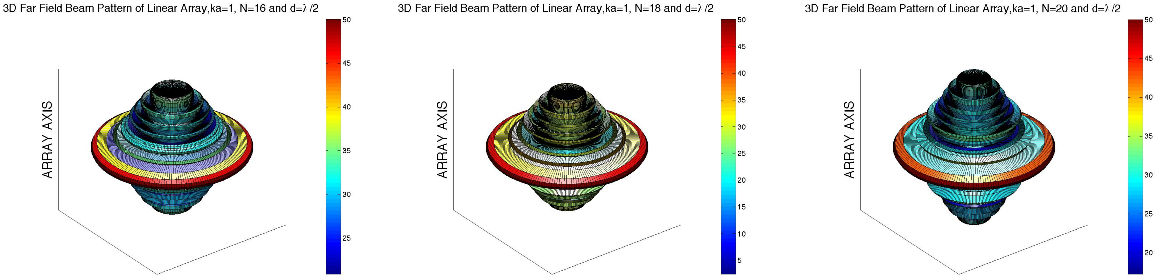

(g) N=16 (h) N=18 (i) N=20

Figure 5.12: The 3D normalized far-field beam patterns for a modeled vertical linear array composed of an even number N of evenly spaced spherical thin-shell transducer elements lying along the polar axis ($\theta = 0$) at $\lambda/2$, f=474 Hz and ka=1 (a-i) 3D front-left view of far-field beam pattern of vertical linear array.

5.6.2 The Linear Array with the Ring-Shell Elements

Three-Element Array Configuration

Figure 5.13 depicts the 3D normalized far-field beam pattern of a linear array with three evenly-spaced, identical, ring-shell transducer elements at "*ka*=1" (f=605 Hz). The inter-element spacing is equal to $\lambda/2$. It is remarkable that the conical nodal surfaces do not degrade relative to broadside at end fire

Figure 5.14 is the normalized vertical beam pattern of the three evenly-spaced, identical, ring-shell transducers. The inter-element spacing is again equal to $\lambda/2$. Figures 5.14b and 5.14c compare the beam patterns obtained from the T-matrix method versus the point source method. Unlike for the spherical thin shell transducers, the beam patterns for the ring shell transducers are nearly the same for both techniques except true nulls do not occur in T-matrix method. This is probably due to two things:

1. The ring-shell transducers are operated at resonance (controlled), where the spherical shells were not.
2. There is no evidence of a spurious (uncontrolled) resonance at the operating frequency for the ring-shell transducers, but there was for the spherical shell transducers.

Seven-Element Array Configuration

Figure 5.15 depicts the 3D normalized far-field beam pattern of a linear array with seven evenly-spaced, identical, ring-shell transducer elements at "*ka*=1" (f=605 Hz). The inter-element spacing is again equal to $\lambda/2$. The width of the main lobe is reduced, and the directivity is enhanced in this configuration compared to the three element array. Three conical nodal surfaces can clearly be seen in the figure.

Figure 5.16 is the normalized beam pattern of the seven evenly-spaced, identical, ring-shell transducers. The inter-element spacing is equal to $\lambda/2$. Figures 5.16b and 5.16c compare the patterns obtained from the T-matrix method versus the point source calculation. Although the beam patterns of the T-matrix seem almost the same as the beam patterns obtained using point sources near broadside, Figure 5.16c shows beam patterns obtained using T-matrices do not produce nulls as do the point sources. Also, a 2 dB reduction was observed at end fire for the T-matrix compared to point sources.

Eight-Element Array Configuration

Figure 5.17 depicts the 3D normalized far-field beam pattern of the linear array with eight evenly-spaced, identical, ring-shell transducer elements at "*ka*=1" (f=605 Hz). The inter-element spacing is equal to $\lambda/2$. Four conical nodal surfaces are clearly seen from the figure.

Although the difference between the two methods is practically indistinguishable at broadside, Figure 5.18 shows an interaction effect near the end fire in the detailed plot of amplitudes, shown in Figure 5.18c, demonstrating the T-matrix method does not produce nulls at end fire while the point source method does. Also it should be noted the adjacent nulls do not exist for the T-matrix method.

Three-Element Array Configuration With Different Inter-Element Spacing Distance

Figure 5.19 illustrates the effect of an inter-element spacing on the three-element array with "*ka*" equal to one. The inter-element spacing distances are arbitrarily selected between $\lambda/2$-$\lambda/4$. Figures 5.19a through 5.19i show that decreasing the inter-element distances increases array interaction. The largest difference is observed for the configuration of the $\lambda/3$ (Figure 5.19f). The difference between the product theory and the T-matrix method are clearly observed near the end fire of this configuration.

Array Configurations With Different Numbers of Elements

To determine the effect of the number of elements in an array, different configurations were examined. Figures 5.20 and 5.21 represent the far-field beam patterns for different numbers N of elements. The elements are spaced equally, and inter-element spacing is fixed at $\lambda/2$. For convenience, even numbers of elements and odd numbers of elements are displayed in separate figures.

Figure 5.21 shows the configurations for the even numbers. At end fire, an adjacent null is presented with an even number of elements using the point sources due to the axis of symmetry; while the beam pattern obtained using the T-matrix shows array interaction effects and produces a beam pattern that does not terminate at adjacent nulls at end fire.

Figures 5.22 and 5.23 demonstrate the 3D normalized far-field beam pattern for the different configurations corresponding to figure Figure 5.20 and Figure 5.21. The directionality of the array increases with N. Almost all of the estimated conical nodal surfaces by point sources are clearly observed.

Summary of Results for Linear Arrays of Ring-Shell Transducers

1. The figures illustrate the difference between the two methods is not remarkable except for the end fire direction. Unlike the linear array of spherical thin-shell transducer, the 'shading" effect disappears for this configuration. Only the shadowing effect is produced near the end fire, and it is remarkable for even numbered configurations.

2. The most significant scattering effect was observed when the inter-element spacing was $\lambda/3$. A spacing smaller than $\lambda/3$ resulted in local maxima on axis where the spherical shell and point source arrays both show local minima. The relative consistency of axial to broadside amplitude for the ring-shell array is probably due to its being generated at resonance.
3. The Figures 5.8 and 5.19 showed that for the spherical thin-shell array, the qualitative shape of the beam patterns is the same, e.g., the angles of local maxima and minima. However, for the ring-shell array, regardless of the spacing, the on-axis response appears to be consistently about 7 dB smaller than the broadside response.
4. The least desirable array configuration of the ring-shells was observed for $\lambda/3$ inter element-spacing distance (Figure 5.19f).

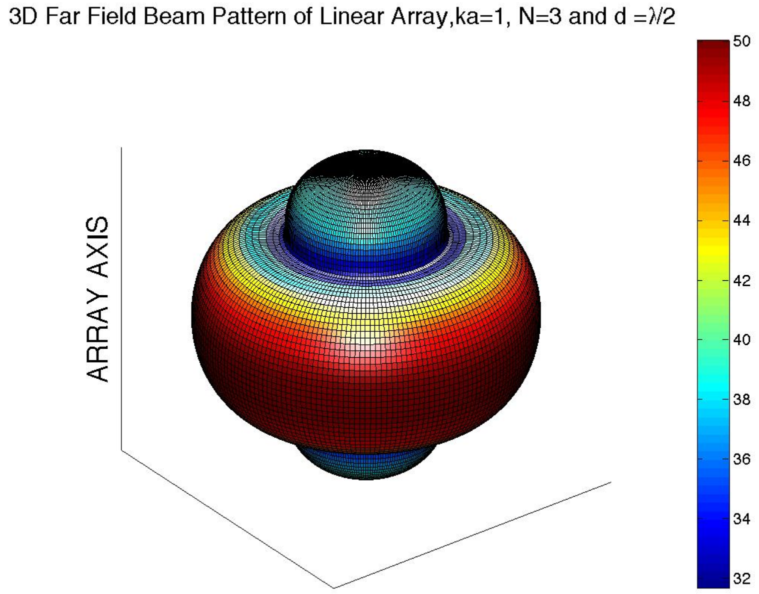

Figure 5.13: 3D front-left view of normalized far field beam pattern of vertical linear array with three ring-shell transducer elements obtained with the T-matrix method,inter-element spacing d=$\lambda/2$, f=605 Hz and ka=1.

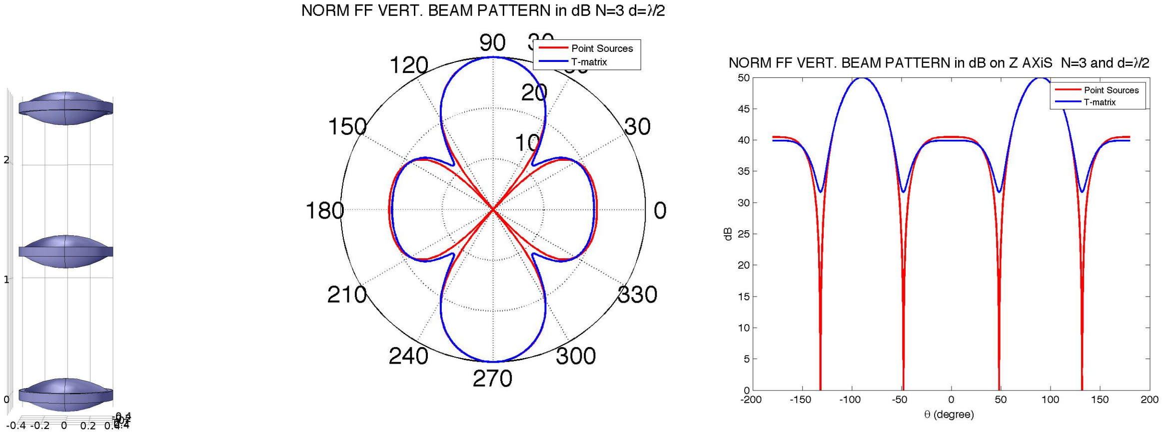

(a) (b) (c)

Figure 5.14: Normalized far-field vertical beam pattern for the modeled linear array with three identical ring-shell transducer elements lying along polar axis ($\theta = 0$), inter-element spacing d=$\lambda/2$, f=605 Hz and ka=1. (a) Orientation of the ring-shell transducers (b) A polar plot of the normalized magnitudes of the vertical far-field beam pattern (c) A plot of the normalized magnitudes of the vertical far-field beam pattern

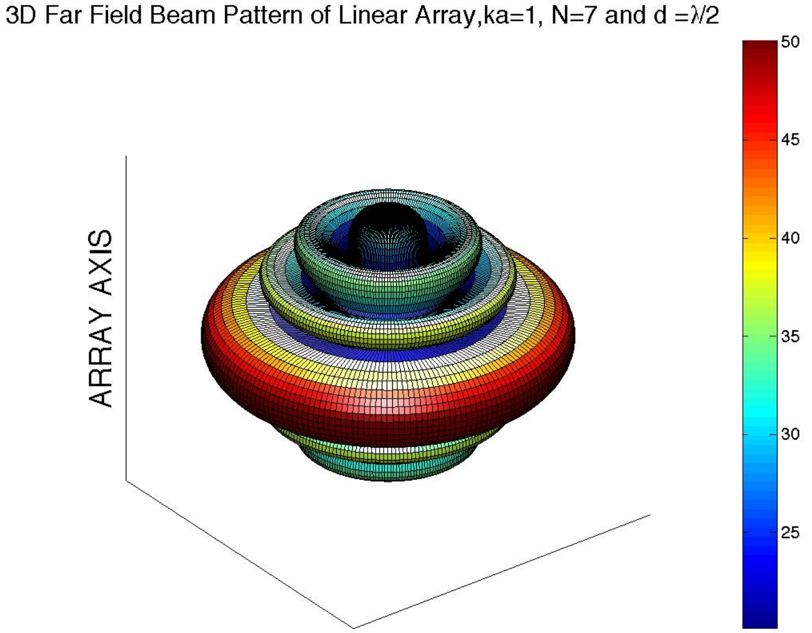

Figure 5.15: 3D front-left view of normalized far field beam pattern of vertical linear array with seven ring-shell transducer elements obtained with the T-matrix method, inter-element spacing d=$\lambda/2$, f=605 Hz and ka=1.

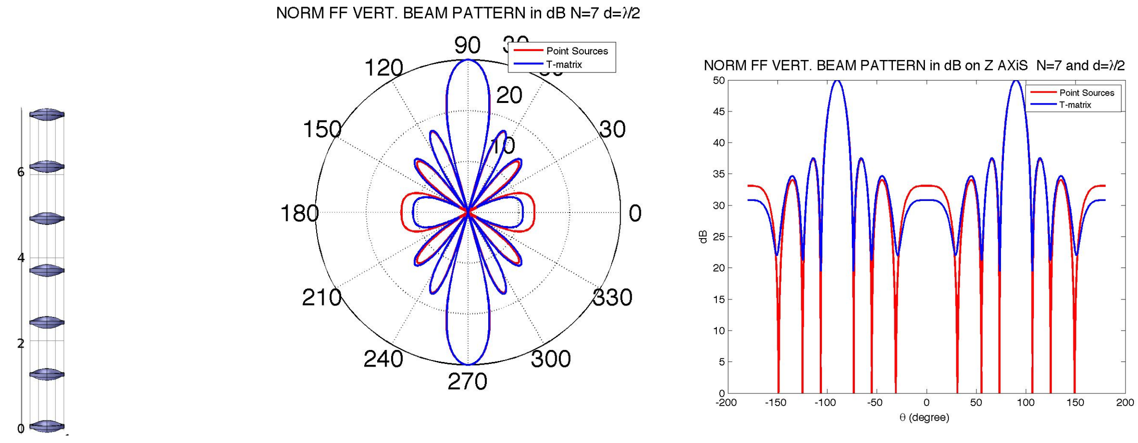

(a) (b) (c)

Figure 5.16: Normalized far-field vertical beam pattern for the modeled linear array with seven identical ring-shell transducer elements lying along polar axis ($\theta = 0$), inter-element spacing d=$\lambda/2$, f=605 Hz and ka=1. (a) Orientation of the ring-shell transducers (b) A polar plot of the normalized magnitudes of the vertical far-field beam pattern (c) A plot of the normalized magnitudes of the vertical far-field beam pattern

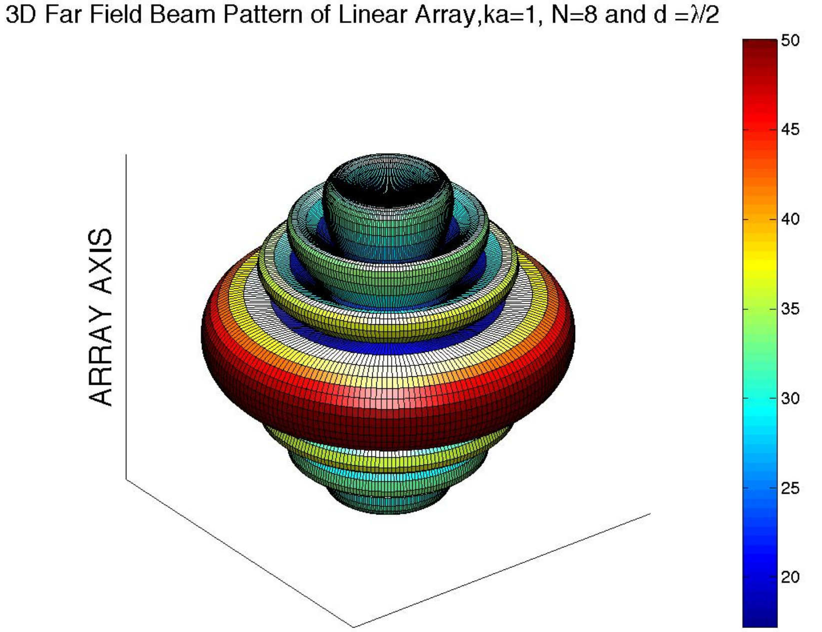

Figure 5.17: 3D front-left view of normalized far field beam pattern of vertical linear array with eight ring-shell transducer elements obtained with the T-matrix method, inter-element spacing d=$\lambda/2$, f=605 Hz and ka=1.

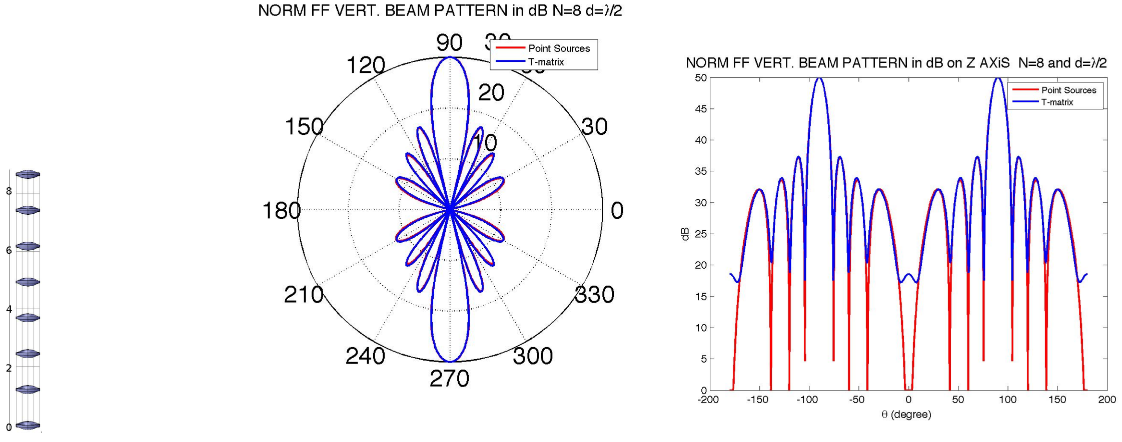

(a) (b) (c)

Figure 5.18: Normalized far-field vertical beam pattern for the modeled linear array with eight identical ring-shell transducer elements lying along polar axis ($\theta = 0$), inter-element spacing d=$\lambda/2$, f=605 Hz and ka=1. (a) Orientation of the ring-shell transducers (b) A polar plot of the normalized magnitudes of the vertical far-field beam pattern (c) A plot of the normalized magnitudes of the vertical far-field beam pattern

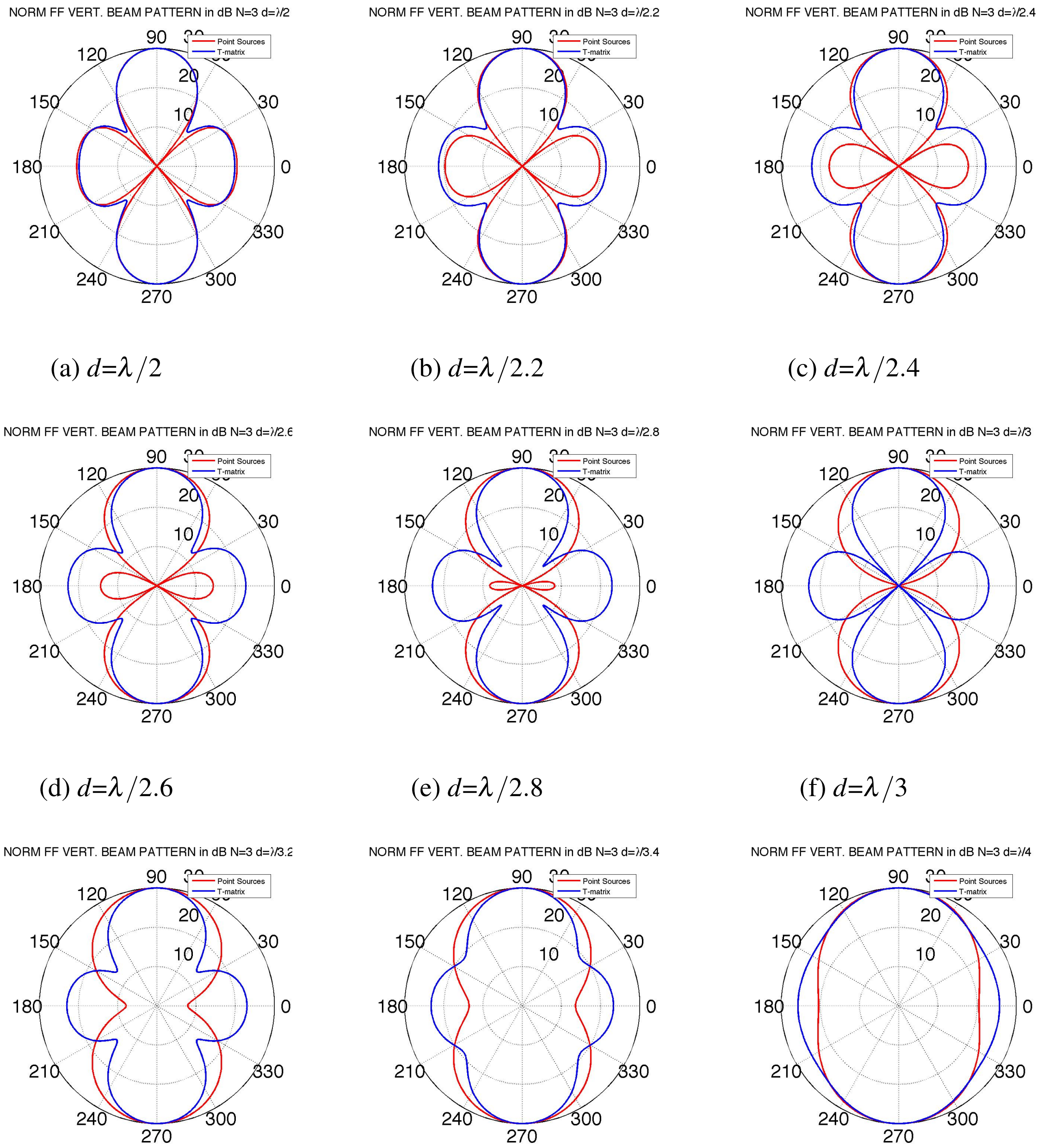

(a) d=$\lambda/2$ (b) d=$\lambda/2.2$ (c) d=$\lambda/2.4$

(d) d=$\lambda/2.6$ (e) d=$\lambda/2.8$ (f) d=$\lambda/3$

(g) d=$\lambda/3.2$ (h) d=$\lambda/3.4$ (i) d=$\lambda/4$

Figure 5.19: The comparison of the far-field vertical beam patterns of a modeled evenly spaced three-element linear array of the ring-shell at f=605 Hz and ka=1 with different inter-element spacing distance (a-i) Comparison of polar plot of the normalized vertical far-field beam pattern of T-matrix method against polar plot of the normalized vertical far-field beam pattern of the point sources.

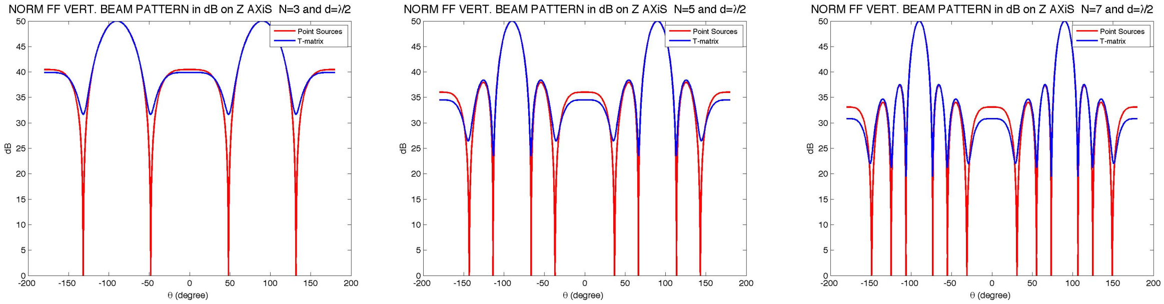

(a) *N*=3 (b) *N*=5 (c) *N*=7

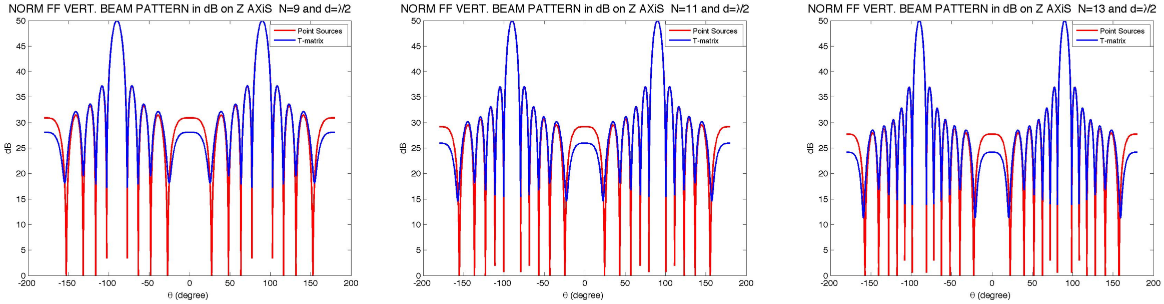

(d) *N*=9 (e) *N*=11 (f) *N*=13

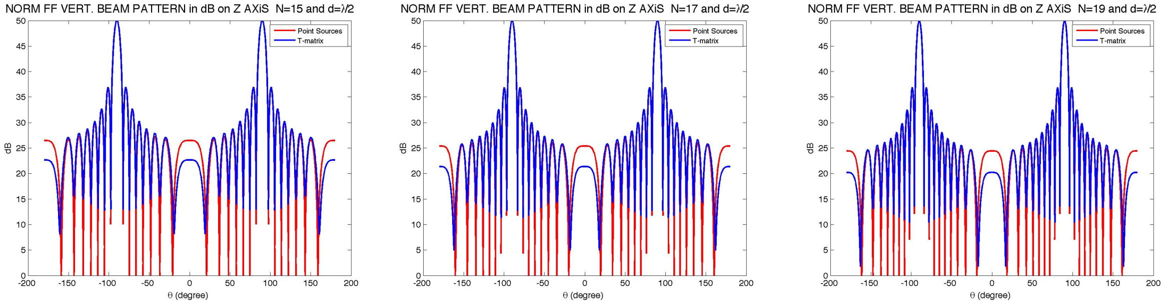

(g) *N*=15 (h) *N*=17 (i) *N*=19

Figure 5.20: The vertical far-field beam patterns for a modeled vertical linear array composed of an odd number N of evenly spaced flextensional transducer elements lying along the polar axis ($\theta = 0$) at $\lambda/2$, f=605 Hz and ka=1 (a-i) Comparison of cartesian plot of the normalized vertical far-field beam pattern of T-matrix method against cartesian plot of the normalized vertical far-field beam pattern of the point sources.

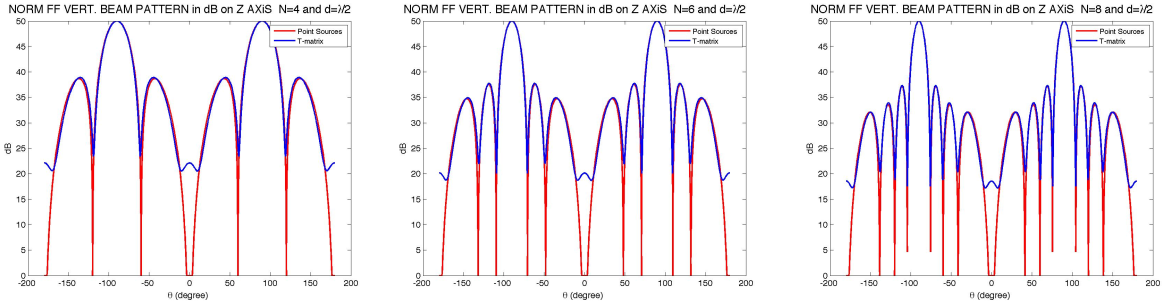

(a) N=4 (b) N=6 (c) N=8

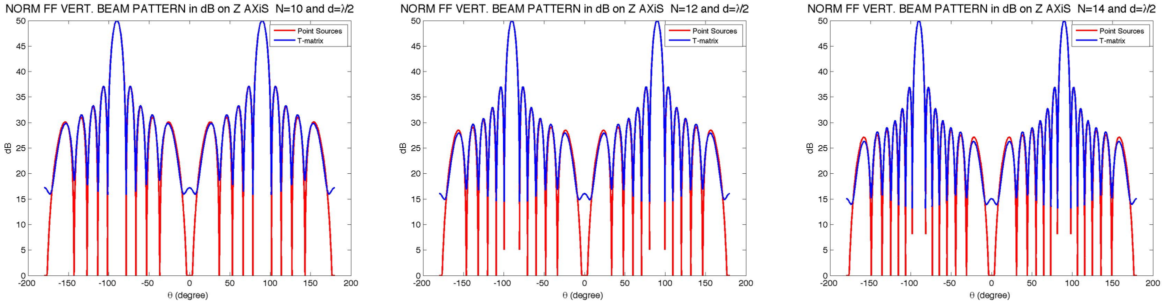

(d) N=10 (e) N=12 (f) N=14

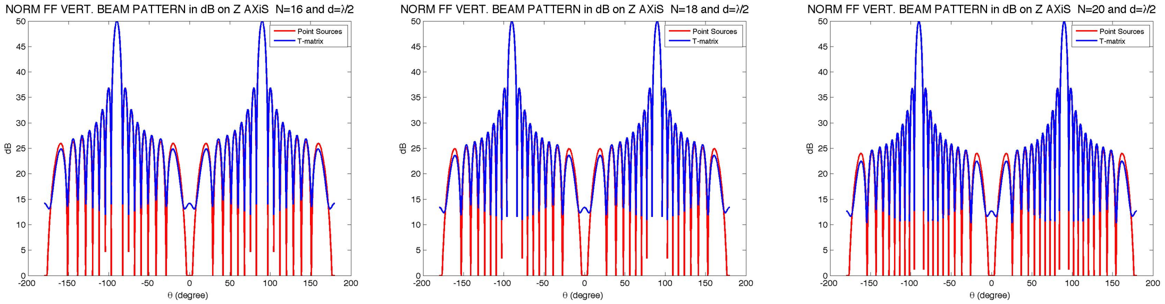

(g) N=16 (h) N=18 (i) N=20

Figure 5.21: The vertical far-field beam patterns for a modeled vertical linear array composed of an even number N of evenly spaced spherical thin-shell transducer elements lying along the polar axis ($\theta = 0$) at $\lambda/2$, f=605 Hz and ka=1 (a-i) Comparison of cartesian plot of the normalized vertical far-field beam pattern of T-matrix method against cartesian plot of the normalized vertical far-field beam pattern of the point sources.

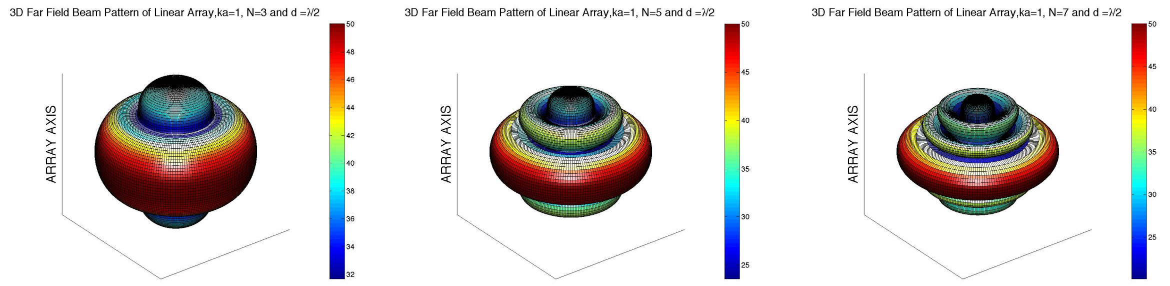
3D Far Field Beam Pattern of Linear Array,ka=1, N=3 and d =λ/2

3D Far Field Beam Pattern of Linear Array,ka=1, N=5 and d =λ/2

3D Far Field Beam Pattern of Linear Array,ka=1, N=7 and d =λ/2

(a) N=3 (b) N=5 (c) N=7

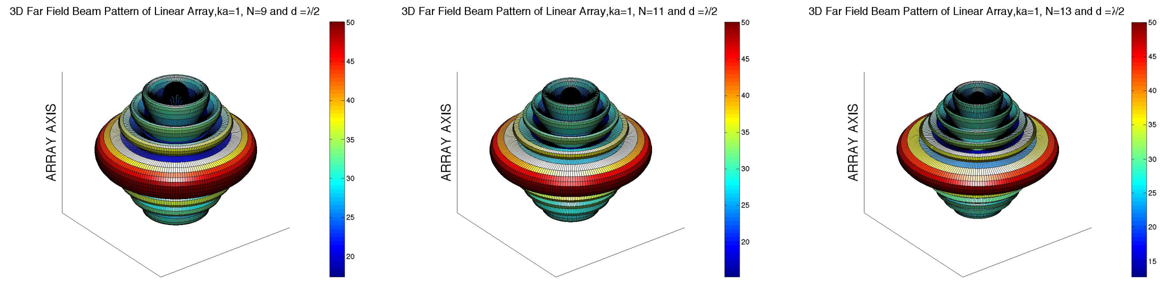
3D Far Field Beam Pattern of Linear Array,ka=1, N=9 and d =λ/2

3D Far Field Beam Pattern of Linear Array,ka=1, N=11 and d =λ/2

3D Far Field Beam Pattern of Linear Array,ka=1, N=13 and d =λ/2

(d) N=9 (e) N=11 (f) N=13

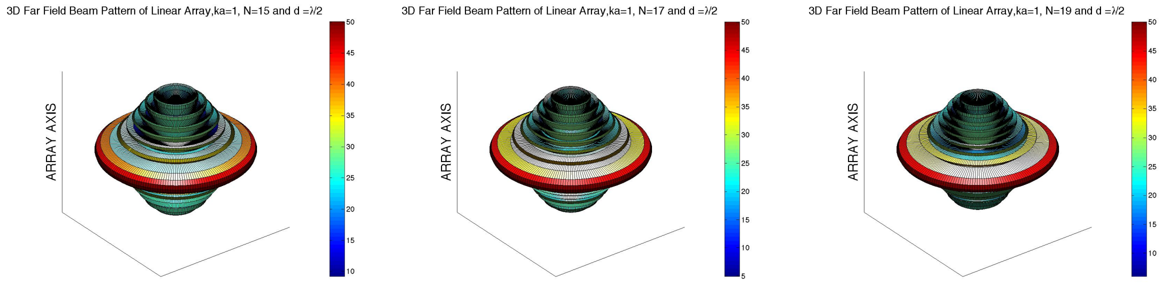
3D Far Field Beam Pattern of Linear Array,ka=1, N=15 and d =λ/2

3D Far Field Beam Pattern of Linear Array,ka=1, N=17 and d =λ/2

3D Far Field Beam Pattern of Linear Array,ka=1, N=19 and d =λ/2

(g) N=15 (h) N=17 (i) N=19

Figure 5.22: The 3D normalized far-field beam patterns for a modeled vertical linear array composed of an odd number N of evenly spaced spherical thin-shell transducer elements lying along the polar axis ($\theta = 0$) at $\lambda/2$, f=605 Hz and ka=1 (a-i) 3D front-left view of normalized far-field beam pattern of vertical linear array

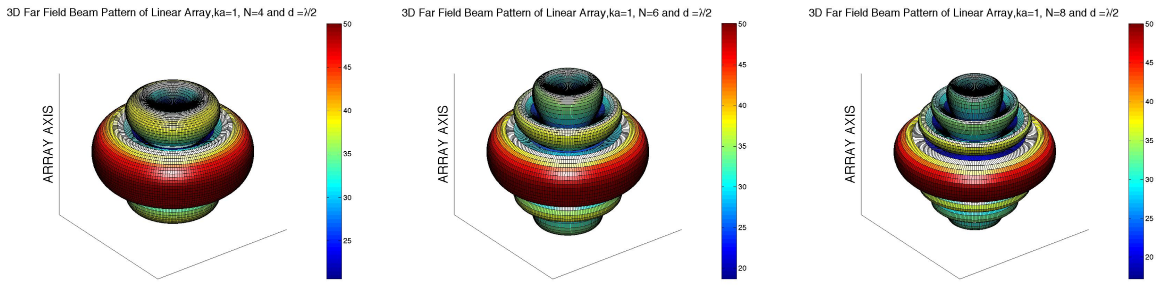

(a) N=4 (b) N=6 (c) N=8

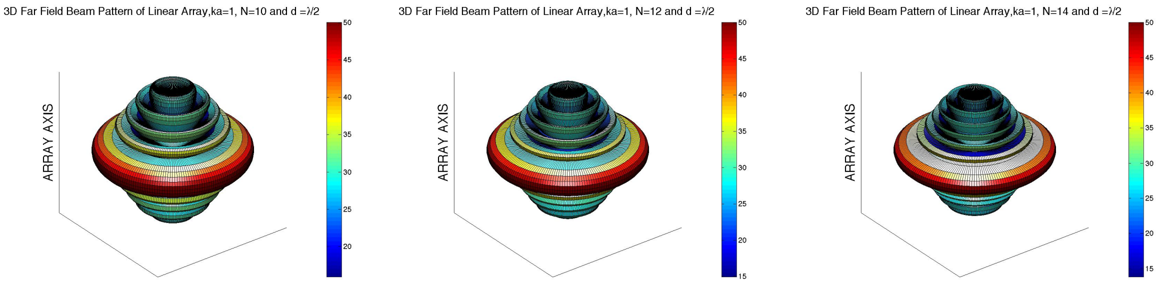

(d) N=10 (e) N=12 (f) N=14

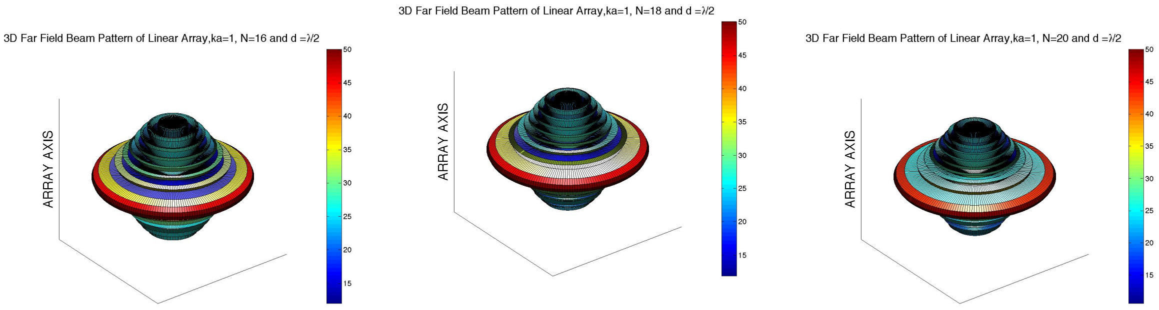

(g) N=16 (h) N=18 qualitative (i) N=20

Figure 5.23: The 3D normalized far-field beam patterns for a modeled vertical linear array composed of an even number N of evenly spaced spherical thin-shell transducer elements lying along the polar axis ($\theta = 0$) at $\lambda/2$, f=605 Hz and ka=1 (a-i) 3D front-left view of normalized far-field beam pattern of vertical linear array.

5.7 General Conclusion

The characteristics of beam patterns were obtained using the T-matrix method for modeling a vertical linear array comprised of spherical thin shell transducer elements and a vertical linear array comprised of ring-shell transducer elements at "*ka*=1." Results obtained with the T-matrix were compared with for point source arrays. While, both approaches are in agreement near broadside, they differ from each other near and at the end fire directions. This is expected because the point sources ignore array element interaction while the T-matrix method considers this affect. Such interactions, if they stimulate uncontrolled resonances, as is the case for the spherical shell transducer, can result in large deviations from point-source behavior.

Array element interactions cause the degradation or the "shadowing" in amplitude of beam pattern amplitudes near end fire. The shadowing or degradation is induced by scattering since the scattering produces a destructive interference in an array and changes the radiation away from broadside. As a result of these interactions, side lobes smear the minor lobes and shadow the adjacent null. In particular, this effect can be seen in 3D beam patterns. The nodal surfaces disappear or interfere with the closest side lobes, resulting in the expected nodal surface not terminating at an adjacent null (e.g., Figure 5.4, Figure 5.13).

To investigate the scattering characteristics, the pressure amplitudes (e.g, outgoing, scattered, radiated) are normalized with the monopole radiated pressure amplitude, P^r_{00}. The normalized pressure amplitudes are multiplied by phase factors of the far-field Hankel function, $i^{(n+1)}$, in order to see the interaction effect on the radiation pattern explicitly (equation (5.5)). The normalized pressure coefficients are listed in Tables 5.3 through 5.8. The scattering characteristics can be deduced from these tables. The linear quadrupole component dominates the scattering in the array consisting of the spherical shells while monopole scattering dominates the other components of the ring-shell array. This is entirely consistent with the previously mentioned facts that the ring-shell transducers are operated at (mostly monopole) resonance, where the spherical shell transducers are not, and there exists an uncontrolled linear quadrupole resonance of the spherical shell transducers at almost exactly the chosen operating frequency. The differing scattering characteristics demonstrate themselves in Figures 5.5 and 5.16. The increasing side lobes are observed at end fire of the spherical thin-shells, while the side lobes of the ring-shell degrade.

For further investigation to understand the factors affecting the array interaction, the inter-element spacing distance was allowed to vary between $\lambda/2 - \lambda/4$. Resultant figures show the effect of inter-element spacing distances on array sound pressure levels. In particular, when the inter-element spacing distance is equal to the ratio of wavelength to the number of elements, λ/N, significant changes are observed in the beam patterns of Figures 5.19 and 5.8. The array interaction can be controlled by adjusting the inter-element spacing distance in order to minimize this interaction

The second factor considered was the affect the number of elements has on beam pattern for an array. This array interaction effect is attenuated as the number of elements is increased. In conclusion, an optimal number of elements can be determined by analyses of beam patterns to enhance or reduce array element interactions.

N=3	*ka=1 f=474 Hz*	**Magnitude**			**Phase (degree)**		
Nu.	**Comp.**	**Outgoing**	**Radiated**	**Scattered**	**Outgoing**	**Radiated**	**Scattered**
1	0,0	0.978	1.000	0.027	0.86	0.00	146.65
	1,0	0.068	0.000	0.068	122.39	90.00	122.39
	2,0	1.178	0.000	1.178	320.33	180.00	320.33
2	0,0	0.968	1.000	0.069	3.55	0.00	119.79
	1,0	0.000	0.000	0.000	-64.99	90.00	-64.99
	2,0	1.214	0.000	1.214	358.34	180.00	358.34
3	0,0	0.978	1.000	0.027	0.86	0.00	146.65
	1,0	0.068	0.000	0.068	-57.61	90.00	-57.61
	2,0	1.178	0.000	1.178	320.33	180.00	320.33

Table 5.3: The normalized pressure coefficient of the linear array consisting of spherical three thin-shell transducers

N=3	*ka=1 f=605 Hz*	**Magnitude**			**Phase (degree)**		
Nu.	**Comp.**	**Outgoing**	**Radiated**	**Scattered**	**Outgoing**	**Radiated**	**Scattered**
1	0,0	0.855	1.000	0.159	4.05	0.00	157.66
	1,0	0.031	0.000	0.031	10.46	90.00	10.46
	2,0	0.090	0.104	0.014	176.26	174.59	343.96
2	0,0	0.918	1.000	0.466	27.73	0.00	113.70
	1,0	0.000	0.000	0.000	-76.86	90.00	-76.86
	2,0	0.090	0.104	0.039	196.55	174.59	296.36
3	0,0	0.855	1.000	0.159	4.06	0.00	157.60
	1,0	0.031	0.000	0.031	190.70	90.00	190.70
	2,0	0.090	0.104	0.014	176.27	174.59	343.86

Table 5.4: The normalized pressure coefficient of the linear array consisting of three ring-shell transducers

N=4	*ka=1 f=474 Hz*	**Magnitude**			**Phase (degree)**		
Nu.	**Comp.**	**Outgoing**	**Radiated**	**Scattered**	**Outgoing**	**Radiated**	**Scattered**
1	0,0	0.984	1.000	0.031	1.54	0.00	121.45
	1,0	0.080	0.000	0.080	104.79	90.00	104.79
	2,0	0.885	0.000	0.885	315.54	180.00	315.54
2	0,0	0.970	1.000	0.054	2.65	0.00	124.43
	1,0	0.029	0.000	0.029	18.92	90.00	18.92
	2,0	1.249	0.000	1.249	336.80	180.00	336.80
3	0,0	0.970	1.000	0.054	2.65	0.00	124.43
	1,0	0.029	0.000	0.029	198.92	90.00	198.92
	2,0	1.249	0.000	1.249	336.80	180.00	336.80
4	0,0	0.984	1.000	0.031	1.54	0.00	121.45
	1,0	0.080	0.000	0.080	-75.21	90.00	-75.21
	2,0	0.885	0.000	0.885	315.54	180.00	315.54

Table 5.5: The normalized pressure coefficient of the linear array consisting of four spherical thin-shell transducers

N=4	*ka=1 f=605 Hz*	**Magnitude**			**Phase (degree)**		
Nu.	**Comp.**	**Outgoing**	**Radiated**	**Scattered**	**Outgoing**	**Radiated**	**Scattered**
1	0,0	0.913	1.000	0.196	10.53	0.00	121.42
	1,0	0.042	0.000	0.042	-17.41	90.00	-17.41
	2,0	0.094	0.104	0.016	182.29	174.59	303.89
2	0,0	0.828	1.000	0.349	19.23	0.00	128.73
	1,0	0.032	0.000	0.032	146.43	90.00	146.43
	2,0	0.084	0.104	0.030	187.95	174.59	313.81
3	0,0	0.827	1.000	0.349	19.23	0.00	128.77
	1,0	0.032	0.000	0.032	-33.90	90.00	-33.90
	2,0	0.084	0.104	0.030	187.95	174.59	313.87
4	0,0	0.914	1.000	0.196	10.54	0.00	121.35
	1,0	0.042	0.000	0.042	162.81	90.00	162.81
	2,0	0.094	0.104	0.016	182.30	174.59	303.76

Table 5.6: The normalized pressure coefficient of the linear array consisting of four ring-shell transducers

N=8	*ka=1 f=474 Hz*	**Magnitude**			**Phase (degree)**		
Nu.	**Comp.**	**Outgoing**	**Radiated**	**Scattered**	**Outgoing**	**Radiated**	**Scattered**
1	0,0	0.980	1.000	0.032	1.44	0.00	129.79
	1,0	0.084	0.000	0.084	112.28	90.00	112.28
	2,0	1.033	0.000	1.033	324.51	180.00	324.51
2	0,0	0.968	1.000	0.058	2.83	0.00	125.04
	1,0	0.027	0.000	0.027	-22.51	90.00	-22.51
	2,0	1.259	0.000	1.259	345.11	180.00	345.11
3	0,0	0.974	1.000	0.045	2.15	0.00	126.20
	1,0	0.033	0.000	0.033	254.49	90.00	254.49
	2,0	1.118	0.000	1.118	329.58	180.00	329.58
4	0,0	0.985	1.000	0.039	2.08	0.00	113.39
	1,0	0.051	0.000	0.051	-75.03	90.00	-75.03
	2,0	0.769	0.000	0.769	305.41	180.00	305.41
5	0,0	0.985	1.000	0.039	2.08	0.00	113.39
	1,0	0.051	0.000	0.051	104.97	90.00	104.97
	2,0	0.769	0.000	0.769	305.41	180.00	305.41
6	0,0	0.974	1.000	0.045	2.15	0.00	126.20
	1,0	0.033	0.000	0.033	74.49	90.00	74.49
	2,0	1.118	0.000	1.118	329.58	180.00	329.58
7	0,0	0.968	1.000	0.058	2.83	0.00	125.04
	1,0	0.027	0.000	0.027	157.49	90.00	157.49
	2,0	1.259	0.000	1.259	345.11	180.00	345.11
8	0,0	0.980	1.000	0.032	1.44	0.00	129.79
	1,0	0.084	0.000	0.084	-67.72	90.00	-67.72
	2,0	1.033	0.000	1.033	324.51	180.00	324.51

Table 5.7: The normalized pressure coefficient of the linear array consisting of eight spherical thin-shell transducers

N=8	*ka=1 f=605 Hz*	**Magnitude**			**Phase (degree)**		
Nu.	**Comp.**	**Outgoing**	**Radiated**	**Scattered**	**Outgoing**	**Radiated**	**Scattered**
1	0,0	0.902	1.000	0.178	8.99	0.00	127.67
	1,0	0.039	0.000	0.039	-13.03	90.00	-13.03
	2,0	0.094	0.104	0.015	180.85	174.59	311.18
2	0,0	0.846	1.000	0.380	21.78	0.00	124.38
	1,0	0.024	0.000	0.024	145.83	90.00	145.83
	2,0	0.085	0.104	0.032	190.45	174.59	308.74
3	0,0	0.824	1.000	0.290	14.62	0.00	134.21
	1,0	0.020	0.000	0.020	-48.27	90.00	-48.27
	2,0	0.085	0.104	0.024	183.97	174.59	320.30
4	0,0	0.841	1.000	0.324	17.69	0.00	127.81
	1,0	0.017	0.000	0.017	125.19	90.00	125.19
	2,0	0.085	0.104	0.027	186.88	174.59	312.79
5	0,0	0.841	1.000	0.324	17.69	0.00	127.82
	1,0	0.018	0.000	0.018	-54.94	90.00	-54.94
	2,0	0.085	0.104	0.027	186.88	174.59	312.81
6	0,0	0.824	1.000	0.290	14.62	0.00	134.19
	1,0	0.019	0.000	0.019	131.84	90.00	131.84
	2,0	0.085	0.104	0.024	183.97	174.59	320.27
7	0,0	0.846	1.000	0.380	21.78	0.00	124.40
	1,0	0.025	0.000	0.025	-34.68	90.00	-34.68
	2,0	0.085	0.104	0.032	190.45	174.59	308.77
8	0,0	0.902	1.000	0.178	9.00	0.00	127.60
	1,0	0.039	0.000	0.039	167.19	90.00	167.19
	2,0	0.094	0.104	0.015	180.86	174.59	311.05

Table 5.8: The normalized pressure coefficient of the linear array consisting of eight ring-shell transducers

THIS PAGE INTENTIONALLY LEFT BLANK

CHAPTER 6:
Conclusion and Future Work

6.1 Conclusion

This thesis is the first successful practical demonstration of the T-matrix method applied to an active sonar array for which a finite-element model was employed to compute the scattering properties of a single transducer.

A piezoelectric thin spherical shell transducer and a class V flextensional transducer were modeled using the COMSOL Multiphysics computer code. Linear array models of the developed transducers were created using the T-matrix method.

Firstly, we modeled a radially polarized piezoelectric spherical thin-shell transducer. Validation of the model was done by comparing the computed values of the free-field radiated pressure amplitude against those of an approximate analytical model derived from an equivalent circuit model of the spherical transducer. The results agreed within 3.7 percent, which is acceptable for validation of the finite element code.

As a second transducer type, a class V flextensional ring-shell transducer was selected in part because data are available from a bi-planar billboard array tested in the 1990s [1]. The model of the ring-shell flextensional transducer was developed in COMSOL Multiphysics. Computed radiation characteristics are in excellent agreement with the manufacturer's data. The primary resonance frequency computed is only 0.8 percent lower than that of the manufacturer's data, and the second resonance computed is only 0.7 percent lower. The calculated source level (SL) for a 3000 Vrms drive for the primary resonance frequency was found to be 1.4 dB lower than the manufacturer's data at the primary resonance frequency and 3 dB higher than the manufacturer's data at the secondary resonance frequency. The bandwidth and the mechanical quality factor also show excellent agreement with the manufacturer's data.

After validation of the model, the scattering T-matrix and radiation coefficients of the developed model were computed through quadrupolar order using COMSOL for "*ka*" values equal to one. This same value was used in the T-matrix method to model the linear array.

Two linear array models were created. Beam patterns were computed for different configurations. The computed beam pattern results were compared against those using point source array theory.

The most significant differences were observed between the two solutions at end fire. This is expected because the T-matrix method incorporates the array interaction while the point source array theory does not. In particular, we observed that the nulls at end fire are not completed, and they are shadowed by scattering. The T- matrix method accounts for the inter-element array interaction and simulates the array performance more realistically than the point source array theory.

The T-matrix method can be used as a versatile tool in the design phase of an array with high-power active transducer elements. That is because the multi-interaction is accounted for in the methodology. The accuracy of the T-matrix method depends upon the finite-element model of the single transducer used to create the array. COMSOL Multiphysics produces a good model for a single transducer, thereby computing the scattering and radiation characteristics of arrays comprised of these transducers.

It should be noted, the developed finite element model was built for the common case *ka*=1. For higher *ka* values refinements should be made in the finite element model. Possible improvements were investigated for the ring-shell transducer in Chapter 4.4. When the Perfectly Matched Layer (PML) boundary condition was applied, the model performed better at frequencies higher than 1600 Hz in determining the SL.

6.1.1 Future Work

As a result of the research done on the T-matrix method application for array modeling, several other interesting topics for study have arisen.

In comparison to an approximate method, it is relatively easy to employ the T-matrix method in modeling active sonar array element interaction, and so this method should become the preferred method for active sonar array performance prediction. However, more practical examples are needed to demonstrate its applicability and superiority for an actual densely packed, high power active sonar array.

In order to test the accuracy of the T-matrix method, we are encouraged to develop an array model of the bi-planar array composed of 24 Sparton of Canada 600 Hz class flextensional ring-shell transducers that were tested in the 1990s and compare the data to our computed results using the T-matrix method.

As an alternative to computation of the mutual acoustic radiation with Pritchard's approximation, the development of a mutual acoustic radiation impedance using a T-matrix description can be carried out by future research in order to evaluate a projector's internal stress.

The accuracy of PML applied in the 3D finite element model can also be investigated for improving the performance of the 3D model at high frequencies.

THIS PAGE INTENTIONALLY LEFT BLANK

REFERENCES

[1] M. Werbicki, "NATO comparative test program 24-element class V flextensional-biplanar array report," Tech Memo 901108A, Naval Underwater Systems Center, New London, CT, June 1990.

[2] G. McMahon, "The ring-shell flextensional transducer (class V)," in *Proceedings of the International Workshop on Power Transducers for Sonics and Ultrasonics* (B. Hamonic, O. Wilson, and J. N. Decarpingny, eds.), pp. 60–74, Springer-Verlag, 1991.

[3] J. Adeff, "The three-element linear array expreriment data." February 2013.

[4] C. Sherman and J. Butler, *Transducers and Arrays for Underwater Sound*. Springer Science+Business, 2007.

[5] B. King and A. V. Buren, "A general addition theorem for spheroidal wave functions," *SIAM J.MATH.ANAL.*, vol. 4, pp. 149–153, February 1973.

[6] C. L. Scandrett and S. R. Baker, "T-matrix approach to array modeling," Technical Report NPS-UW-98-001, Naval Postgraduate School, Monterey, CA, June 1998.

[7] R. Pinto, "Three dimensional finite element model of a high power, low frequency ring-shell flextensional sonar transducer," Master's thesis, Naval Postgraduate School, Monterey, CA, January 1993.

[8] R. Richards, J. Blottman, and B. McTaggart, "Physics of array element interaction phenomena," in *Proceedings of the International Workshop on Power Transducers for Sonics and Ultrasonics* (O. W. B.F Hamonic and J. N. Decarpingny, eds.), pp. 86–108, Springer-Verlag, 1991.

[9] R. L. Pritchard, "Mutual acoustic impedance between radiators in an infinite rigid plane," *Journal of Acoustical Society of America*, vol. 32, pp. 730–737, 1960.

[10] L. E. Kinsler, A. B. C. A. R. Frey, and J. V. Sanders, *Fundamentals of Acoustics*. John Wiley and Sons, 4th ed., 2000.

[11] C. L. Scandrett and D. R. Canright, "Acoustic interactions in arrays of spherical elastic shells," *Journal of Acoustic Society of America*, vol. 90, pp. 589–595, July 1991.

[12] A. L. D. Ruiz, “Calculation of the transition matrix for the scattering of acoustic waves from a thin elastic spherical shell using the atila finite element code,” Master’s thesis, Naval Postgraduate School, Monterey, CA, March 1994.

[13] J. Day, “A modal approximation for the mutual radiation impedance for spherical sources and acoustic wave scattering using an improved atila finite element code,” Master’s thesis, Naval Postgraduate School, Monterey, CA, September 1999.

[14] K. Chuan, “Calculation of the transition matrix for the scattering of acoustic waves from a thin elastic spherical shell using the comsol multiphysics finite-element code,” Master’s thesis, Naval Postgraduate School, Monterey, CA, December 2011.

[15] M. Werbicki, “In-water tests of the sparton of Canada (SOC) class V flextensional transducer (single element configuration),” Tech Memo 901108A, Naval Underwater Systems Center, New London, CT, May 1990.

[16] G. McMahon and B. Armstrong, “A 10-kw ring-shell projector,” in *Progress in Underwater Acoustics* (H. M. Merklinger, ed.), pp. 647–650, Plenum Publishing Corp., 1987.

[17] COMSOL, *COMSOL Multiphysics User’s Guide*, version 4.3a ed., November 2012.

[18] COMSOL Multiphysics, *Acoustics Module User’s Guide Version*, 4.3a ed., October 2012.

[19] O. Wilson, *Introduction to Theory and Design of Sonar Transducers*. Peninsula Publishing Co., 1988.

[20] D. Berlincourt, D. Curran, and H. Jaffe, *Piezoelectric and Piezomagnetic Materials*, vol. I.,Part A, ch. 3. Academic Press, N.Y, 1964.

[21] K. F. Riley, M. P. Hobson, and S. Bence, *Mathematical Methods for Physics and Engineering*. Cambridge University Press, N.Y, 3th ed., 2006.

[22] M. Abramowitz and I. Stegun, *Handbook of Mathematical Functions*. Dover Publications,Inc.NY, 1972.

[23] R. Timme, A. Young, and J. Blue, “Transducer needs for low-frequency sonar,” in *Proceedings of the International Workshop on Power Transducers for Sonics and Ultrasonics* (a. O. W. B.F Hamonic and J. N. Decarpingny, eds.), pp. 3–13, Springer-Verlag, June 1991.

[24] J. Blottman, “Sparton ring-shell single element modeling,” Technical Memorandum 89-1090, NUWC, New London Laboratory, June 1989.

[25] COMSOL Multiphysics, *Introduction to Acoustics Module*, 4.3a ed., May 2012.

[26] M. C. Junger and D. Feit, *Sound, Structures, and Their Interaction*. Massachusetts Institute of Technology, 2th ed., 1986.

THIS PAGE INTENTIONALLY LEFT BLANK

APPENDIX A:

Transforming the Elasto-Piezoelectric Property Matrix to Model a Circumferentially-Polarized Ring as Radially-Polarized

The elasto-piezoelectric property matrix for a piezoelectric ceramic, taking stress T and electric field E as independent, is

$$\begin{bmatrix} S_1 \\ S_2 \\ S_3 \\ S_4 \\ S_5 \\ S_6 \\ D_1 \\ D_2 \\ D_3 \end{bmatrix} = \left[\begin{array}{ccc|ccc|ccc} s_{11}^E & s_{12}^E & s_{13}^E & 0 & 0 & 0 & 0 & 0 & d_{31} \\ s_{12}^E & s_{11}^E & s_{13}^E & 0 & 0 & 0 & 0 & 0 & d_{31} \\ s_{13}^E & s_{13}^E & s_{33}^E & 0 & 0 & 0 & 0 & 0 & d_{33} \\ \hline 0 & 0 & 0 & s_{44}^E & 0 & 0 & 0 & d_{15} & 0 \\ 0 & 0 & 0 & 0 & s_{44}^E & 0 & d_{15} & 0 & 0 \\ 0 & 0 & 0 & 0 & 0 & s_{66}^E & 0 & 0 & 0 \\ \hline 0 & 0 & 0 & 0 & d_{15} & 0 & \varepsilon_{11}^T & 0 & 0 \\ 0 & 0 & 0 & d_{15} & 0 & 0 & 0 & \varepsilon_{11}^T & 0 \\ d_{31} & d_{31} & d_{33} & 0 & 0 & 0 & 0 & 0 & \varepsilon_{33}^T \end{array}\right] \begin{bmatrix} T_1 \\ T_2 \\ T_3 \\ T_4 \\ T_5 \\ T_6 \\ E_1 \\ E_2 \\ E_3 \end{bmatrix} \tag{A.1}$$

In a circumferentially-polarized ring for a right-handed coordinate basis set, $z = 1$, $r = 2$, and $\phi = 3$ (axial,radial,circumferential, respectively). Then, denoting l for longitudinal, s for shear,

$$\begin{bmatrix} S_1 = S_{lz} \\ S_2 = S_{lr} \\ S_3 = S_{l\phi} \\ S_4 = S_{sz} \\ S_5 = S_{sr} \\ S_6 = S_{s\phi} \\ D_1 = D_z \\ D_2 = D_r \\ D_3 = D_\phi \end{bmatrix} = \left[\begin{array}{ccc|ccc|ccc} s_{11}^E & s_{12}^E & s_{13}^E & 0 & 0 & 0 & 0 & 0 & d_{31} \\ s_{12}^E & s_{11}^E & s_{13}^E & 0 & 0 & 0 & 0 & 0 & d_{31} \\ s_{13}^E & s_{13}^E & s_{33}^E & 0 & 0 & 0 & 0 & 0 & d_{33} \\ \hline 0 & 0 & 0 & s_{44}^E & 0 & 0 & 0 & d_{15} & 0 \\ 0 & 0 & 0 & 0 & s_{44}^E & 0 & d_{15} & 0 & 0 \\ 0 & 0 & 0 & 0 & 0 & s_{66}^E & 0 & 0 & 0 \\ \hline 0 & 0 & 0 & 0 & d_{15} & 0 & \varepsilon_{11}^T & 0 & 0 \\ 0 & 0 & 0 & d_{15} & 0 & 0 & 0 & \varepsilon_{11}^T & 0 \\ d_{31} & d_{31} & d_{33} & 0 & 0 & 0 & 0 & 0 & \varepsilon_{33}^T \end{array}\right] \begin{bmatrix} T_1 = T_{lz} \\ T_2 = T_{lr} \\ T_3 = T_{l\phi} \\ T_4 = T_{sz} \\ T_5 = T_{sr} \\ T_6 = T_{s\phi} \\ E_1 = E_z \\ E_2 = E_r \\ E_3 = E_\phi \end{bmatrix} \tag{A.2}$$

Now, suppose we want to model this ring as radially polarized, while trying to keep its elastic and dielectric matrix as follows.

Exchange the last two rows and columns (i.e., 8 and 9)

$$\begin{bmatrix} S_1 = S_{lz} \\ S_2 = S_{lr} \\ S_3 = S_{l\phi} \\ S_4 = S_{sz} \\ S_5 = S_{sr} \\ S_6 = S_{s\phi} \\ D_1 = D_z \\ D_2 = D_r \\ D_3 = D_\phi \end{bmatrix} = \left[\begin{array}{ccc|ccc|ccc} s_{11}^E & s_{12}^E & s_{13}^E & 0 & 0 & 0 & 0 & d_{31} & 0 \\ s_{12}^E & s_{11}^E & s_{13}^E & 0 & 0 & 0 & 0 & d_{31} & 0 \\ s_{13}^E & s_{13}^E & s_{33}^E & 0 & 0 & 0 & 0 & d_{33} & 0 \\ \hline 0 & 0 & 0 & s_{44}^E & 0 & 0 & 0 & 0 & d_{15} \\ 0 & 0 & 0 & 0 & s_{44}^E & 0 & d_{15} & 0 & 0 \\ 0 & 0 & 0 & 0 & 0 & s_{66}^E & 0 & 0 & 0 \\ \hline 0 & 0 & 0 & 0 & d_{15} & 0 & \varepsilon_{11}^T & 0 & 0 \\ d_{31} & d_{31} & d_{33} & 0 & 0 & 0 & 0 & \varepsilon_{33}^T & 0 \\ 0 & 0 & 0 & d_{15} & 0 & 0 & 0 & 0 & \varepsilon_{11}^T \end{array}\right] \begin{bmatrix} T_1 = T_{lz} \\ T_2 = T_{lr} \\ T_3 = T_{l\phi} \\ T_4 = T_{sz} \\ T_5 = T_{sr} \\ T_6 = T_{s\phi} \\ E_1 = E_z \\ E_2 = E_r \\ E_3 = E_\phi \end{bmatrix} \tag{A.3}$$

Change the correspondence of the matrix indices with coordinate directions to identify the new polarization direction as the "3" direction ($\phi = 2, r = 3$). Exchanges rows and columns 2 and 3, 5 and 6, and 8 and 9

$$\begin{bmatrix} S_1 = S_{lz} \\ S_2 = S_{l\phi} \\ S_3 = S_{lr} \\ S_4 = S_{sz} \\ S_5 = S_{s\phi} \\ S_6 = S_{sr} \\ D_1 = D_z \\ D_2 = D_\phi \\ D_3 = D_r \end{bmatrix} = \left[\begin{array}{ccc|ccc|ccc} s_{11}^E & s_{13}^E & s_{12}^E & 0 & 0 & 0 & 0 & 0 & d_{31} \\ s_{13}^E & s_{33}^E & s_{13}^E & 0 & 0 & 0 & 0 & 0 & d_{33} \\ s_{12}^E & s_{13}^E & s_{11}^E & 0 & 0 & 0 & 0 & 0 & d_{31} \\ \hline 0 & 0 & 0 & s_{44}^E & 0 & 0 & 0 & d_{15} & 0 \\ 0 & 0 & 0 & 0 & s_{66}^E & 0 & 0 & 0 & 0 \\ \hline 0 & 0 & 0 & 0 & 0 & s_{44}^E & d_{15} & 0 & 0 \\ 0 & 0 & 0 & 0 & 0 & d_{15} & \varepsilon_{11}^T & 0 & 0 \\ 0 & 0 & 0 & d_{15} & 0 & 0 & 0 & \varepsilon_{11}^T & 0 \\ d_{31} & d_{33} & d_{31} & 0 & 0 & 0 & 0 & 0 & \varepsilon_{33}^T \end{array}\right] \begin{bmatrix} T_1 = T_{lz} \\ T_2 = T_{l\phi} \\ T_3 = T_{lr} \\ T_4 = T_{sz} \\ T_5 = T_{s\phi} \\ T_6 = T_{sr} \\ E_1 = E_z \\ E_2 = E_\phi \\ E_3 = E_r \end{bmatrix} \tag{A.4}$$

The final form is not expected to depend upon whether the transformed polarization direction is chosen, r or z. To prove this, we follow the same procedure as above, now exchanging ϕ for the z polarization direction. We exchange rows and columns (7 and 9).

$$\begin{bmatrix} S_1 = S_{lz} \\ S_2 = S_{lr} \\ S_3 = S_{l\phi} \\ S_4 = S_{sz} \\ S_5 = S_{sr} \\ S_6 = S_{s\phi} \\ D_1 = D_z \\ D_2 = D_r \\ D_3 = D_\phi \end{bmatrix} = \left[\begin{array}{ccc|ccc|ccc} s_{11}^E & s_{12}^E & s_{13}^E & 0 & 0 & 0 & d_{31} & 0 & 0 \\ s_{12}^E & s_{11}^E & s_{13}^E & 0 & 0 & 0 & d_{31} & 0 & 0 \\ s_{13}^E & s_{13}^E & s_{33}^E & 0 & 0 & 0 & d_{33} & 0 & 0 \\ \hline 0 & 0 & 0 & s_{44}^E & 0 & 0 & 0 & d_{15} & 0 \\ 0 & 0 & 0 & 0 & s_{44}^E & 0 & 0 & 0 & d_{15} \\ 0 & 0 & 0 & 0 & 0 & s_{66}^E & 0 & 0 & 0 \\ \hline d_{31} & d_{31} & d_{33} & 0 & 0 & 0 & \varepsilon_{33}^T & 0 & 0 \\ 0 & 0 & 0 & d_{15} & 0 & 0 & 0 & \varepsilon_{11}^T & 0 \\ 0 & 0 & 0 & 0 & d_{15} & 0 & 0 & 0 & \varepsilon_{11}^T \end{array}\right] \begin{bmatrix} T_1 = T_{lz} \\ T_2 = T_{lr} \\ T_3 = T_{l\phi} \\ T_4 = T_{sz} \\ T_5 = T_{sr} \\ T_6 = T_{s\phi} \\ E_1 = E_z \\ E_2 = E_r \\ E_3 = E_\phi \end{bmatrix} \tag{A.5}$$

We change the correspondence of matrix indices with coordinate directions to identify the new polarization direction as the “3” direction (we now assigning $\phi = 1$, $z = 3$)

$$\begin{bmatrix} S_3 = S_{lz} \\ S_2 = S_{lr} \\ S_1 = S_{l\phi} \\ S_4 = S_{sz} \\ S_5 = S_{sr} \\ S_6 = S_{s\phi} \\ D_3 = D_z \\ D_2 = D_r \\ D_1 = D_\phi \end{bmatrix} = \left[\begin{array}{ccc|ccc|ccc} s_{11}^E & s_{12}^E & s_{13}^E & 0 & 0 & 0 & d_{31} & 0 & 0 \\ s_{12}^E & s_{11}^E & s_{13}^E & 0 & 0 & 0 & d_{31} & 0 & 0 \\ s_{13}^E & s_{13}^E & s_{33}^E & 0 & 0 & 0 & d_{33} & 0 & 0 \\ \hline 0 & 0 & 0 & s_{44}^E & 0 & 0 & 0 & d_{15} & 0 \\ 0 & 0 & 0 & 0 & s_{44}^E & 0 & 0 & 0 & d_{15} \\ 0 & 0 & 0 & 0 & 0 & s_{66}^E & 0 & 0 & 0 \\ \hline d_{31} & d_{31} & d_{33} & 0 & 0 & 0 & \varepsilon_{33}^T & 0 & 0 \\ 0 & 0 & 0 & d_{15} & 0 & 0 & 0 & \varepsilon_{11}^T & 0 \\ 0 & 0 & 0 & 0 & d_{15} & 0 & 0 & 0 & \varepsilon_{11}^T \end{array}\right] \begin{bmatrix} T_3 = T_{lz} \\ T_2 = T_{lr} \\ T_1 = T_{l\phi} \\ T_6 = T_{sz} \\ T_5 = T_{sr} \\ T_4 = T_{s\phi} \\ E_3 = E_z \\ E_2 = E_r \\ E_1 = E_\phi \end{bmatrix} \tag{A.6}$$

We exchange rows and columns 1 and 3, 4 and 6, 7 and 9 to put them in regular order:

$$\begin{bmatrix} S_1 = S_{l\phi} \\ S_2 = S_{lr} \\ S_3 = S_{lz} \\ S_6 = S_{s\phi} \\ S_5 = S_{sr} \\ S_4 = S_{sz} \\ D_1 = D_{\phi} \\ D_2 = D_r \\ D_3 = D_z \end{bmatrix} = \left[\begin{array}{ccc|ccc|ccc} s_{33}^E & s_{13}^E & s_{13}^E & 0 & 0 & 0 & 0 & 0 & d_{33} \\ s_{13}^E & s_{11}^E & s_{12}^E & 0 & 0 & 0 & 0 & 0 & d_{31} \\ s_{13}^E & s_{12}^E & s_{11}^E & 0 & 0 & 0 & 0 & 0 & d_{31} \\ \hline 0 & 0 & 0 & s_{66}^E & 0 & 0 & 0 & 0 & 0 \\ 0 & 0 & 0 & 0 & s_{44}^E & 0 & d_{15} & 0 & 0 \\ 0 & 0 & 0 & 0 & 0 & s_{44}^E & 0 & d_{15} & 0 \\ \hline 0 & 0 & 0 & 0 & d_{15} & 0 & \varepsilon_{11}^T & 0 & 0 \\ 0 & 0 & 0 & 0 & 0 & d_{15} & 0 & \varepsilon_{11}^T & 0 \\ d_{33} & d_{31} & d_{31} & 0 & 0 & 0 & 0 & 0 & \varepsilon_{33}^T \end{array}\right] \begin{bmatrix} T_1 = T_{l\phi} \\ T_2 = T_{lr} \\ T_3 = T_{lz} \\ T_4 = T_{s\phi} \\ T_5 = T_{sr} \\ T_6 = T_{sz} \\ E_1 = E_{\phi} \\ E_2 = E_r \\ E_3 = E_z \end{bmatrix} \tag{A.7}$$

An alternative procedure to transform the electrical coupling is as follows. Instead of exchanging rows and columns, permute them. Permuting the polarization direction to “r” (i.e., the “2” direction):

$$\begin{bmatrix} S_1 = S_{lz} \\ S_2 = S_{lr} \\ S_3 = S_{l\phi} \\ S_4 = S_{sz} \\ S_5 = S_{sr} \\ S_6 = S_{s\phi} \\ D_1 = D_z \\ D_2 = D_r \\ D_3 = D_{\phi} \end{bmatrix} = \left[\begin{array}{ccc|ccc|ccc} s_{11}^E & s_{12}^E & s_{13}^E & 0 & 0 & 0 & 0 & d_{31} & 0 \\ s_{12}^E & s_{11}^E & s_{13}^E & 0 & 0 & 0 & 0 & d_{31} & 0 \\ s_{13}^E & s_{13}^E & s_{33}^E & 0 & 0 & 0 & 0 & d_{33} & 0 \\ \hline 0 & 0 & 0 & s_{44}^E & 0 & 0 & d_{15} & 0 & 0 \\ 0 & 0 & 0 & 0 & s_{44}^E & 0 & 0 & 0 & d_{15} \\ 0 & 0 & 0 & 0 & 0 & s_{66}^E & 0 & 0 & 0 \\ \hline 0 & 0 & 0 & d_{15} & 0 & 0 & \varepsilon_{11}^T & 0 & 0 \\ d_{31} & d_{31} & d_{33} & 0 & 0 & 0 & 0 & \varepsilon_{11}^T & 0 \\ 0 & 0 & 0 & 0 & d_{15} & 0 & 0 & 0 & \varepsilon_{33}^T \end{array}\right] \begin{bmatrix} T_1 = T_{lz} \\ T_2 = T_{lr} \\ T_3 = T_{l\phi} \\ T_4 = T_{sz} \\ T_5 = T_{sr} \\ T_6 = T_{s\phi} \\ E_1 = E_z \\ E_2 = E_r \\ E_3 = E_{\phi} \end{bmatrix} \tag{A.8}$$

Now, reidentify coordinate directions and matrix subscripts:

$$\begin{bmatrix} S_2 = S_{lz} \\ S_3 = S_{lr} \\ S_1 = S_{l\phi} \\ S_5 = S_{sz} \\ S_6 = S_{sr} \\ S_4 = S_{s\phi} \\ D_2 = D_z \\ D_3 = D_r \\ D_1 = D_\phi \end{bmatrix} = \left[\begin{array}{ccc|ccc|ccc} s_{11}^E & s_{12}^E & s_{13}^E & 0 & 0 & 0 & 0 & d_{31} & 0 \\ s_{12}^E & s_{11}^E & s_{13}^E & 0 & 0 & 0 & 0 & d_{31} & 0 \\ s_{13}^E & s_{13}^E & s_{33}^E & 0 & 0 & 0 & 0 & d_{33} & 0 \\ \hline 0 & 0 & 0 & s_{44}^E & 0 & 0 & d_{15} & 0 & 0 \\ 0 & 0 & 0 & 0 & s_{44}^E & 0 & 0 & 0 & d_{15} \\ 0 & 0 & 0 & 0 & 0 & s_{66}^E & 0 & 0 & 0 \\ \hline 0 & 0 & 0 & d_{15} & 0 & 0 & \varepsilon_{11}^T & 0 & 0 \\ d_{31} & d_{31} & d_{33} & 0 & 0 & 0 & 0 & \varepsilon_{11}^T & 0 \\ 0 & 0 & 0 & 0 & d_{15} & 0 & 0 & 0 & \varepsilon_{33}^T \end{array}\right] \begin{bmatrix} T_2 = T_{lz} \\ T_3 = T_{lr} \\ T_1 = T_{l\phi} \\ T_5 = T_{sz} \\ T_6 = T_{sr} \\ T_4 = T_{s\phi} \\ E_2 = E_z \\ E_3 = E_r \\ E_1 = E_\phi \end{bmatrix} \tag{A.9}$$

Now, put the matrix in regular order:

$$\begin{bmatrix} S_1 = S_{l\phi} \\ S_2 = S_{lz} \\ S_3 = S_{lr} \\ S_4 = S_{s\phi} \\ S_5 = S_{sz} \\ S_6 = S_{sr} \\ D_1 = D_\phi \\ D_2 = D_z \\ D_3 = D_r \end{bmatrix} = \left[\begin{array}{ccc|ccc|ccc} s_{33}^E & s_{13}^E & s_{12}^E & 0 & 0 & 0 & 0 & 0 & d_{33} \\ s_{13}^E & s_{11}^E & s_{13}^E & 0 & 0 & 0 & 0 & 0 & d_{31} \\ s_{12}^E & s_{13}^E & s_{11}^E & 0 & 0 & 0 & 0 & 0 & d_{31} \\ \hline 0 & 0 & 0 & s_{66}^E & 0 & 0 & 0 & 0 & 0 \\ 0 & 0 & 0 & 0 & s_{44}^E & 0 & 0 & d_{15} & 0 \\ 0 & 0 & 0 & 0 & 0 & s_{44}^E & d_{15} & 0 & 0 \\ \hline 0 & 0 & 0 & 0 & 0 & d_{15} & \varepsilon_{11}^T & 0 & 0 \\ 0 & 0 & 0 & 0 & d_{15} & 0 & 0 & \varepsilon_{11}^T & 0 \\ d_{33} & d_{31} & d_{31} & 0 & 0 & 0 & 0 & 0 & \varepsilon_{33}^T \end{array}\right] \begin{bmatrix} T_1 = T_{l\phi} \\ T_2 = T_{lz} \\ T_3 = T_{lr} \\ T_4 = T_{s\phi} \\ T_5 = T_{sz} \\ T_6 = T_{sr} \\ E_1 = E_\phi \\ E_2 = E_z \\ E_3 = E_r \end{bmatrix} \tag{A.10}$$

Following the permutation procedure, now make “z” the polarization direction:

$$\begin{bmatrix} S_1 = S_{lz} \\ S_2 = S_{lr} \\ S_3 = S_{l\phi} \\ S_4 = S_{sz} \\ S_5 = S_{sr} \\ S_6 = S_{s\phi} \\ D_1 = D_z \\ D_2 = D_r \\ D_3 = D_\phi \end{bmatrix} = \left[\begin{array}{ccc|ccc|ccc} s_{11}^E & s_{12}^E & s_{13}^E & 0 & 0 & 0 & d_{31} & 0 & 0 \\ s_{12}^E & s_{11}^E & s_{13}^E & 0 & 0 & 0 & d_{31} & 0 & 0 \\ s_{13}^E & s_{13}^E & s_{33}^E & 0 & 0 & 0 & d_{33} & 0 & 0 \\ \hline 0 & 0 & 0 & s_{44}^E & 0 & 0 & 0 & 0 & d_{15} \\ 0 & 0 & 0 & 0 & s_{44}^E & 0 & 0 & d_{15} & 0 \\ 0 & 0 & 0 & 0 & 0 & s_{66}^E & 0 & 0 & 0 \\ \hline d_{31} & d_{31} & d_{33} & 0 & 0 & 0 & \varepsilon_{33}^T & 0 & 0 \\ 0 & 0 & 0 & 0 & d_{15} & 0 & 0 & \varepsilon_{11}^T & 0 \\ 0 & 0 & 0 & d_{15} & 0 & 0 & 0 & 0 & \varepsilon_{11}^T \end{array}\right] \begin{bmatrix} T_1 = T_{lz} \\ T_2 = T_{lr} \\ T_3 = T_{l\phi} \\ T_4 = T_{sz} \\ T_5 = T_{sr} \\ T_6 = T_{s\phi} \\ E_1 = E_z \\ E_2 = E_r \\ E_3 = E_\phi \end{bmatrix} \tag{A.11}$$

Now, reidentify coordinate directions and matrix subscripts:

$$\begin{bmatrix} S_3 = S_{lz} \\ S_1 = S_{lr} \\ S_2 = S_{l\phi} \\ S_6 = S_{sz} \\ S_4 = S_{sr} \\ S_5 = S_{s\phi} \\ D_3 = D_z \\ D_1 = D_r \\ D_2 = D_\phi \end{bmatrix} = \left[\begin{array}{ccc|ccc|ccc} s_{11}^E & s_{12}^E & s_{13}^E & 0 & 0 & 0 & d_{31} & 0 & 0 \\ s_{12}^E & s_{11}^E & s_{13}^E & 0 & 0 & 0 & d_{31} & 0 & 0 \\ s_{13}^E & s_{13}^E & s_{33}^E & 0 & 0 & 0 & d_{33} & 0 & 0 \\ \hline 0 & 0 & 0 & s_{44}^E & 0 & 0 & 0 & 0 & d_{15} \\ 0 & 0 & 0 & 0 & s_{44}^E & 0 & 0 & d_{15} & 0 \\ 0 & 0 & 0 & 0 & 0 & s_{66}^E & 0 & 0 & 0 \\ \hline d_{31} & d_{31} & d_{33} & 0 & 0 & 0 & \varepsilon_{33}^T & 0 & 0 \\ 0 & 0 & 0 & 0 & d_{15} & 0 & 0 & \varepsilon_{11}^T & 0 \\ 0 & 0 & 0 & d_{15} & 0 & 0 & 0 & 0 & \varepsilon_{11}^T \end{array}\right] \begin{bmatrix} T_3 = T_{lz} \\ T_1 = T_{lr} \\ T_2 = T_{l\phi} \\ T_6 = T_{sz} \\ T_4 = T_{sr} \\ T_5 = T_{s\phi} \\ E_3 = E_z \\ E_1 = E_r \\ E_2 = E_\phi \end{bmatrix} \tag{A.12}$$

Now put in regular order:

$$\begin{bmatrix} S_1 = S_{lr} \\ S_2 = S_{l\phi} \\ S_3 = S_{lz} \\ S_4 = S_{sr} \\ S_5 = S_{s\phi} \\ S_6 = S_{sz} \\ D_1 = D_r \\ D_2 = D_\phi \\ D_3 = D_z \end{bmatrix} = \left[\begin{array}{ccc|ccc|ccc} s_{11}^E & s_{13}^E & s_{12}^E & 0 & 0 & 0 & 0 & 0 & d_{31} \\ s_{13}^E & s_{33}^E & s_{13}^E & 0 & 0 & 0 & 0 & 0 & d_{33} \\ s_{12}^E & s_{13}^E & s_{11}^E & 0 & 0 & 0 & 0 & 0 & d_{31} \\ \hline 0 & 0 & 0 & s_{44}^E & 0 & 0 & d_{15} & 0 & 0 \\ 0 & 0 & 0 & 0 & s_{66}^E & 0 & 0 & 0 & 0 \\ 0 & 0 & 0 & 0 & 0 & s_{44}^E & 0 & d_{15} & 0 \\ \hline 0 & 0 & 0 & d_{15} & 0 & 0 & \varepsilon_{11}^T & 0 & 0 \\ 0 & 0 & 0 & 0 & 0 & d_{15} & 0 & \varepsilon_{11}^T & 0 \\ d_{33} & d_{31} & d_{31} & 0 & 0 & 0 & 0 & 0 & \varepsilon_{33}^T \end{array}\right] \begin{bmatrix} T_1 = T_{lr} \\ T_2 = T_{l\phi} \\ T_3 = T_{lz} \\ T_4 = T_{sr} \\ T_5 = T_{s\phi} \\ T_6 = T_{sz} \\ E_1 = E_r \\ E_2 = E_\phi \\ E_3 = E_z \end{bmatrix} \tag{A.13}$$

THIS PAGE INTENTIONALLY LEFT BLANK

APPENDIX B:

Main Code

```
 %case: arbitrary number of element on the Z(polar) axis
clear all
clc
element=[2];
distance=[2];
for num1=1:length(element)
for num2=1:length(distance)
clearvars -except element distance num1 num2
clc
mode=2; % total number of mode
K2=(mode+1)^2; % monopole,dipole, quadrupole
% Parameter are adjusted for ka=1
radius=0.4; %radius of ring-shell [m]
c=1490; %speed of sound [m/s]
f=605;
lambda=c/f; %wavelength [m]
k=2*pi/lambda; %wave number
ka=k*radius; % ka=1.0
d=lambda/distance(num2); %distance between the projector
kd=k*d;
%write transducer location for line array
N=element(num1); %number of projector
%check the number of element whether odd or even number
if mod(N,2)==0 %if it is even the spacing along the z axis would
p=-N/2:N/2-1;
z=(p*d)+d/2; %transducer located through axes(x,y,z)
else
p =-(N-1)/2:1:(N-1)/2;
z=p*d; %transducer located through axes(x,y,z)
end
```

```
%other axis would be zero for linear array
x=zeros(1,N);
y=zeros(1,N);
position=[x' y' z'];
%calculate the relative angle for each transducer
for var1=1:N
for var2=1:N
delta_x=0;
delta_y=0;
delta_z=z(var1)-z(var2);
r=sqrt(delta_x.^2+delta_y.^2+delta_z.^2);
theta(var1,var2)=acos(delta_z/r);
phi(var1,var2)=atan2(delta_x,delta_y);
end;
end;
%Set the diagonal angles zeros(i.e theta11,theta22,theta33...)
theta(1:N+1:N*N)=0;
%% Computation of translation Matrix Gij for transducer elements
% the modes of radiated transducer called as r,m and the modes of the transducer
% where the radiated pressure defined as incoming pressure reference with
% it's origin called as s,u.
alfa=zeros(K2*N);
for sph_m=1:N %main ring-shell
for sph_r=1:N %relative ring-shell
kr12=abs(sph_m-sph_r)*kd;
count2=0;
for r=0:mode %2nd ring-shell modes r,m
for m=-r:r
count2=1+count2; %index of Gij matrix column
count1=0; %index of Gij matrix row
for s=0:mode %1th ring-shell modes s,u
for u=-s:s
count1=count1+1;
%define the lower limit of summation
```

```
t0=abs(r-s);
t1=abs(m-u);
if t1>t0
if mod((t1-t0),2)==0
t0=t1;
else
t0=t1+1;
end;
end;
count3=1;
clear Gtemp3
for t=t0:2:s+r
%Van Buren's paper used for defining the a
%coeffcient and named this function as "a".
Gtemp1=a(s,t,r,u,m)*shank2(t,kr12);
%spherical harmonic function calculate sph.
%harmonic
M=m-u; %order of Spherical Harmonic
Gtemp2=sphericalharmonic(t,M,theta(sph_m,sph_r),phi(sph_m,sph_r));
%Multiplication of defined spherical harmonic,a
%coeff and sph. hankel.
Gtemp3(1,count3)=Gtemp1*Gtemp2;
%increase the count3 t create a Btemp1c
%vector.
count3=count3+1;
end;
%the translation matrix which showed the outgoing wavw
%from 2 sphere as a incominwave to 1 sphere.
if kr12==0
G(count1,count2)=0;
else
G(count1,count2)=sum(Gtemp3);
end;
end;
```

```
end;
count1=1;
end;
end;
%locate the product matrix(T-matrix and Gij) as a submatrix into Alfo matrix
load('Tmatrix_ring.mat') %T-MAtrix computed by the help of COMSOL
pos1a=(1+length(G)*(sph_r-1));
pos1b=(length(G)+length(G)*(sph_r-1));
pos2a=1+length(G)*(sph_m-1);
pos2b=(length(G)+length(G)*(sph_m-1));
if sph_r-sph_m==0
alfa(pos2a:pos2b,pos1a:pos1b)=zeros(length(Tmatrix));
else
alfa(pos2a:pos2b,pos1a:pos1b)=Tmatrix*G;
end;
end;
end;
%% Calculate Beam Pattern
clearvars -except alfa N position element distance lambda d k mode num1 num2
load('Radiated Pressure Amplitude_ring1V.mat') %Radiated pressure computed by the help of
COMSOL
Pr=repmat(P_radiated,N,1); %repeat the vector for the specified mode for each projector
%% DEFINE SCATTER VECTOR
%express in matrix form A*P_s=B
%A : I-Alfa and B: Free Radiated Pressure multiply alfa
A=eye(length(alfa))-alfa;
B=alfa*Pr;
%Solution for P_s
P_s=A\B;
%% Total Pressure Computation
%Point position,spherical coordinate system according to the top transducer
sample=30;
phi=linspace(0,pi,sample);% degree
%convert radian
```

```
theta=linspace(0,pi,sample);
%define the position vectors and unit vectors
position=position’;
%Summation
for ind2=1:length(theta)
rhat=[cos(phi).*sin(theta(ind2));sin(theta(ind2)).*sin(phi);cos(theta(ind2)).*ones(1,length(phi))];
for ind1=1:length(phi)
Ptotal=0;
count=0;
for proj=1:N %number of projector
Ptempb=0;
for n=0:mode
Ptempa=0;
for m=-n:n
count=count+1;
%Spherical Harmonic Function changed,because theta is not scalar
%anymore
Ptempa=Ptempa+(Pr(count)+P_s(count))*sphericalharmonic(n,m,theta(ind2),phi(ind1)); % total Pressure
end
Ptempb=Ptempb+Ptempa*(1i)^(n+1); % total Pressure
end
Ptotal=Ptotal+Ptempb.*exp(1i.*k.*(position(1,proj).*rhat(1,ind1)...
+position(2,proj).*rhat(2,ind1)+position(3,proj).*rhat(3,ind1)));
end
Ptotal1(ind1,ind2)=Ptotal;
end;
%Find the beam pattern
end;
%normalization
H=Ptotal1/abs(max(max(Ptotal1))); % the max function takes the magnitude of the complex value
b=20*log10(abs(H)); %Beam Pattern in dB
shift=50;
```

```
b =b+shift;
b(find(b<0)) = 0;
%% Plots of Results
x = (b.*(cos(phi)'*sin(theta)));
y = (b.*(sin(phi)'*sin(theta)));
z = b.*repmat(cos(theta),sample,1);
x1 =-(b.*(cos(phi)'*sin(theta)));
y1 =-(b.*(sin(phi)'*sin(theta)));
z1 =b.*repmat(cos(theta),sample,1);
%For convenience in linear Plot convert the angle unit from radian to degree
phi_d=phi*180/pi;
figure1=figure
axis equal
set(gca,'FontSize',12)
surf(x,y,z,b)
hold on
surf(x1,y1,z1,b)
axis square; camlight headlight;
set(gca,'box','off');
set(gca,'xtick',[],'ytick',[],'ztick',[]);
xlabel('')
ylabel('')
zlabel('ARRAY AXIS','FontSize',18)
title(['3D Far Field Beam Pattern of Linear Array,ka=1, N=',num2str(N)...
,' and d = \lambda/',num2str(distance(num2))],'FontSize',15)
screen=get(0,'ScreenSize');
end;
end;
```

B.1 Code of the Used Functions

The following code was used in the main code they are written by Joseph L. Day [13]

shank2

```
function hn=shank2(n,x)
% Computes the Spherical Hankel function of the second kind
% Written by Joseph L. Day

hn=sqrt(pi/(2*x))*besselh(n+.5,2,x);
```

B.1.1 jprime

```
 function jp=jprime(n,x)
% Computes the first derivative of the Spherical Bessel function.
% Written by Joseph L. Day

jp=sqrt(pi/(2*x))*(besselj(n-.5,x)-(n+1)*besselj(n+.5,x)/(x));
```

B.1.2 fact

```
 function y=fact(n)

% Computes the factorial of n
% Written by Joseph L. Day

y=prod(1:n) ;
```

B.1.3 bc

```
 function y=bc(n,m)

% Computes the binomial coefficient
% Written by Joseph L. Day
```

```
if m<0
y=0;
e1seif n-m<0
y=0;
else
y=prod(1:n)/(prod(1:m)*prod(1:n-m));
end
```

B.1.4 a

```
 function A=a(s,t,r,u,m)

% computes the function a(s,t,r,u,m) of the Addition Theorem
% as written in King and Van Buren

num1=(2*s+1)*(2*t+1)*fact(s-u)*fact(t-m+u)*fact(r+m)*fact((s+t+r)/2);
dem1=fact((r+t-s)/2)*fact((r+s-t)/2)* fact((s+t-r)/2)*fact(s+t+r+1);
term1=num1/dem1;
wmin=max([r-s-t,s-r-t-2*m+2*u,t-s-r+2*u])/2;
wmax=min([s+t-r,r+t-s-2*m+2*u,r+s-t+2*u])/2;
sum=0;

for w=wmin:wmax
sum=sum+(-1)^w*bc(s+t-r,(s+t-r)/2+w)*...
bc(t+r-s,(t+r-s)/2+m-u+w)*bc(s+r-t,(s+r-t)/2-u+w);
end

A=(i^(s+t-r))*term1*sum;
```

Initial Distribution List

1. Defense Technical Information Center
   Ft. Belvoir, Virginia

2. Dudley Knox Library
   Naval Postgraduate School
   Monterey, California